X-ray Study of Neutral Iron Line Emission in the Galactic Ridge: Contribution of Low-Energy Cosmic Rays

Kumiko Nobukawa (Kawabata)

Department of Physics, Graduate School of Science, Kyoto University
Kitashirakawa Oiwake-cho, Sakyo-ku, Kyoto, 606-8502, Japan
kumiko@cr.scphys.kyoto-u.ac.jp

February 10, 2016

Abstract

The Galactic diffuse X-ray emission (GDXE) is unresolved X-rays prevailing along the Galactic plane (e.g. Worrall *et al.* 1982, *Astrophysical Journal* **255**, 111–121). One of the most remarkable features of the GDXE is strong K-shell lines of neutral, helium-like and hydrogen-like iron at 6.4 keV, 6.7 keV and 7.0 keV, respectively. A popular idea for the origin of the GDXE is a superposition of many faint point sources, such as cataclysmic variables (CVs) and coronally active binaries (ABs) because more than 80% of the GDXE has been resolved into point-like sources at a small area near the Galactic center (Revnivtsev *et al.* 2009, *Nature*, **458**, 7242, 1142–1144). However, the spectra of the GDXE are different from position to position (Uchiyama *et al.* 2013, *Publications of the Astronomical Society of Japan*, **65**, 19). If many point sources contribute to the GDXE, the spectra should be spatially uniform. Previous debate on the GDXE origin has been based on the results of limited spectral and spatial resolution. In this dissertation, using the Suzaku satellite, we have measured the detailed spatial distributions (the scale heights) and spectral features (the equivalent widths) of the 6.4 keV, 6.7 keV, and 7.0 keV lines separately. The scale height of the 6.7 keV line is roughly consistent with those of CVs and ABs, while that of the 6.4 keV line is far smaller than those of the CVs and ABs, and similar to molecular clouds. Furthermore clear enhancements of the 6.4 keV line relative to the 6.7 keV line are found at $1.^\circ5 < l < 3.^\circ5$ (GC east) and $l = 20^\circ$ regions. These enhancements are associated with molecular gas. The X-ray spectra of the enhanced regions show large equivalent widths of > 300 eV (Nobukawa *et al.* 2015, *The Astrophysical Journal Letters*, **807**, L10). Even in the GDXE of non-excess areas, an assembly of CVs and ABs does not reproduce the spectra; at least a half of the 6.4 keV line emission along the Galactic plane cannot be explained by point sources. Thus additional contribution of other sources with a strong 6.4 keV line is required. Since the 6.4 keV line from molecular gas irradiated by X-rays, cosmic-ray protons or electrons has a large equivalent width (> 300 eV), the 6.4 keV line should be dominated by the diffuse emission from molecular gas. The scattered photons from the interstellar gas originated from bright X-ray sources are less than 10% of the total 6.4 keV line emission. Therefore the most possible origin is low-energy cosmic rays (LECRs). The energy densities of the LECRs would be ~ 10 eV cm^{-3} and ~ 0.01 eV cm^{-3} for protons and electrons, respectively. Our study demonstrates that the 6.4 keV line can be a unique probe to investigate the LECRs.

Acknowledgement

I would like to express my special appreciation and thanks to my advisor, Professor Emeritus Dr. Katsuji Koyama for providing comprehensive guidelines and for encouraging my research throughout my Ph.D. years. His advice has consistently been based on far-sighted vision. I consider it as a great opportunity to do my Ph.D research under his guidance and to learn from his research expertise.

I would like to thank my supervisor, Professor Dr. Takeshi Tsuru, who has guided me through my Ph.D. years and provided me with the valuable opportunity to develop the SXI onboard ASTRO-H. The experience of developing the SXI occupies an important place in my career. I have learned to combine observational astrophysics research and detector development.

I am vey grateful to the members of my Ph.D. committee for their time and valuable feedback on a preliminary version of this dissertation. I would particularly like to acknowledge Professor Dr. Toru Tanimori and Dr. Hidetoshi Kubo, who have also provided valuable comments in the laboratory colloquiums.

I gratefully acknowledge my research collaborators. Professor Dr. Shigeo Yamauchi at Nara Women's University analyzed the Suzaku data with me and provided a lot of information on previous studies. Dr. Kazufumi Torii and Professor Dr. Yasuo Fukui at Nagoya University provided the NANTEN data and discussed with me which molecular clouds corresponds to the enhancements of the 6.4 keV line and what is the origin of low-energy cosmic rays. I am also very grateful to Dr. Takaaki Tanaka. His comments and calculation based on his expertise in cosmic-ray acceleration in SNRs have been valuable and they strengthen the discussion in my Ph.D. research. He has also corrected English errors in this dissertation.

I am very thankful to members of the Cosmic-Ray laboratory for all the great times that we have shared.

I am deeply thankful to my parents for their love, support and encouragements. I am very much indebted to my husband Dr. Masayoshi Nobukawa, who has supported me in my personal and academic life. Without him, I would never have been complete my Ph.D. nor this dissertation.

This work is supported by Research Fellowships of the Japan Society for the Promotion of Science for Young Scientists.

Kumiko K. Nobukawa

Kyoto
February 2016

Contents

List of Figures

List of Tables

Chapter 1

Review

1.1 Interstellar medium and spiral arms in the Milky Way galaxy

The Milky Way, where we live, is the closest among all galaxies in the universe, and hence a basic target to study and understand an incredible number of galaxies which exist in the universe. Many researchers have observed the Galaxy in the optical band since the days of Galileo Galilei. However, optical surveys cannot see far into the Galactic plane because of large extinction due to interstellar dust and gas. Thanks to development in technology, we can today observe the Galaxy by various wavelengths other than the optical band: radio, far and near infrared, X-ray, and gamma-ray.

The Milky Way is classed into a bar spiral galaxy. In the nucleus of the Milky Way, a supermassive black hole with a mass of $\sim 4 \times 10^6 M_\odot$[1], Sagittarius A* (Sgr A*), has been found (Genzel *et al.*, 2000; Ghez *et al.*, 2000, 2008). Sgr A* sits at a dynamical center of the Galactic gravity (e.g. Ghez *et al.*, 2008). The main part of the Galaxy is the disk, where stars and gas are concentrated in. The Sun, which is located at a distance between 7.5 kpc and 8.5 kpc from the Galactic center, is also placed in the disk.

1.1.1 Spiral arm structures

Figure 1.1 shows an artists concept of a face-on view of the Milky Way. Spiral structures in a galaxy, which are called spiral arms, are regions where star formation actively occurs. The Milky Way galaxy is found to have four principal spiral arms from star, interstellar-gas, and dust distributions: the Scutum-Centaurus arm, the Sagittarius arm, the Norma arm, and the Perseus arm. In addition, the (Near and Far) 3 kpc arm, which could be a ring-like structure, also has been reported (e.g. Van Woerden and Rougoor, 1957; Dame and Thaddeus, 2008).

1.1.2 Interstellar medium (ISM)

The space between stars in the disk is filled with the interstellar medium (ISM), which is mainly composed of hydrogen (neutral atoms, molecules, or ions).

[1] The symbol of $M_\odot$ represents the solar mass of 1.99×10^{33} g.

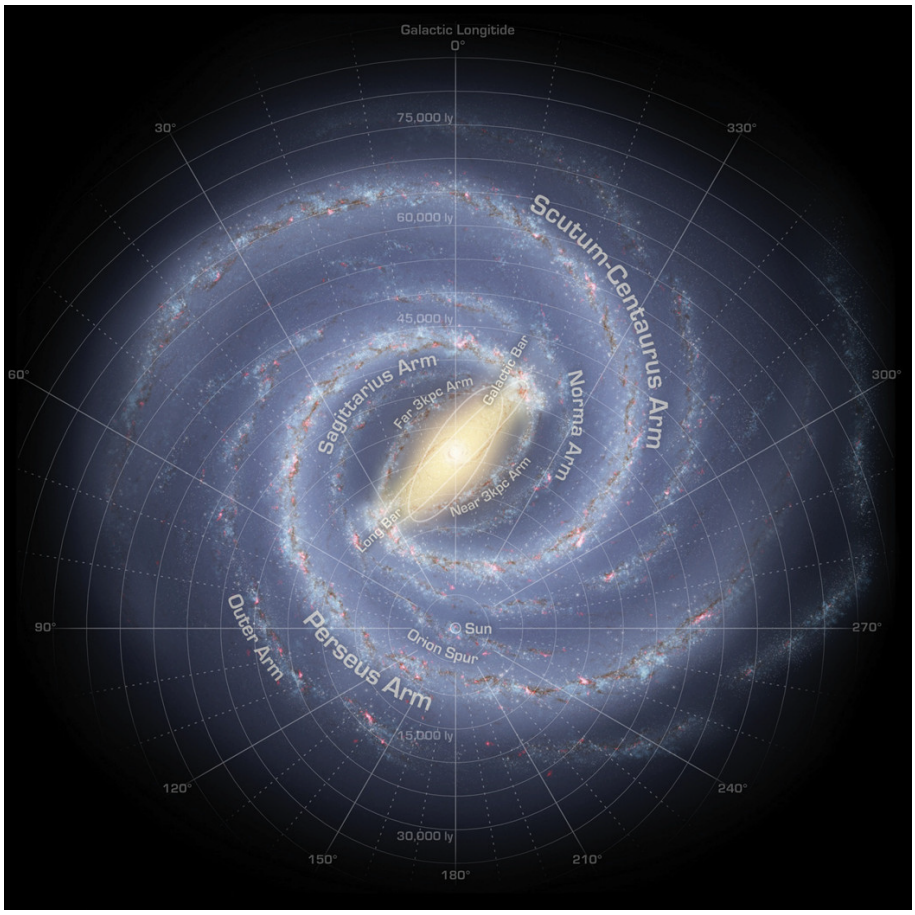

Figure 1.1. Sketch of face-on view of the Milky Way taken from Churchwell *et al.* (2009).

Neutral hydrogen atoms (HI gas)

Cold (∼100 K) neutral hydrogen atoms can be observed by a radio emission line at 21 cm. Since electrons and protons have intrinsic magnetic moments, interaction between those magnetic dipole causes the hyperfine structure. The energy state of the electron spinning parallel has slightly higher than that of the electron spinning antiparallel. When an electron transition occurs from the higher to the lower energy orbit, radiation at a wavelength of 21 cm is emitted from the atom. This is an extremely rare phenomenon; its lifetime is 1.1×10^7 years. However, there are an enormous amount of hydrogen atoms in the interstellar space, and thus a considerable number of transition occur. The HI gas is distributed through the Milky Way galaxy, and traces the spiral-arm structure of the Milky Way. If we assume that most of gas follows an circular orbit around the Galactic center and know the rotation curve for the Galaxy (e.g. Fich *et al.*, 1989), we obtain the relation between the radial velocity along the line of sight and distance from the Sun. Combining this relation with the HI line spectra, which reflect motion of the gas (Doppler effect), we can yield spatial distribution of HI gas in the Milky Way (e.g. Oort *et al.*, 1958; Nakanishi and Sofue, 2003). The vertical thickness of the HI gas increases with the Galactocentric distance; the scale height at the Galactocentric distance of ~ 1 kpc is ~ 100 pc while that of ~ 10 kpc is ~ 300 pc (Nakanishi and Sofue, 2003).

Molecular clouds

When the density of hydrogen becomes higher, hydrogen exists as molecular gas (H_2). A hydrogen molecule is a homonuclear linear molecule with no permanent dipole moment, and hence cannot radiate emission in low temperature of ∼10 K. The line emission from carbon-monoxide (CO) is widely used as a main tracer of molecular gas. The transitions of CO is more frequent than that of H_2 and the emission lines are detected even in quite tenuous molecular gas. Furthermore, a proportional relationship between the intensity of the CO line and amount of H_2 is observationally confirmed. A factor to convert the ^{12}CO intensity (K km s^{-1}) to the H_2 column density $N_{\rm H}$ (cm^{-2}) is called X-factor. The X-factor in the solar neighborhood of $\sim 1.8 \times 10^{20}$ is reported (e.g. Dame *et al.*, 2001). Torii *et al.* (2010) obtained the X-factor of $\sim 0.7 \times 10^{20}$ in the Galactic center (GC). Figure 1.2 shows a CO velocity-integrated map and longitude-velocity map in the Milky Way (Dame *et al.*, 2001). The GC region represents the strongest concentration of molecular gas and a large velocity dispersion in the CO maps. This corresponds to the central molecular zone (CMZ) of about 200 pc radius, in which the molecular gas is characterized by large densities, high temperatures, and apparently strong magnetic fields (e.g. Morris and Serabyn, 1996).

Ionized hydrogen (HII gas)

The ionization energy of an electron in hydrogen atoms is 13.6 eV. Hydrogen atoms are ionized by photoionization by ultraviolet, collisional ionization by high energy particles, and thermal ionization. Ionized hydrogen (HII) regions in the ISM are ionized by ultraviolet from young massive (O- or B-type) stars which were formed inside the giant molecular clouds. HII regions trace star formation at the present time, and have the temperature of 10^4 K typically. Also young white dwarfs radiate ultraviolet. Old low-mass (1–8$M_\odot$) stars evolve to red giants and finally to white dwarfs. Young white dwarfs are hot enough to ionize the stellar envelope material that had been ejected during the red giant phase. This phenomenon is called as planetary nebulae.

There exists much higher temperature ($\gtrsim 10^6$ K) gas emitting X-rays in the Milky Way. We will describe the hot gas (plasma) in the next section.

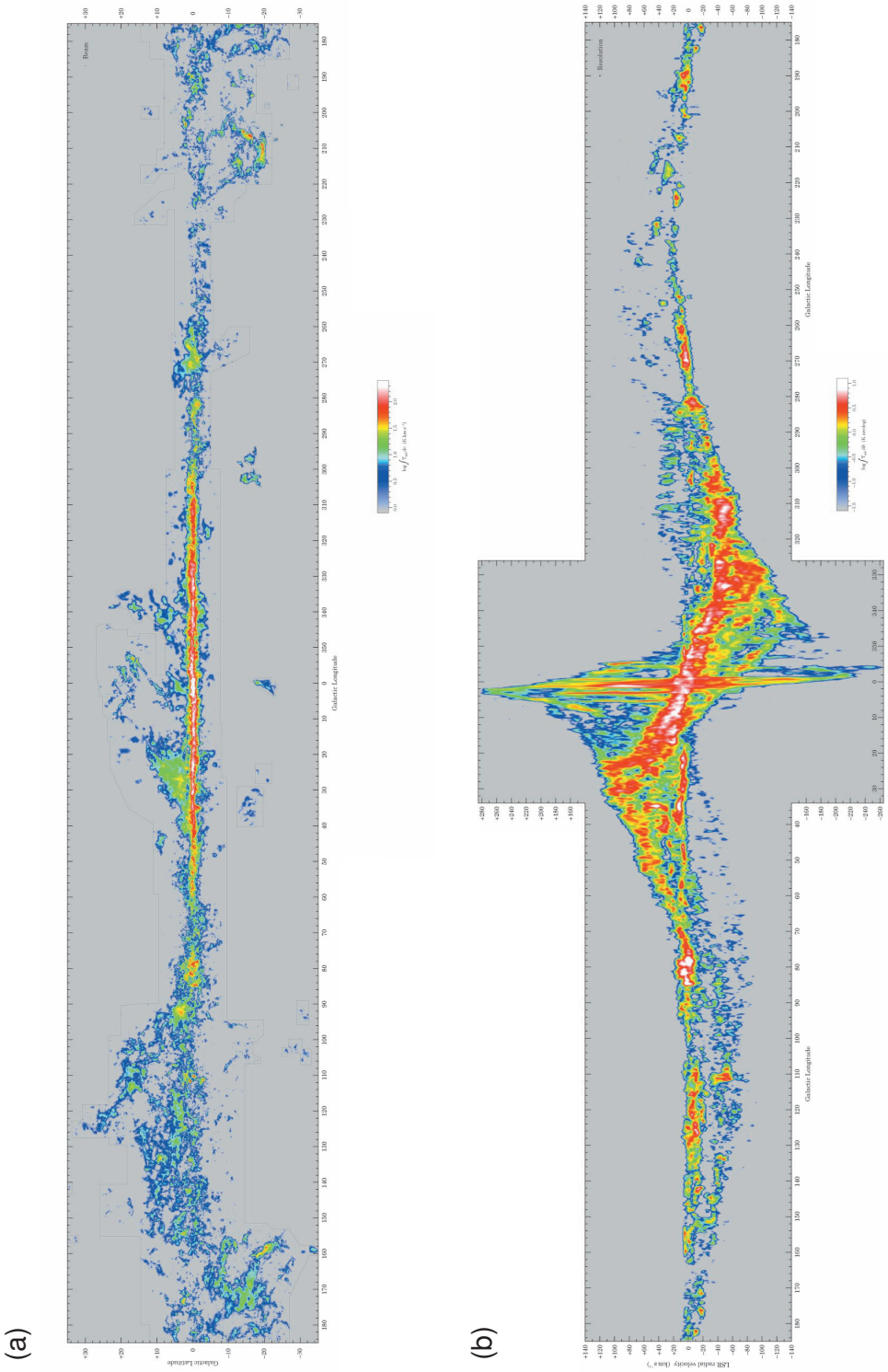

Figure 1.2. (a) Velocity-integrated CO map and (b) longitude-velocity map of Milky Way. Both figures are taken from Dame *et al.* (2001).

1.2 X-ray view of the Milky Way galaxy: the Galactic diffuse X-ray emission (GDXE) with iron K-shell lines

X-ray observations by the HEAO 1 satellite discovered unresolved X-ray emission in the 2–10 keV band with the half thickness of ~ 240 pc in the inner disk ($50° < l < 120°$ and $-130° < l < -70°$)[2] of the Milky Way (Worrall *et al.*, 1982). This emission has been called the Galactic ridge X-ray emission (GRXE). Worrall *et al.* (1982) estimated the luminosity of the GRXE within a 7.8 kpc radius of the Galactic disk and obtained $\sim 1.4 \times 10^{38}$ erg s^{-1} in the 2–10 keV band. They argued that the origin of the X-ray emission is unresolved point sources. The EXOSAT found that the GRXE extends from the GC to $|l| = 40°$ with the scale height of $\sim 2°$ (Warwick *et al.*, 1985).

The Japanese X-ray astronomy satellite Tenma detected an intense iron line in the spectra taken from the Galactic ridge (Koyama *et al.*, 1986b). An example of the spectra is shown in figure 1.3. The line energy of 6.7 keV is consistent with the fluorescence line from helium-like iron, and therefore the line indicates that the GRXE is composed of an optical thin thermal plasma.

Performing a survey observation along the Galactc plane, the Ginga satellite discovered that the iron line intensity has a large peak in the GC region (Koyama *et al.*, 1989; Yamauchi *et al.*, 1990; Yamauchi and Koyama, 1993). The intense line-emitting region is distributed within the angular size of $1.^{\circ}8 \times 1.^{\circ}0$ around Sgr A* (Yamauchi *et al.*, 1990). The intense X-ray emission from the GC has been referred to as the Galactic center X-ray emission (GCXE).

The ASCA satellite separated the previously observed iron line at 6.7 keV in the GCXE into three iron K-shell lines: the 6.4 keV line from neutral iron, the 6.7 keV line from helium-like iron, and the 7.0 keV line from hydrogen-like iron. The emission mechanism of the 6.4 keV line differs from that of the 6.7 keV and 7.0 keV lines. The 6.7 keV and 7.0 keV lines are due to collisional excitation in optically-thin thermal plasma. On the other hand, the 6.4 keV line originates from photoionization by external X-rays or inner-shell ionizaion by high-energy particles. The external X-rays and particles should have higher energy than the neutral-iron K edge at 7.1 keV. Figure 1.5a shows a spectrum extracted from the GC obtained by ASCA. In the GRXE, the iron K-shell line was resolved into the three iron lines for the first time by Suzaku (Ebisawa *et al.*, 2008).

ASCA revealed that the GRXE cannot be explained by one-temperature plasma model. The GRXE spectrum exhibits K-shell lines from helium-like magnesium, silicon, sulfur, and iron as is shown in figure 1.5b, and is fairly fitted by two-temperature plasma with the temperatures of ~ 0.8 keV and ~ 7 keV (Kaneda *et al.*, 1997); the former temperature plasma is required to explain the magnesium, silicon, and sulfur lines while the latter temperature plasma is for the iron lines. Similar two-temperature models are required also in the GCXE (Muno *et al.*, 2004; Uchiyama *et al.*, 2013). Figure 1.6a and b show X-ray spectra of the GCXE and GRXE fitted with a two-temperature model as well as the 6.4 keV line and continuum radiated from cold material. We will hereafter call the plasma with the lower temperature as the low-temperature plasma (LP) and the one with the higher temperature as the high-temperature plasma (HP).

The distribution of the GRXE and GCXE has often been expressed by an exponential model. Yamauchi and Koyama (1993) measured the latitudinal distribution of the GRXE ($|l| > 10°$) and found that the e-folding scale height of the 6.7 keV line emission is ~100 pc. Kaneda *et al.* (1997) obtained

[2]Studies of the Milky Way commonly use the Galactic coordinate system: the Galactic longitude (l) and the Galactic latitude (b). See also figure 1.1, which shows the Galactic longitude.

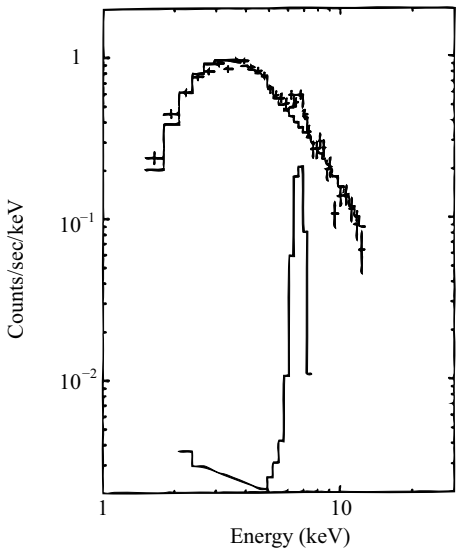

Figure 1.3. Spectrum taken from the Galactic plane observed by Tenma (Koyama *et al.*, 1986b).

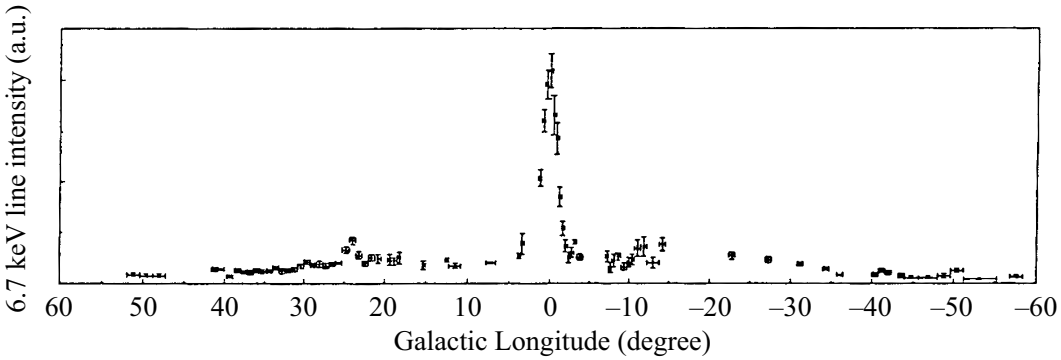

Figure 1.4. Intensity distribution of the 6.7 keV line along the Galactic plane taken from a Ginga survey (Koyama *et al.*, 1989).

a similar result by observing the Scutum arm ($l \sim 28°$). Revnivtsev *et al.* (2006a) measured the scale height of the GRXE of 130 ± 20 pc in the 3–20 keV band at $l = 20°$. Also Revnivtsev and Molkov (2012) performed a scan survey across the Galactic plane with the stripe from $b \sim 0°$ to $b \sim 30°$ at $l \sim 18.^{\circ}5$ and obtained the scale height of ~ 107 pc in the 4.3–10.5 keV. Uchiyama *et al.* (2013) measured intensity profiles of the 6.4 keV, 6.7 keV, and 7.0 keV lines and the continuum band in 5–8 keV, and thus separated the GCXE from the GRXE with scale lengths of $0.^{\circ}6$ (80 pc) and 50° (8 kpc) and with scale heights of $\sim 0.^{\circ}2$–$0.^{\circ}4$ (30–60 pc) and $\sim 1°$–$5°$ (150–750 pc), respectively[3].

Yamauchi and Koyama (1993) discovered a clear excess near the GC, which is broader than the GRXE component. Its scale height is as large as $\sim 5°$. A similar result was obtained by Valinia and Marshall (1998), who observed the $|l| < 30°$ region and found the presence of two components: a thin and thick disk components with the scale heights of $\lesssim 70$ pc ($0.^{\circ}5$) and ~ 500 pc (4°), respectively. The thick disk component was found also by Revnivtsev (2003). They observed the GRXE near the GC in the energy band of 3–20 keV and found that the intensity distribution at $|b| > 2°$ could be

[3]On the assumption of the distance of 8 kpc.

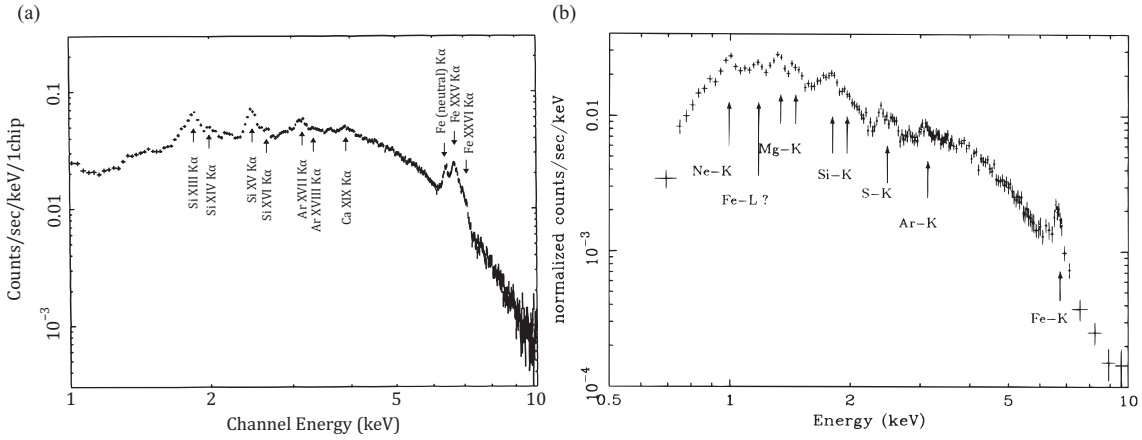

Figure 1.5. Spectrum of (a) the GCXE (Koyama *et al.*, 1996) and (b) the GRXE (Kaneda *et al.*, 1997) observed by ASCA.

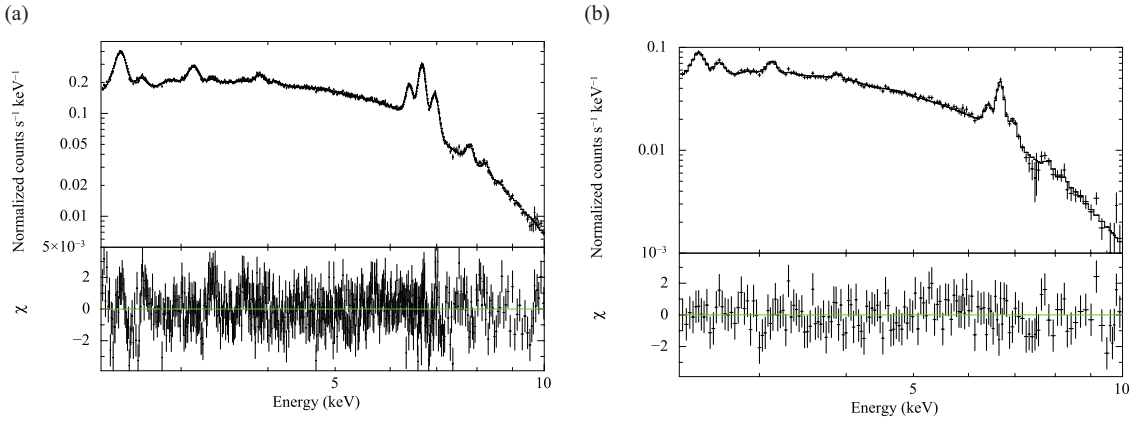

Figure 1.6. X-ray spectra of (a) the GCXE and (b) the GRXE observed by Suzaku (Uchiyama *et al.*, 2013). Both the spectra are fitted with a two-temperature model.

well described by an exponential model with scale height of $\sim 3°$. This bulge-like emission is called as the Galactic bulge X-ray emission (GBXE). Hereafter, we will call the GCXE, GBXE, and GRXE collectively as the Galactic diffuse X-ray emission (GDXE).

1.3 Debates over the origin of the iron K-shell lines in the GDXE

The origin of the GDXE, particularly that of the iron lines, has been caused a lot of discussion. The most popular idea is a superposition of many point sources as is the case in the cosmic X-ray background (CXB), which is explained by a sum of active galactic nuclei below several hundreds keV (e.g. Ueda *et al.*, 2003). Yamauchi *et al.* (1996) performed Poisson-fluctuation analysis of the surface brightness of the GRXE and found that point sources which have the luminosity larger than $\sim 2 \times 10^{33}$ erg s^{-1} in the 2–10 keV band are excluded as the origin of the GRXE.

Cataclysmic variables (CVs) and coronally active binaries (ABs) have the luminosity of $\lesssim 10^{33}$ erg s^{-1}

in the 2–10 keV band, and their spectra exhibit iron K-shell lines as seen in the GDXE. The number densities of CVs and ABs are considered to be large in the Milky Way. Therefore, CVs and ABs have been major candidates for the GDXE. CVs are close binaries that consist of a white dwarf and a companion star, and show violent variability in the time-scales of seconds to years. The two objects are so close to each other that the gravity of white dwarf tears off gas from a companion star and the gas falls into the white dwarf. X-rays are radiated during the accretion.

ABs are late-type close binaries like RS Canum Venaticorum (RS CVn) systems and BY Draconis (BY Dra-), Algol-, and W Ursae Majoris (W UMa-) type binaries. Most of ABs fall into the first two types. RS CVn systems typically consist of a G- or K-type giant or subgiant with a late-type main-sequence or subgiant companion, while BY Dra-type binaries typically consist of two late-type main-sequence stars (Dempsey *et al.*, 1993, 1997). Algol binaries contain late-type component, typically spectral type K, filling its Rosh robe and losing mass to a A- or B-type companion (Dempsey *et al.*, 1993). W UMa-type binaries are composed of F-K stars which are in contact via a common convective envelope (McGale *et al.*, 1996).

Sazonov *et al.* (2006) constructed an X-ray luminosity function of nearby X-ray sources in the luminosity range of 10^{30}–10^{34} erg s^{-1} (2–10 keV) by using RXTE. They also extended this luminosity function down to $10^{27.5}$ erg s^{-1} by using the Rosat All-Sky Survey in soft X-rays; they converted the observed soft X-ray (0.5–2 keV) luminosity to the 2–10 keV energy band based on the 0.1–10 keV spectra of typical sources. Although they ascribed 50% errors in converting, they found that the local cumulative X-ray (2–10 keV) emissivities (per unit stellar mass) of ABs and CVs are $(2.0 \pm 0.8) \times 10^{27}$ and $(1.1 \pm 0.3) \times 10^{27}$ erg s^{-1} $M_{\odot}^{-1}$, respectively.

Revnivtsev *et al.* (2006a) studied the surface brightness of the GBXE ($|l| < 10^{\circ}$ and $1^{\circ} < b < 8^{\circ}$) and GRXE ($|b| < 0.^{\circ}5$) and found that the distribution of the 3–20 keV band closely follows a Galactic near-infrared (NIR) surface brightness measured by COBE/DIRBE (3.5 μm). The NIR data trace the Galactic stellar mass distribution. The authors also calculated a ratio of X-ray luminosity to stellar mass in the GBXE and obtained the ratio of $(3.5 \pm 0.5) \times 10^{27}$ erg s^{-1} $M_{\odot}^{-1}$. This value is almost consistent with the sum of the emissivities of ABs and CVs of $\sim 3.1 \times 10^{27}$ erg s^{-1} $M_{\odot}^{-1}$ (Sazonov *et al.*, 2006). Therefore, they claimed that the bulk of the GDXE is composed of point sources. Also Revnivtsev *et al.* (2006b) measured the distribution of the 6.7 keV line along the Galactic plane. Here, they did not resolved the iron line at 6.7 keV into the 6.4 keV, 6.7 keV, and 7.0 keV lines due to performance limitations of the detector. They found that the line distribution spatially corresponds to the NIR surface brightness (4.9 μm) as is shown in figure 1.7. They also demonstrated the proportionality between the 6.7-keV surface brightness and the NIR in the $|l| > 10^{\circ}$ and $|l| < 3^{\circ}$ regions.

XMM-Newton and Chandra have the good spatial resolution of 5″ and 0.6″ (FWHM; Aschenbach *et al.*, 2000; Weisskopf *et al.*, 2002), respectively, and therefore they have an advantage to resolve point sources. Observing by XMM-Newton, Muno *et al.* (2004) resolved only 10% of the GCXE into discrete point sources under their detection limit for point sources of $\sim 3 \times 10^{-15}$ erg s^{-1} cm^{-2} ($\sim 10^{31}$ erg s^{-1} in luminosity) in the 2–10 keV band. A similar result was obtained in Chandra observations of the GRXE performed by Ebisawa *et al.* (2001, 2005) under the same detection limit as Muno *et al.* (2004).

Revnivtsev *et al.* (2009), on the other hand, claimed that they resolved ∼80% of the GDXE in the 6–7 keV band into discrete point sources by performing deep observation (1 Msec) at $(l, b) = (0.^{\circ}1, -1.^{\circ}4)$ by Chandra (Chandra bulge field: CBF). Figure 1.8 shows the spectrum of total emission observed by Chandra as well as the summed spectra of the detected sources and unresolved emission.

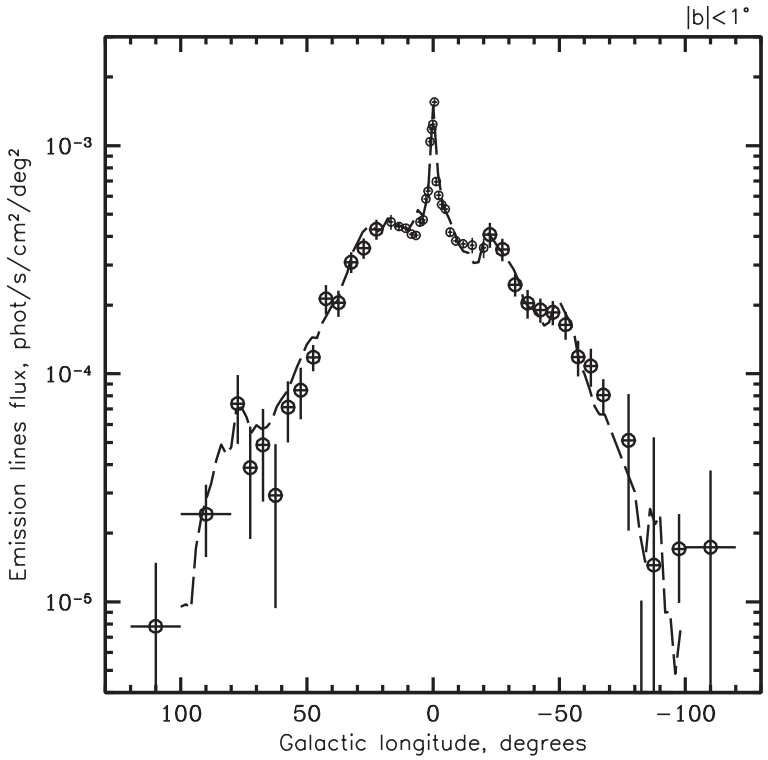

Figure 1.7. Profiles of the surface brightness of the 6.7 keV line along the Galactic plane at $|l| < 2°$ measured by RXTE/PCA (Revnivtsev *et al.*, 2006b). The dashed line shows the profile of the surface brightness of 4.9 μm measured by COBE/DIRBE.

The detected sources exhibit a prominent 6.7 keV line although the authors did not separate the iron line into the three lines due to finite energy resolution of the instrument. They also made the histogram which shows the fraction of resolved X-ray emission around the 6.7 keV line as a function of the limiting source flux/luminosity (figure 1.9). Most of the detected point sources are probably ABs (with luminosity of $< 10^{32}$ erg s^{-1}) and CVs (with luminosity of 10^{31}–10^{32} erg s^{-1}). They predicted the attributable fraction of the ABs and CVs of 2 : 1. This seems to be a crucial result. However, there are several problems with the point-source scenario as discussed later (section 2.1).

The other scenario for the origin of the GDXE is a truly diffuse emission. Since the GDXE involves the emission lines from highly ionized iron (the 6.7 keV and 7.0 keV lines), diffuse thermal plasma can contribute to the GDXE. However, there are some problems in the diffuse-plasma scenario. The first one is an energy source. Koyama *et al.* (1986a) estimated the contribution of uncatalogued supernova remnants (SNRs) and found that the supernova (SN) rate of one SN per 10 years can explain the observational result. This rate is much higher than the canonical value of one SN per 50–100 years. The second problem is that hot plasma with temperature as high as 5–10 keV cannot be bound to the small scale height of ~ 100 pc by the gravitational potential of the Milky Way.

The discovery of non-thermal emission (Yamasaki *et al.*, 1997; Valinia and Marshall, 1998) raised another scenario in which the interaction of low-energy cosmic-ray (LECR) electrons with the ISM contributes to the GDXE. Valinia *et al.* (2000) argued that the hard X-ray emission above 2 keV comes from two components: a thermal component with the temperature of 2–3 keV and a non-thermal component produced by LECR electron. In this scenario, the 6.7 keV line is due to the former while

the 6.4 keV line originates from the latter. Masai *et al.* (2002) claimed that the GRXE can be explained by non-equilibrium emission due to quasi-thermal electrons with the temperature of a few tens of keV. These electrons are accelerated in *situ*, and can be bound gravitationally in the Galactic disk. Tanuma *et al.* (1999) proposed that magnetic reconnection plays a role in producing the hot plasma in the GDXE. Magnetic reconnection, which can occur by SNs, cosmic rays, Parker instability, or turbulence, heats the interstellar gas by releasing interstellar magnetic energy. Sunyaev *et al.* (1993) predicted that a part of the GCXE may be due to Thomson scattering of X-rays from nearby sources by dense gas. Molaro *et al.* (2014) applied this idea to the GRXE and suggested that 10–30% of the GRXE arise from the scattering of X-rays from bright X-ray binaries by the ISM.

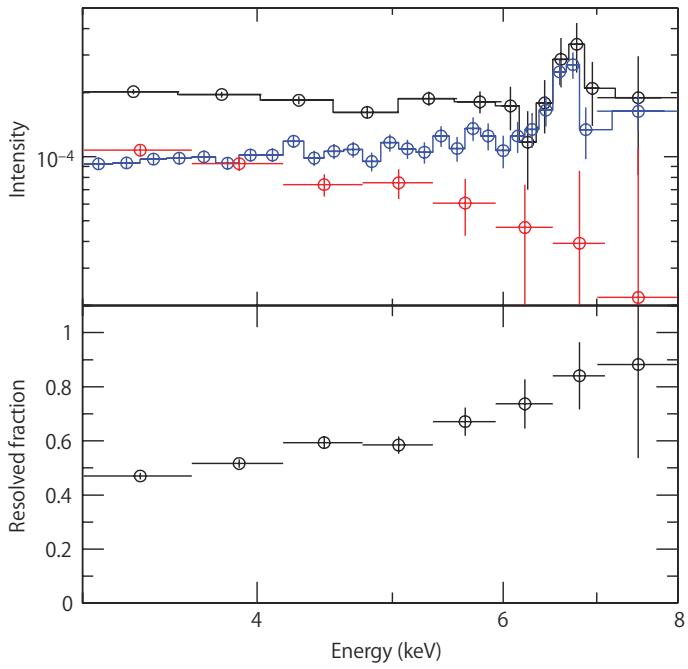

Figure 1.8. (upper) Spectra obtained by the Chandra deep observation of the region near the Galactic center (the CBF: $l = 0.°1$, $b = -1.°4$). Black, blue and red data points show the spectrum of the total emission, the collective spectrum of all detected sources, and the spectrum of the remaining unresolved emission, respectively. (bottom) Fraction of the X-ray emission resolved by Chandra into point sources as a function of X-ray photon energy. Both the figures are taken from Revnivtsev *et al.* (2009).

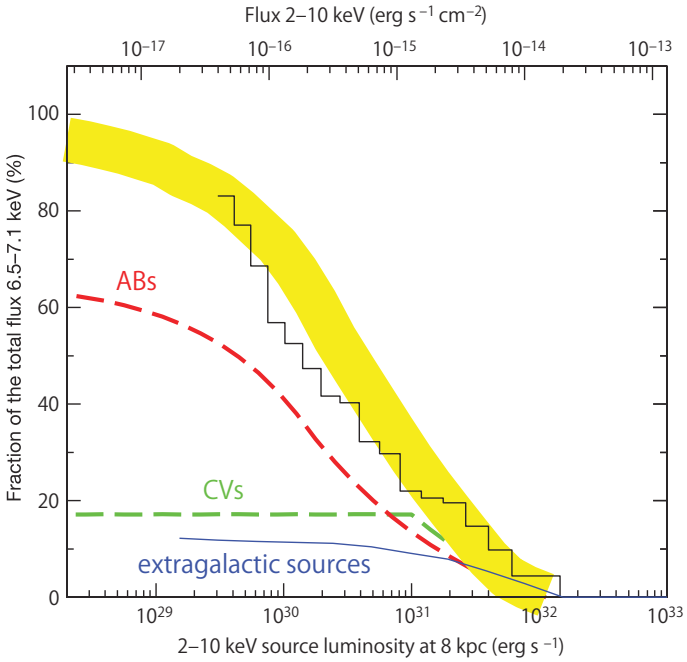

Figure 1.9. Fraction of resolved X-ray emission around the 6.7 keV iron emission line as a function of the limiting source flux/luminosity (Revnivtsev *et al.*, 2009). The histogram shows the fraction of the total flux in the 6.5–7.1 keV energy band in the CBF provided by discrete sources with fluxes above a given detection threshold in the 2–10 keV energy band. The wide yellow curve shows the corresponding dependence expected for a combination of Galactic sources with luminosities below 10^{32} erg s^{-1} (all located at the Galactic center distance of 8 kpc) and extragalactic sources with fluxes below 2×10^{-14} erg s^{-1} cm^{-2} in this energy band. The blue, green, and red curves show the expected contributions of extragalactic sources, CVs, and ABs, respectively.

1.4 6.4 keV clumps in the Galactic center region

Figure 1.10 shows the longitude distribution of the 6.4 keV and 6.7 keV lines in the GC obtained by Suzaku. Both the profiles are clearly different from each other; the profile of the 6.7 keV line distributes smoothly while that of the 6.4 keV line are clumpy. Therefore, the 6.4 keV clumps differs from the 6.7 keV line in the origin. Koyama *et al.* (1996) discovered that these clumpy structures correspond to giant molecular clouds in the Sgr B2 and the Radio Arc regions. Figure 1.11 shows the X-ray image in the 6.4 keV band and velosity-integrated CS ($J = 1 - 0$) map in the GC. CS emission traces highly dense gas, and we see the regions which is bright in 6.4 keV corresponding to those with dense molecular clouds. The 6.4 keV clumps should be originate from large amount of neutral iron atoms in the clouds.

Koyama *et al.* (1996) proposed that the 6.4 keV emission from the Sgr B2 cloud is due to photoionization of neutral iron by external X-rays. This idea is called an X-ray reflection nebulae (XRN) scenario, which is essentially the same as the prediction by Sunyaev *et al.* (1993). Murakami *et al.* (2000) found the large equivalent width (1–2 keV) of the 6.4 keV line and the deep absorption edge at the iron K-edge (7.1 keV) corresponding to $N_{\rm H} \sim 10^{24}$ cm^{-2}. They also discovered that the peak position of the 6.4 keV line emission is shifted from the core of the molecular cloud toward the Galactic

center by about 1′–2′. These features are well explained by the XRN model. Murakami *et al.* (2001a) discovered another 6.4 keV clump in the Sgr C region. In order to explain the 6.4 keV line intensity, a bright source with the luminosity of $\geq 10^{38}$–10^{39} is required (Koyama *et al.*, 1996; Murakami *et al.*, 2001a,b). A candidate source is Sgr A*, the super-massive black hole at a distance of several hundred light-years from the molecular clouds (Ghez *et al.*, 2008). Although the present luminosity of Sgr A* is only 10^{33}–10^{34} erg s^{-1} (Baganoff *et al.*, 2003), it is possible that Sgr A* was bright several hundred years ago with an X-ray luminosity a million times higher than the present.

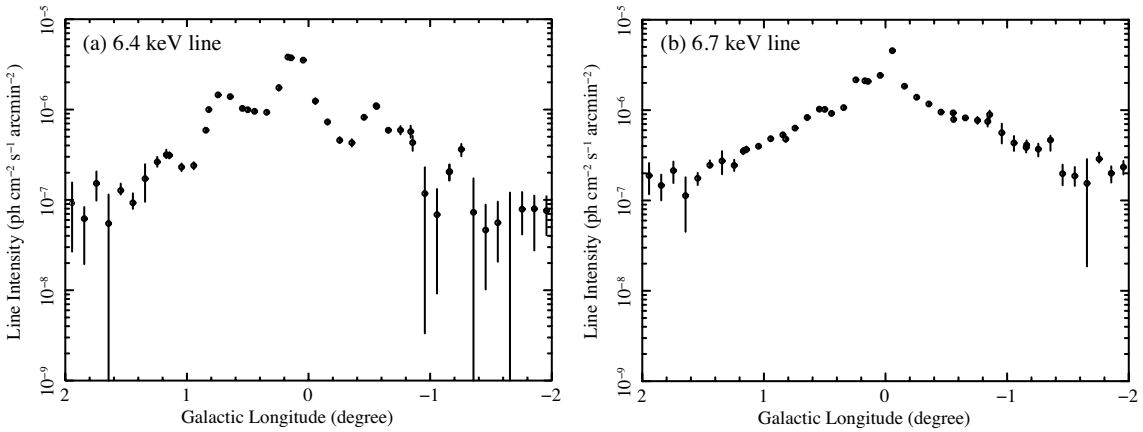

Figure 1.10. Longitude distributions of (a) the 6.4 keV line and (b) the 6.7 keV line in the Galactic center region. The data points are taken from Uchiyama *et al.* (2011).

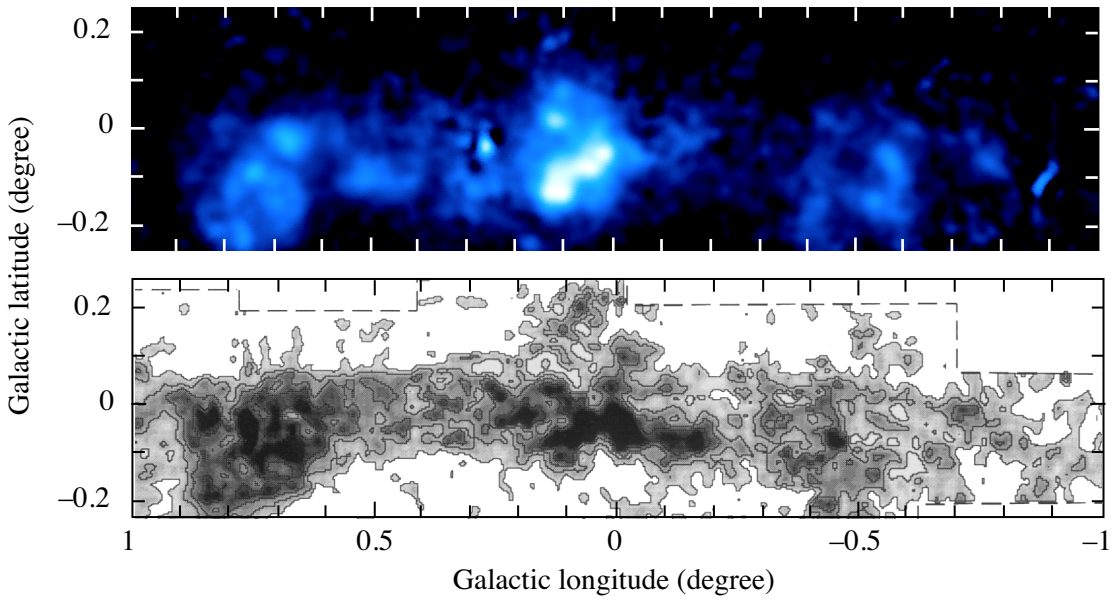

Figure 1.11. (top) X-ray image in the 6.4 keV line in the Galactic center region obtained by Suzaku (Nobukawa, 2011). (bottom) Velosity-integrated CS (J = 1–0) emission in the same region as the top panel. The velocity integrated range is from −200 km s^{-1} to 200 km s^{-1} (Tsuboi *et al.*, 1999).

Inui *et al.* (2009) discovered time variability of the 6.4 keV flux in the Sgr B2 region from the archival data for 10 years obtained with Suzaku, XMM-Newton, Chandra, and ASCA; the 6.4 keV

line intensity decreased to 60% in the time span 1994–2005 (figure 1.12) in contrast to the constant flux of the 6.7 keV line. Also other authors detected similar time variability of the 6.4 keV line flux in other regions (Ponti *et al.*, 2010; Nobukawa *et al.*, 2011). Although these results favored the XRN scenario, another scenario in which the 6.4 keV line is produced by inner-shell ionization by LECR electrons could not be rejected.

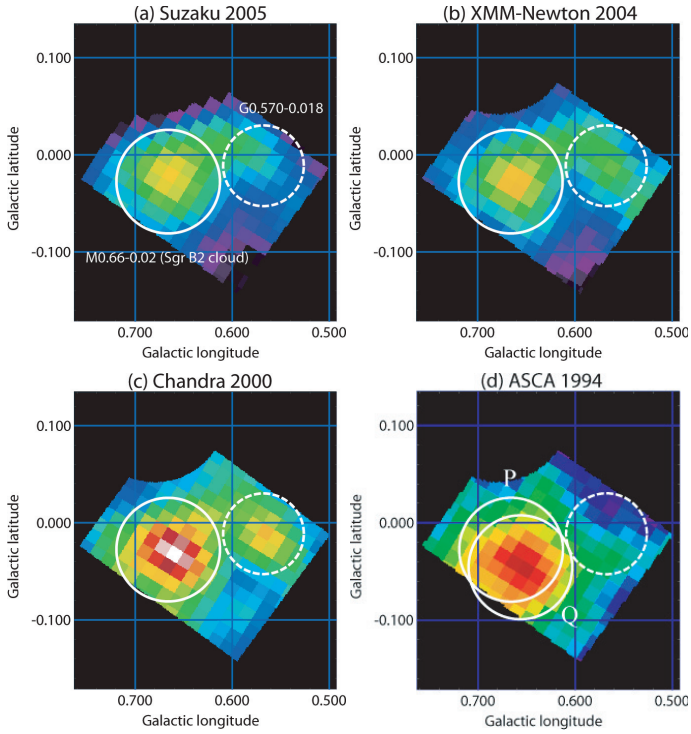

Figure 1.12. Surface brightness maps of the iron lines obtained with (a) Suzaku/XIS in 2005, (b) XMM-Newton/MOS and PN in 2004, (c) Chandra/ACIS-wein 2000, and (d) ASCA/SIS in 1994. Pixel size is 50″×50″ in each case (Inui *et al.*, 2009).

The equivalent widths consolidated the XRN scenario. Nobukawa *et al.* (2010) discovered K-shell lines of neutral argon, calcium, chrome, and manganese atoms in the GC region. The equivalent widths of these K-shell lines indicate that the metal abundances should be 1.6 solar in the XRN scenario and 4 solar in the electron-bombardment scenario. However, the metal abundance in the GC was found to be 1–2 solar (Muno *et al.*, 2004; Nobukawa *et al.*, 2011; Uchiyama *et al.*, 2013). Therefore, the origin of the 6.4 keV clumps are believed to the XRN.

In addition to the 6.4 keV clumps, a more uniformly distributed 6.4 keV line emission extending from the GC to the Galactic plane is found (see figure 1.10; Ebisawa *et al.*, 2001; Yamauchi *et al.*, 2009; Uchiyama *et al.*, 2011). This component should have an origin other than the XRNe reflecting X-rays from Sgr A*. Its origin is under debate as a part of the GDXE. It is uncertain even whether the 6.4 keV line emission shares the origin with the other iron lines and the continuum. At present, a common candidate for the origin of the 6.4 keV line emission is CVs because they exhibit a prominent 6.4 keV line (Yuasa *et al.*, 2012). However, the previous studies supporting point-source scenario have several problems to be considered and addressed as discussed in the next chapter.

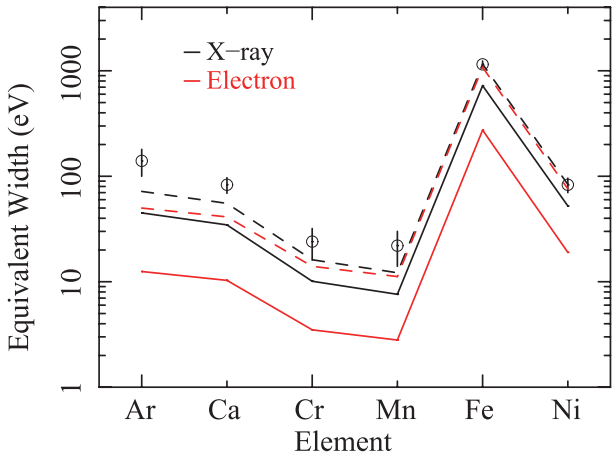

Figure 1.13. Equivalent widths of K-shell line of various neutral atoms in the GC. Black and red lines are the calculated values for the X-ray (with photon index of 1.9) and electron (with particle index of 3) scenarios, respectively. The data points marked with the open circles are the observed values. Errors were estimated at the 90% confidence level. The black and red dashed lines are to guide eyes, which are X-ray and electron scenarios in 1.6 solar and 4.0 solar abundances, respectively (Nobukawa *et al.*, 2010).

Chapter 2

Introduction

2.1 Problems in the previous study on the iron lines in the GDXE

The true origin of the GDXE would be a mixture of point sources and diffuse components. The most popular scenario is that a superposition of point sources dominates the GDXE. In fact, it seems to be crucial that Revnivtsev *et al.* (2009) resolved 80% of the iron line flux into discrete point sources in the CBF. However, the previous studies on the GDXE, especially those supporting the point-source scenario, leave several severe problems. We will consider them in the following.

1. **Is the result of 80% resolution in the CBF obtained by Revnivtsev *et al.* (2009) universal in the GDXE?**

   Previous study revealed that the GDXE is composed of the three components: the GCXE, GBXE, and GRXE. Whether they share the origin is unknown. However, there are some hints which suggests that the three components are different in character.

   Uchiyama *et al.* (2013) investigated the distribution of the 6.7 keV and 7.0 keV line intensity along the Galactic plane as shown in figure 2.1. While the intensity of the 6.7 keV (helium-like iron) line in the GCXE is 10 times as large as the GRXE, that of the 7.0 keV (hydrogen-like iron) line in the GCXE is 30 times as large as the GRXE. This result suggests that the X-ray spectrum of the GCXE is different from that of the GRXE. Even in the point-source scenario, the spectra and the mixing ratio of CVs and ABs should be different between the GCXE and GRXE.

   Also a stellar mass distribution model suggests a possibility that the mixing ratio of point sources in the CBF is different from the GC region and the Galactic plane. Colored lines in figure 2.2 show the stellar mass distribution model originally compiled by Muno *et al.* (2006), which is composed of the nuclear stellar cluster, nuclear stellar disk, Galactic disk, and Galactic bulge. Although the CBF is located near the GC, its latitudinal coordinate of $b = 1.^{\circ}4$ is a bit farther out from the Galactic plane. The arrow in figure 2.2b shows the position of the CBF, where the Galactic bulge and Galactic disk components contribute half and half. On the other hand, the central ($|l_*| < 1^{\circ}$ and $|b_*| < 0.^{\circ}2$) region is dominated by the nuclear stellar cluster and nuclear stellar disk components, and the Galactic plane ($|l| > 1^{\circ}$) is contributed mainly by the Galactic disk component. Furthermore, figure 2.2 also shows a large excess over the stellar mass distribution model in the GC region ($|l_*| < 1^{\circ}5$ and $|b_*| < 1^{\circ}$) assuming that all the other

GDXE are due to unresolved point sources. This indicates the possibility that other components than point sources are dominated the GCXE.

There is still a room for consideration about the argument that Revnivtsev *et al.* (2009) resolved 80% of the iron line flux in the CBF by Chandra and hence point sources should account for the iron lines of GDXE in other regions. We should verify whether their argument is valid throughout the GDXE: the GCXE, GBXE, and GRXE.

2. **The GDXE origin has been debated based on the observational results with limited spatial and spectral resolution.**

The GDXE has been described often by an exponential model with a scale height and a scale length (e.g. Uchiyama *et al.*, 2013). Especially the scale height would provide important information to solve the origin of the GDXE.

In the previous study, a stellar mass distribution model constructed from NIR surface brightness observed by COBE/DIRBE has been used and compared with the spatial distribution of the GDXE (Revnivtsev *et al.*, 2006a; Muno *et al.*, 2006; Uchiyama *et al.*, 2011). However, the angular resolution of the NIR maps was $0.^{\circ}7$, and thus it is not simple way to compare them to the GCXE and GRXE maps with the scale height of $\sim 0.^{\circ}5$–$0.^{\circ}7$. In fact, as shown in figure 2.2b, the scale height of the GCXE would be smaller than that of point sources (Uchiyama *et al.*, 2011). Furthermore, the NIR maps could be affected by bright stars, and hence it is uncertain that they can thoroughly follow low mass stars such as ABs and CVs.

As described in section 1.2, the iron three lines, namely 6.4 keV, 6.7 keV, and 7.0 keV lines, have different radiation mechanism. Therefore, the origin of each line could be different from each other. However, the previous studies have often not separated the three lines due to limitations of detector performance such as energy resolution and effective area (e.g. Revnivtsev *et al.*, 2006b, 2009). The previous debate over the origin of the GCXE, especially the origin of the bright 6.4 keV line emission, shows indispensability to separate each line as described in section 1.4.

Also equivalent widths[1] of the three iron lines in the GDXE are controversial issue. Uchiyama *et al.* (2013) found the equivalent widths of the 6.4 keV, 6.7 keV, and 7.0 keV lines in the GRXE are $\sim$ 110 eV, $\sim$ 490 eV, $\sim$ 110 eV, respectively (see also Ebisawa *et al.*, 2008; Yamauchi *et al.*, 2009). Averaged equivalent widths of CVs with the luminosity of 10^{30}–10^{33} erg s^{-1} are $\sim$ 130 eV for the 6.4 keV line, $\sim$ 160 eV for the 6.7 keV line, and $\sim$ 90 eV for the 7.0 keV line (Hellier *et al.*, 1998; Ezuka and Ishida, 1999; Hellier and Mukai, 2004). Suzaku archive of ABs shows that their mean equivalent widths of the 6.4 keV, 6.7 keV, and 7.0 keV lines are $\sim$ 60 eV, $\sim$ 560 eV, and $\sim$ 80 eV, respectively (Uchiyama *et al.*, 2013) .

As noted by Uchiyama *et al.* (2013) and Warwick *et al.* (2014), any mixture of well-known X-ray CVs and ABs cannot simultaneously explain the equivalent widths of the three lines in the GRXE, and faint sources with lager equivalent width than those of the well-known CVs and ABs are required in order to explain by the point-source scenario. Yuasa *et al.* (2012) found that the spectrum of the GDXE near the GC is explained by CVs with a specific mass. However, in

[1] An equivalent width is the area of the line on a plot of counts versus X-ray energy. Unit is energy (eV or keV).

order to explain the observed equivalent width, the iron abundance is required ~ 3 times larger than the typical value in the well-known CVs.

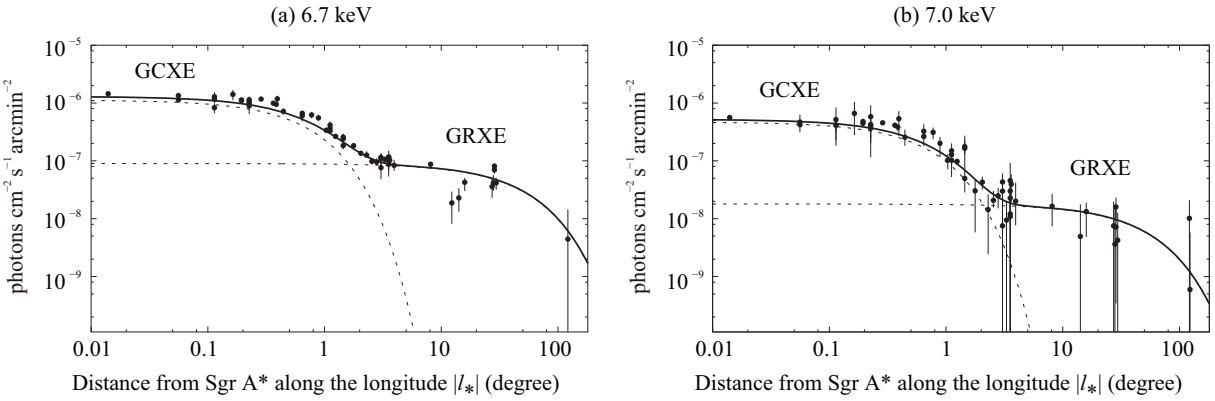

Figure 2.1. (a) 6.7 keV-line intensity distribution along the Galactic plane as a function of l_* (distance from Sgr A*). (b) 7.0 keV-line intensity along the Galactic longitude. Both the figures are taken from Uchiyama *et al.* (2013).

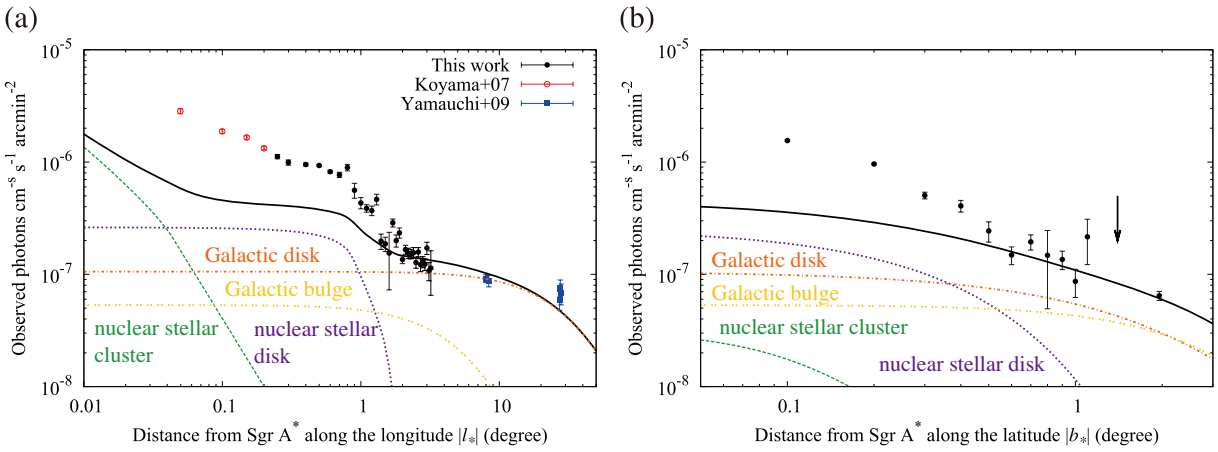

Figure 2.2. (a) 6.7 keV line intensity distribution along the Galactic plane as a function of l_* (distance from Sgr A*). The black solid line is the sum of the four components. (b) Same as the left panel (a), but those along the Galactic longitude at $l_* = -0.^\circ114$ as a function of b_* (distance from the Galactic plane). The arrow shows the position of $b = -1.^\circ4$, which is almost the same region as the CBF (Revnivtsev *et al.*, 2009). Both the figures are taken from Uchiyama *et al.* (2011).

2.2 Aim of this dissertation

The aim of this dissertation is to reveal the origin of the 6.4 keV line emission along the Galactic plane by addressing the problems laid above: (1) We confirm that the GDXE consists of the GCXE, GBXE, GRXE. (2) We separately measure their distributions (the scale heights) and spectral features (the equivalent widths) for the 6.4 keV line, and for comparison, those of the 6.7 keV and 7.0 keV lines in the GCXE, GBXE, and GRXE. (3) We investigate the origin of the 6.4 keV line emission based on the observational result.

In this dissertation, we use the Suzaku satellite. The X-ray charge coupled device camera, the XIS, onboard Suzaku provides lower background and large effective area than ever before, especially for a diffuse emission with energy above 5 keV, and thus Suzaku have demonstrated its capability to resolve the 6.4 keV, 6.7 keV, 7.0 keV lines in the GDXE. We analyze archival data from a huge number of Suzaku observations along the inner Galactic disk ($|l| \lesssim 80°$).

In chapter 3, we overview the Suzaku satellite (section 3.1), the X-ray telescope (section 3.2), and the CCD camera (section 3.3), which are the instruments we used for the observations. The detailed observation log and data reduction are described in chapter 4. In chapter 5, we make the global intensity profiles of the 6.4 keV, 6.7 keV, and 7.0 keV lines and the hard continuum and measure their scale heights to spatially resolve the GCXE, GBXE, and GRXE. We also separately obtain equivalent widths of the three lines for the GCXE, GBXE, and GRXE. In order to constrain the origin of the 6.4 keV line, we extracted X-ray spectra from the regions where the 6.4 keV line intensity is especially strong (chapter 6). In the involved regions, some XIS fields of view (FOVs) are contaminated by "stray light", which occurs by anomaly reflection of X-ray which comes from a very bright point source outside an FOV. We evaluate its effect before spectral analysis (section 6.1). We draw a conclusion for the origin of the 6.4 keV line emission from the Galactic plane in chapter 7. At the last, we briefly give prospects for ASTRO-H, the next Japanese X-ray astronomy satellite (chapter 8).

Throughout this dissertation, the distance to the GC is assumed to be 8 kpc. We call the regions in positive and negative Galactic longitude as "east" and "west", respectively. Errors quoted in this paper are at 68% confidence levels unless otherwise specified.

Chapter 3

Instrument: Suzaku X-ray Satellite

3.1 Suzaku satellite

Suzaku is the fifth Japanese X-ray astronomy satellite launched by Japan Aerospace Exploration Agency (JAXA) with the M-V Launch Vehicle from JAXA's Uchinoura Space Center on July 10, 2005. A schematic view of Suzaku is shown in figure 3.1(left). This satellite was orbiting in a near-circular path with an altitude of 550 km, an inclination of 31.9 degrees, and an orbital period of about 96 minutes. Suzaku had been operated for about 10 years exceeding its planned observation lifetime of about two years. However, its communication with the ground had been established only in fragments since June 1, 2015. The completion of its scientific mission was announced from JAXA on August 26, 2015.

Suzaku carried the X-ray spectrometer (XRS, Kelley *et al.*, 2007), the X-ray Imaging Spectrometer (XIS, Koyama *et al.*, 2007), and the Hard X-ray Detector (HXD, Kokubun *et al.*, 2007; Takahashi *et al.*, 2007). The XRS was intended to provide for the first time both a good energy resolution ($\sim$ 7 eV at 6 keV; FWHM) and a large effective area. Unfortunately, because of a liquid helium coolant loss on August 8, 2005, the XRS was no longer able to provide the planned science. We will not discuss the XRS further in this dissertation. The XIS consists of four X-ray charge-coupled device (CCD) cameras, each placed on the focal plane of each module of the X-Ray Telescope (XRT, Serlemitsos *et al.*, 2007). A side view of the instrument and telescopes are shown in figure 3.1(left).

In this dissertation, we used the data of the XIS in the energy range of 0.2–12 keV, and hence we will describe the detail of the XRT and the XIS in the following sections.

3.2 X-ray Telescope (XRT)

3.2.1 Mechanism and design

X-ray optics is completely different from that for visible light. While lenses used for visible light are produced with transparent materials that have a refractive index much larger than unity, refractive indices of matter to X-rays are less than unity. Thus the most common method to focus X-rays is reflection. X-ray reflection occurs, only when the grazing incidence angle is shallow enough ($\leq 1^\circ$).

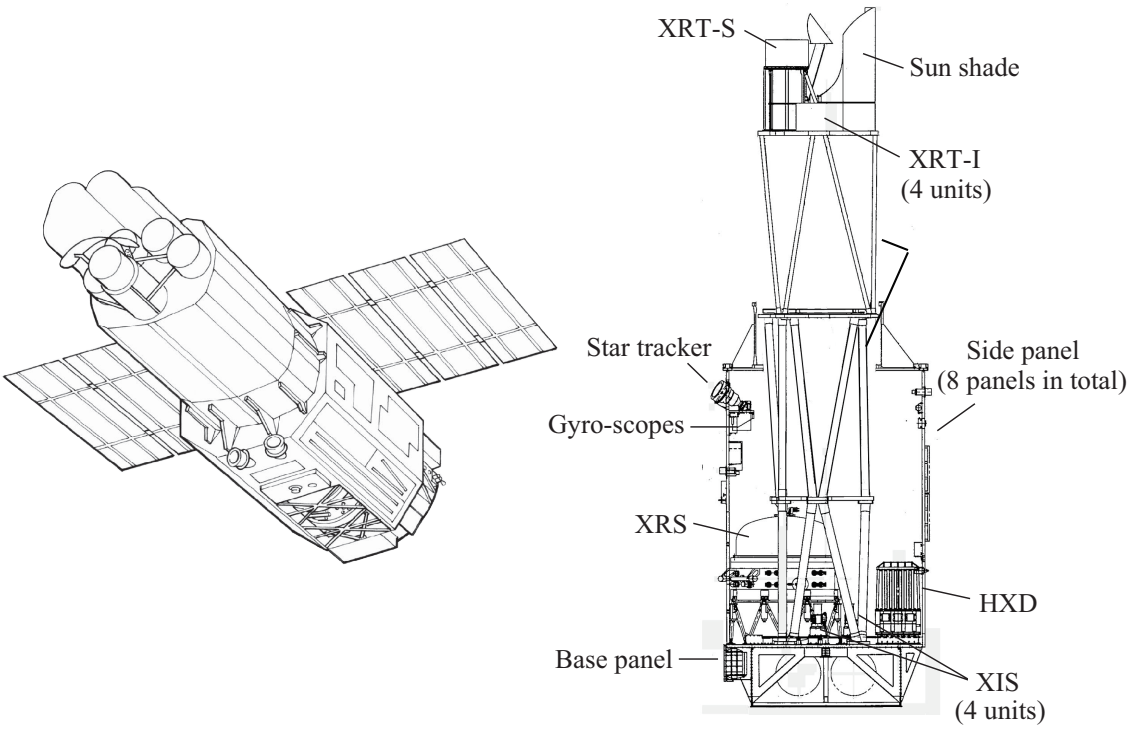

Figure 3.1. (left) Schematic picture of the Suzaku satellite. (right) Side view of the instruments and telescopes on Suzaku. Both are taken from Mitsuda *et al.* (2007)

The XRTs contain in total ~ 170 pairs of concentric thin-foil reflectors, whose thickness is only ~ 165 μm (figure 3.2). The reflectors are thin aluminum foils coated with gold as an X-ray-reflecting material. The gold layer was sputtered onto the glass tube with a highly smooth surface, and then was transferred to the foil reflectors (Serlemitsos and Soong, 1996). The incident grazing angle is $\lesssim 0.6^\circ$ so that even the outermost mirror shell can reflect the iron K-shell line. The diameter of the XRT is ~ 400 mm. The reflectors are radially nested as tight as possible, which results in an aperture efficiency as high as $\sim 60\%$. Thus the XRTs achieve at the same time a large effective area and light weight. In fact, although the total weight is only $\lesssim 80$ kg, the total effective area of the four sets of XRTs at 7 keV is comparable to that of XMM-Newton mirrors, whose total weight is ~ 1300 kg.

The XRT adopted an approximation of the Wolter-I type geometry. As shown in figure 3.3, X-rays are reflected twice on the surface of the primary and secondary reflectors and are gathered on focal plane. The shapes of the primary and secondary reflectors are a paraboloid and hyperboloid, respectively, in the original Wolter-I type optics. In Suzaku, the reflectors have a double-cone geometry to approximate the Wolter-I system (Serlemitsos *et al.*, 2007). This approximation ultimately limits the achievable angular resolution. Reflectors are fabricated in quadrant cones, and the quadrants are aligned so that the optical axes are within 2′ from the mechanical axis. The focal length is 4.75 m for the XIS.

X-rays from the FOV are correctly focused when they are reflected by the two surfaces. However, the tight nesting of the reflectors raises the possibility of reflection other than the normal reflection path; X-rays from the outside of the FOV are reflected only once by the surface or by the backside of the reflectors. When such unintended X-ray reflections cause "stray light" in the FOV. We will

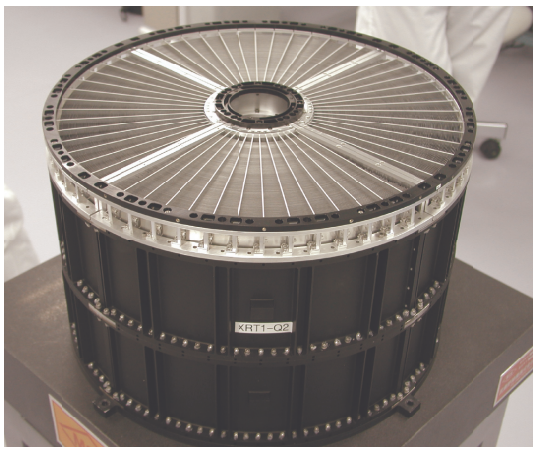

Figure 3.2. Picture of an XRT module (Serlemitsos *et al.*, 2007).

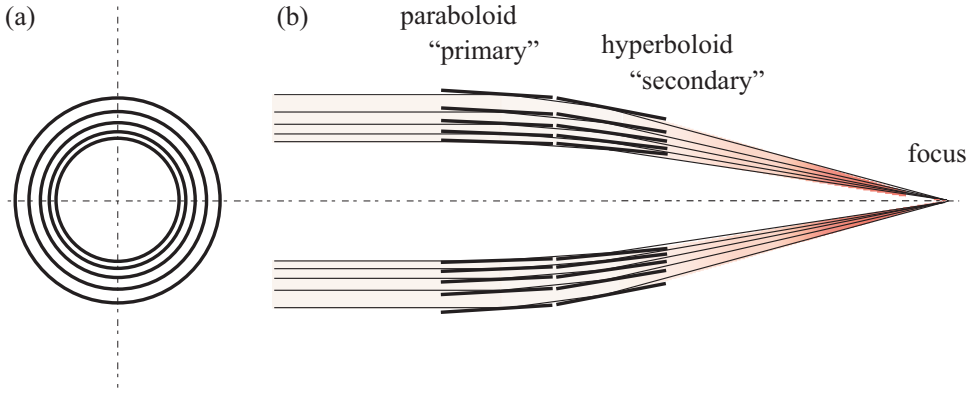

Figure 3.3. Schematic view of an X-ray telescope composed of nested reflectors: (a) front view; (b) the cross section including the optical axis (Mori *et al.*, 2005).

later describe characteristics of stray lights (section 3.2.3). In order to reduce the stray light, a pre-collimator is equipped on the top of the XRT.

The top of the pre-collimator stage is covered with a thermal shield in order to isolate the XRT thermally from the space and to keep the temperature within the XRT's designed function range of 20.0 ± 7.5°C. The thermal shield also function to block optical light from the sky and the Earth's surface illuminated by the Sun.

3.2.2 Performance

The XRTs are designed to achieve the maximum possible effective area, particularly at the energy of the iron K-shell lines even under a severe weight limit imposed by the launch vehicle for Suzaku. Thanks to the tight nesting of the reflectors, the XRTs have large effective areas (450 cm^2 at 1.5 keV, 250 cm^2 at 7 keV per module). On the other hand, the XRTs trade off the spacial resolution. In order to evaluate the spacial resolution, a half power diameter (HPD) is commonly used. The HPD is defined as the diameter within which 50% of X-rays from the focused point source are enclosed. The HPDs of the XRTs are 1.′8–2.′3, which are about one order of magnitude larger than the X-ray

telescopes onboard the other contemporary satellites such as Chandra and XMM-Newton.

An intensity profile of a point source as a function of radius from the point source is called as a point spread function (PSF). An enclosed energy function (EEF) is an integration of a PSF and shows the ratio of the flux in the enclosed circle to the total flux of a point source. The PSF and EEF of a unit of the XRTs are shown in figure 3.4.

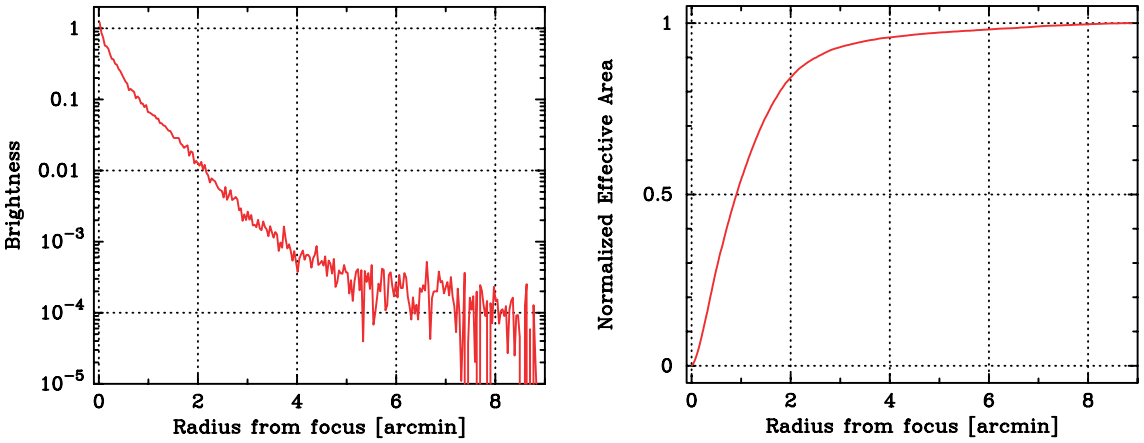

Figure 3.4. Point-spread function (PSF; left), and encircled energy functions (EEF; right) of the XRT module for XIS 0. The plots were obtained by an observation of a moderately bright point source, SS Cyg. The EEF is normalized to unity at the edge of the CCD chip (Serlemitsos *et al.*, 2007).

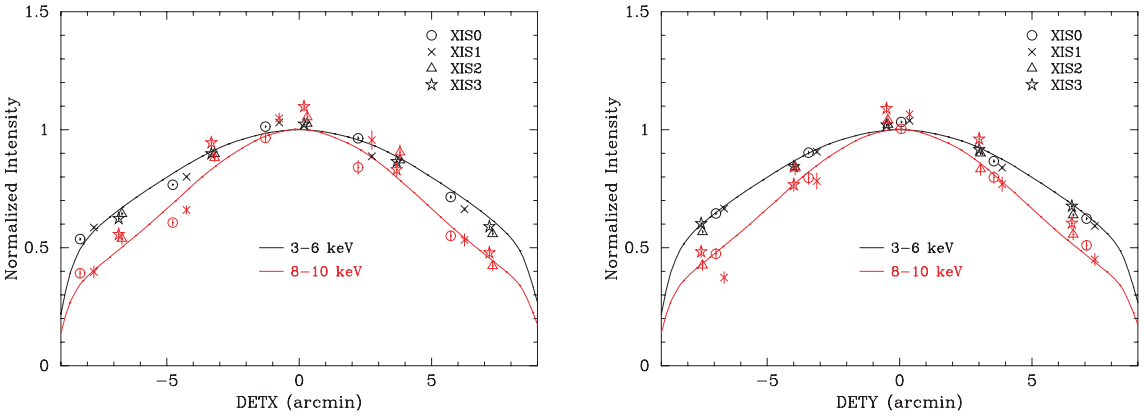

Figure 3.5. Vignetting of the four XRT-I modules using the data of the Crab Nebula observed during August 22–27, 2005 in the two energy bands of 3–6 keV and 8–10 keV. The model curves were calculated with a ray-tracing simulator with spectral parameters of $N_{\rm H} = 0.33{\times}10^{22}$ cm^{-2}, a photon index of 2.09, and normalization of 9.845 photons cm^{-2} s^{-1} keV^{-1} at 1 keV (Serlemitsos *et al.*, 2007).

The effective area for off-axis sources is smaller than that for on-axis ones. This effect is called as "vignetting", and is prominent in high energy. A critical angle is smaller for higher energy X-rays than for lower ones, and therefore less of off-axis high-energy photons reach the focal plane (see figure 3.3). Figure 3.5 shows the off-axis angle dependence of the effective area for the soft (3–6 keV) and the hard (8–10 keV) bands.

3.2.3 Stray light

There are two major components in stray light appearing in the FOV. Reflection paths causing stray light are shown in figure 3.6 as well as the normal double reflection. When an incident X-ray is reflected only once by a secondary reflector, which is so-called secondary reflection, the brightest stray light appears (figure 3.6b). The other component is referred to as backside reflection, which is the result of reflection on the backside of a primary, followed by the normal double reflection (figure 3.6c). As represented in figure 3.6, if the oblique angle of a primary reflector measured from the optical axis is defined as τ, the secondary reflection can occur when the off-axis angle of an incident X-ray θ is in the range of $\tau < \theta < 2\tau$, and the backside reflection appears in the case of $2\tau < \theta < 3\tau$. The oblique angles of all the primary reflectors are in the range of $0.^{\circ}18 < \tau < 0.^{\circ}60$. Therefore, the secondary and backside reflections can possibly cause stray images when the off-axis angle of the source is in the range of $0.^{\circ}18 < \theta < 1.^{\circ}26$ and $0.^{\circ}36 < \theta < 1.^{\circ}89$, respectively, which means that the two major components appear on the opposite sides with respect to the detector center (Mori *et al.*, 2005).

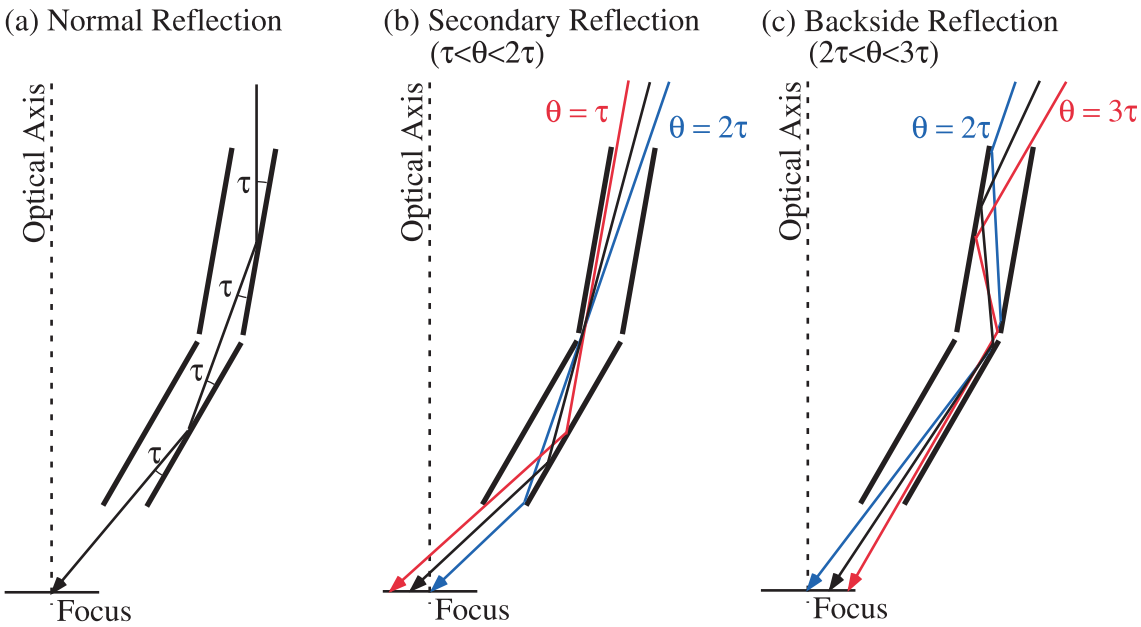

Figure 3.6. Reflection paths causing stray light as well as the normal reflection. The oblique angle of the primary reflector measured from the optical axis of the XRT is represented by τ. (a) Normal double reflection of the X-ray. (b) Secondary reflection, which can occur when the incident angle of the X-ray measured from the optical axis θ is in the range of $\tau < \theta < 2\tau$. (c) Backside reflection, which is followed by the normal double reflection. This pattern occurs in the case of $2\tau < \theta < 3\tau$ (Mori *et al.*, 2005).

Ray-tracing simulation demonstrates a capability of the pre-collimator. Figure 3.7 shows a wide-range vignetting function of the XRT at the three energies of 1.49 keV, 4.51 keV, and 8.04 keV for off-axis angles up to 80′. The pre-collimator cannot completely reduce the secondary reflection at the off-axis angle of < 30′, and also a leak of secondary reflection occurs at off-axis angle of ∼ 60′–70′ through the gap between the pre-collimator and the primary reflectors. However, the intensity of the secondary reflection is reduced by a few orders of magnitude on the average in the off-axis angle range of 20′–70′ .

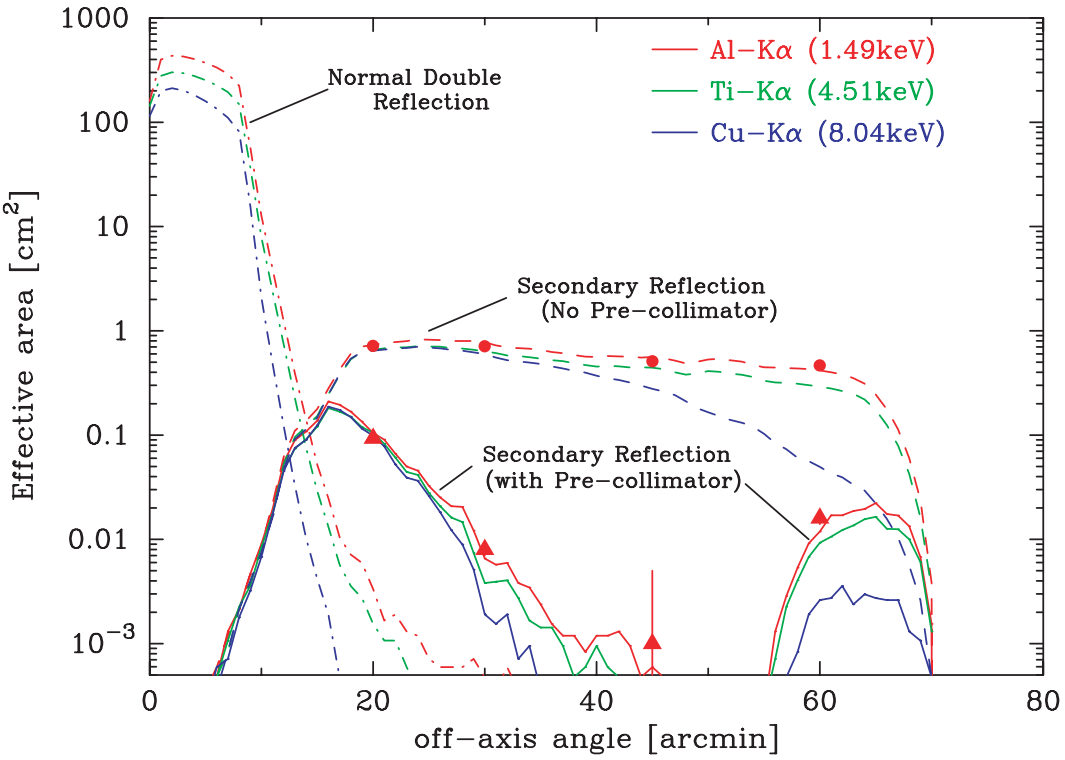

Figure 3.7. Wide-range vignetting function of the XRT at the three energies of 1.49 keV, 4.51 keV, and 8.04 keV for off-axis angles up to 80′. All of the curves were simulated by a ray-tracing simulator (Mori *et al.*, 2005).

Studies of the stray light were carried out with Crab nebula observations with off-axis angles of 20′, 50′, 65′, and 120′. Examples of mosaic images taken in the observations are shown in figures 3.8. The stray images differ from offset to offset and from azimuth to azimuth. They also strongly depend on the incident X-ray energy. The Crab observations revealed that there is discrepancy of the stray light intensity between the ray tracing simulation and observed data. The spectral shapes above 1.5 keV are well reproduced by the simulation. However, the absolute fluxes differ from the ray-tracing simulation with a factor of ~ 2. This is because the estimated gap between the pre-collimator and the primary reflectors in the simulation does not reflect the real one. Therefore stray light flux cannot be estimated by the simulation (Takata *et al.*, 2015).

Figure 3.9 shows a schematic diagram of the stray patterns for a stray light source at an azimuth angle of α and an offset angle of R. The square represents the FOV of the XIS. The FOV near side to a stray light source is contaminated by stray light of the secondary-reflection component, but at the same time free from the backside-reflection component. On the other hand, the far side of the FOV suffers from the backside component, but free from the secondary component. There is another stray light free region corresponding to the quadrant boundary with a cone angle of 12.°8 at an azimuth angle of 45° with a 90° pitch (the white radial lines in figure 3.9).

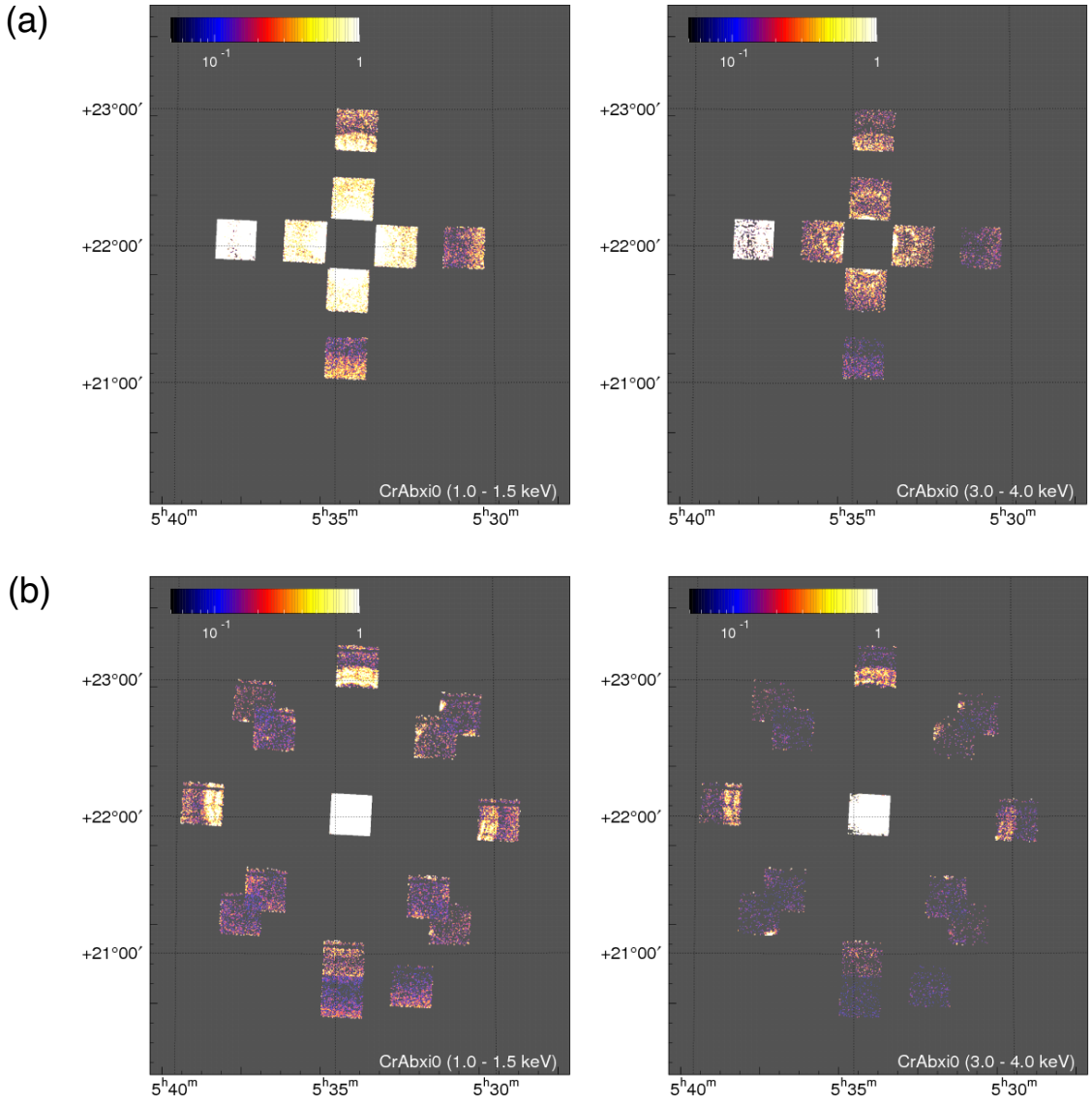

Figure 3.8. Mosaic images of offset observations of an extremely bright point source, Crab, in the sky coordinate (right ascension and declination). (a) Observation with off-axis of 20′ and 50′. (b) Same as (a), but with aff-axis of 50′ and 65′ (Suzaku Technical Description).

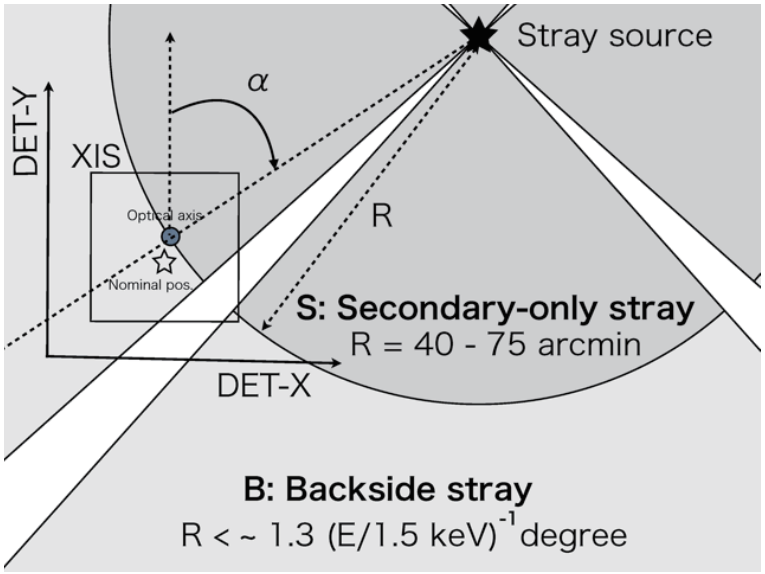

Figure 3.9. Schematic diagram of stray light patterns for a stray source at an azimuth angle of α and offset angle of R. The square shows the FOV of the XIS. This figure is taken from Suzaku Technical Description.

3.3 X-ray Imaging Spectrometer (XIS)

3.3.1 X-ray CCDs

The XIS consists of MOS-type CCDs, in which each pixel is composed of metal (poly-silicon), oxide (silicon dioxide) as an insulator and p-type semiconductor (silicon). When an X-ray photon enters into the depletion layer in a CCD, photo-electrons are created and then electron-hole pairs are generated. The number of the generated electrons is proportional to the incident photon energy. The average energy required to produce an electron-hole pair is 3.65 eV for silicon. The electrons and holes are separated by the electronic field in the depletion layer before they recombine. The electrons are collected into the potential wells under the electrodes as signal charges. After an exposure period, the voltages of the electrodes are clocked to transfer the signal charges to the readout nodes.

The XIS adopted frame transfer CCDs, which consist of two distinct area: an imaging area and a frame-store region as shown in figure 3.10. Whereas the imaging area is exposed, the frame-store region is shielded from X-rays. Each CCD chip is composed of four segments called segment A, B, C, and D. Each segment has its own readout node. After a certain exposure period, the integrated signal charges are transferred in a short time from the imaging area to the frame-store region. The charges in the frame-store region are transferred vertically to the horizontal shift register by each row. At the end, the signal charges in the horizontal shift register are transferred to the readout node by each pixel. This sequence is repeated until all the pixels in the frame-store region are read out. When the charges are transferred to the frame-store region, new exposure starts in the imaging region. The exposures and readouts are performed continuously. The coordinates describing the actual pixel location on the chip are named ACTX and ACTY coordinates (see figure 3.10).

Figure 3.11 shows a photograph and cross section of the XIS sensor. Each XIS sensor has a single CCD chip. Figure 3.12 shows a photograph of the CCD installed in the base. The imaging area of the CCD has 1024×1024 pixels, and the pixel size is 24μm$\times 24\mu$m. Combined with the XRT, the imaging area covers the $18' \times 18'$ region in the sky. Each XIS sensor has three ^{55}Fe calibration sources. One is for the ground calibration and initial orbit calibration, and is attached to the door. For normal observations, this calibration source is out of the FOV because the door was opened. The other calibration sources illuminate the two far-end corners from the read-out node of the imaging area.

The XIS employs two types of CCDs: front-illuminated (FI) and back-illuminated (BI). Three (XIS 0, 2, and 3) of the four sensors are FI type whereas the other (XIS 1) is BI type. The front side of the CCDs have a structure of electrode and insulator made of poly-silicon and silicon dioxide layers, whose thicknesses are ~ 0.28 μm and ~ 0.44 μm, respectively. The FI CCDs are less sensitive than the BI CCD to X-rays in the < 2 keV band because the front-side structure absorbs soft incident X-rays. On the other hand, the depletion layer of the FI CCDs is thicker (~ 65 μm) than that of the BI CCD (~ 42 μm), and hence the FI CCDs have high quantum efficiency to hard X-rays than the BI CCD (figure 3.13). The whole region of XIS 2 and the segment-A of XIS 0 have been out of function since 2006 November and 2009 June, respectively, possibly due to micro-meteorite impact on the CCDs.

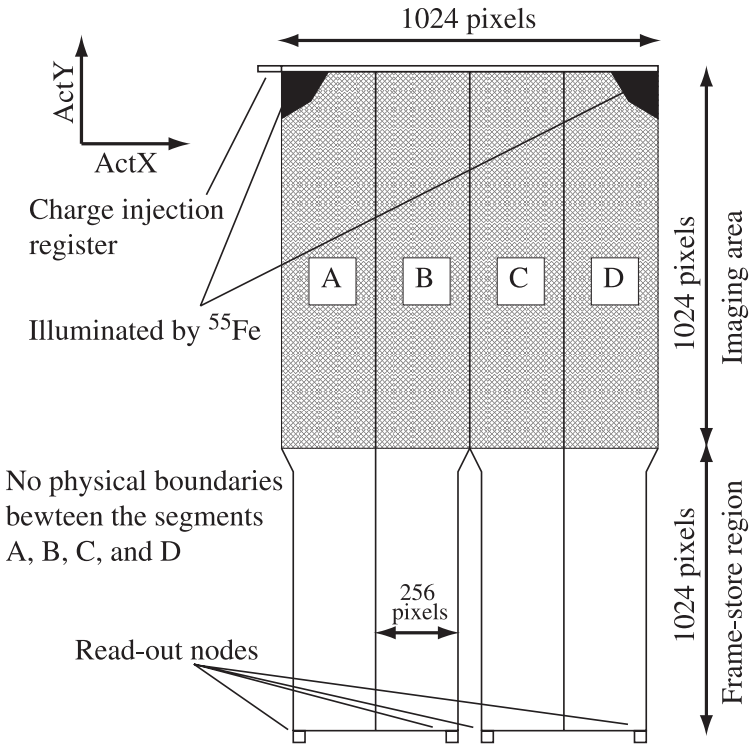

Figure 3.10. Schematic view of the XIS CCD (Koyama *et al.*, 2007).

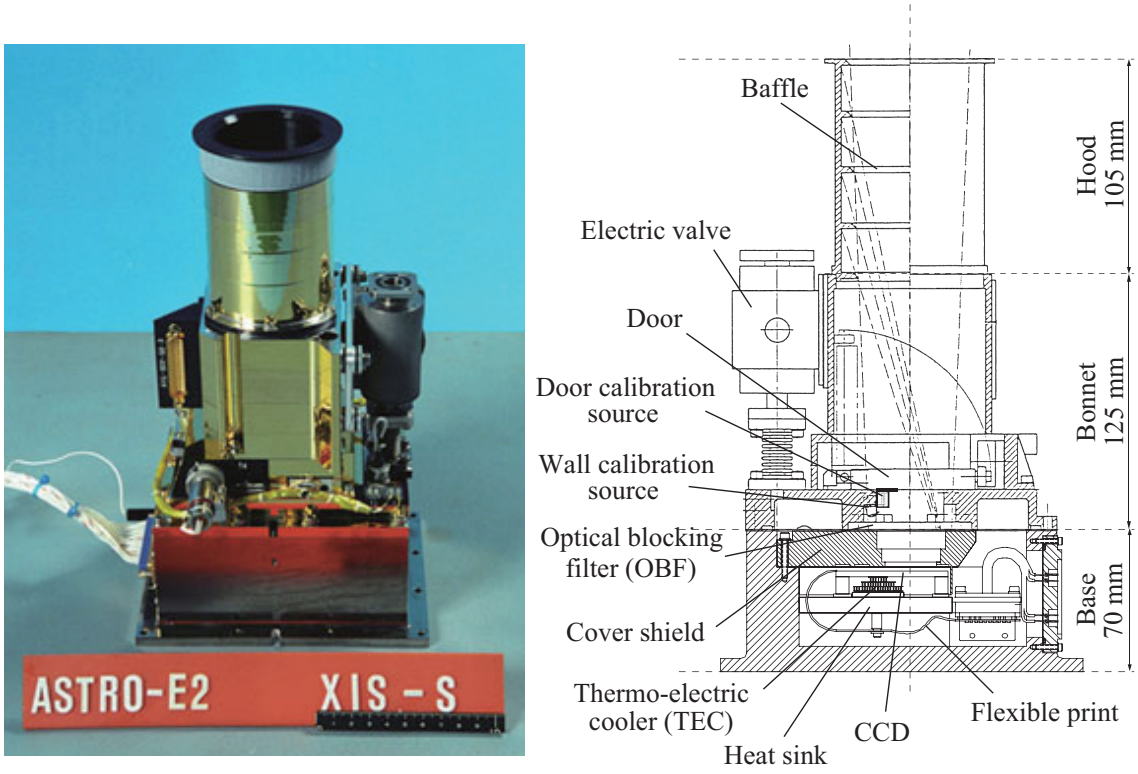

Figure 3.11. Picture (left) and cross section (right) of the XIS sensor (Koyama *et al.*, 2007).

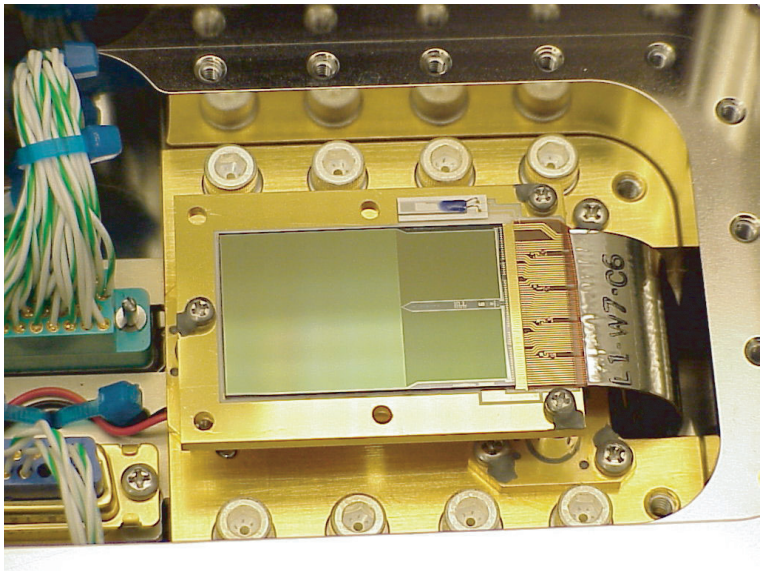

Figure 3.12. Picture of the XIS CCD installed in the base (Koyama *et al.*, 2007).

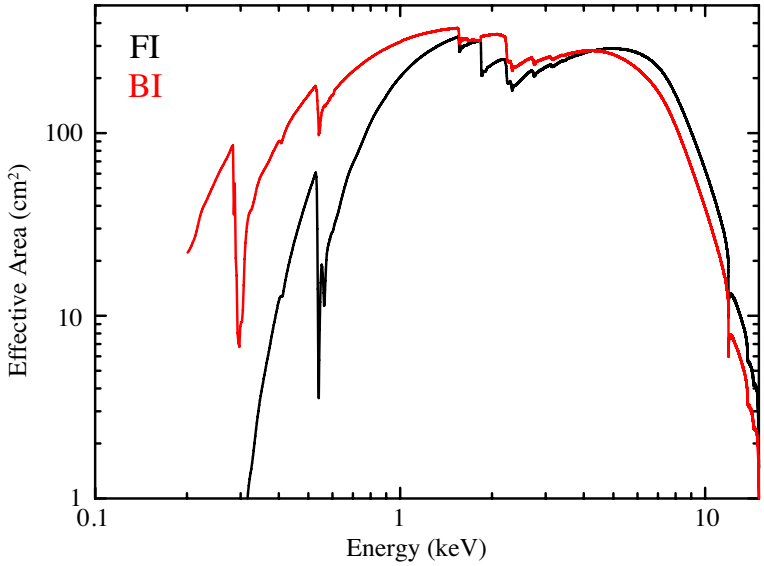

Figure 3.13. Effective area of one XRT+XIS system. The FI CCDs (XIS 0, 2, and 3) have larger effective area than the BI CCD (XIS 1) in the high energy band of $\gtrsim 5$ keV.

3.3.2 Energy response

The pulse height distribution of the signals for a monochromatic incident X-ray energy is called a response function of the detector. The schematic distribution of the XIS response is shown in figure 3.14. The XIS response consists of at least six components: (1) a main peak, (2) a sub peak, (3) a triangle component, (4) a silicon escape, (5) a silicon line, and (6) a constant component (Matsumoto *et al.*, 2006). The main-peak component is made in the case where X-ray photons are absorbed in the depletion layer of the CCD and all electrons are collected as signal. The sub-peak, triangle and constant components come from events in which a part of charges are lost. The silicon escape line appears at the pulse height channel lower than the main peak by 1.74 keV (which is the energy of

the silicon Kα line). The silicon escape event happens when a fluorescent silicon X-ray photon is generated by a photoelectric absorption and the photon escapes from the pixel that absorbed the incident X-ray photon. The silicon Kα line at 1.74 keV occurs when the fluorescent silicon photon is absorbed in another pixel.

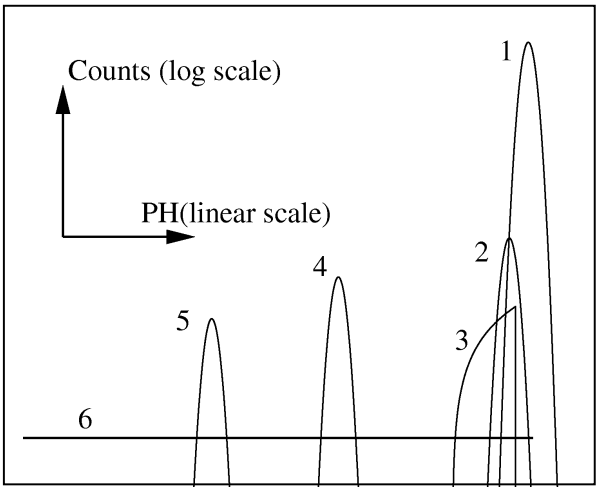

Figure 3.14. Schematic description of the XIS response, which consists of six components: (1) main peak, (2) sub peak, (3) triangle component, (4) silicon escape, (5) silicon Kα line, and (6) constant component (Matsumoto *et al.*, 2006).

3.3.3 Performance and calibration

CCDs in orbit suffer radiation damage in a space environment; for example, cosmic rays generate charge traps that capture signal carriers and increase the charge transfer inefficiency (CTI). The resulting pulse heights of the charge generated in a pixel with a given energy depend on the distance between the pixel and the readout node. Since the charge loss is a stochastic process, the amount of lost charge fluctuates, and energy resolution degrades.

In order to reduce the CTI, a spaced-row charge injection (SCI) technique has been introduced into the XIS (Prigozhin *et al.*, 2000; Bautz *et al.*, 2004; LaMarr *et al.*, 2004). The principle of the SCI technique is to inject artificial charges into given pixels[1] from serial registers attached to the top of each column (Bautz *et al.*, 2004; Nakajima *et al.*, 2008; Uchiyama *et al.*, 2009; Ozawa *et al.*, 2009). The injected charges fill traps so that subsequent charges are transferred with less charge loss.

Figure 3.15 shows the long-term trend of the measured peak energy and width of the manganese Kα line (5.9 keV) from the calibration sources. The peak energy decreases whereas the width increases gradually. In the middle of 2006, the SCI technique was put into routine operation, which resulted in a drastic improvement of the gain and energy resolution. The amount of charges were equivalent to that generated by a 6 keV X-ray photon (6 keV-equivalent) for the FI devices whereas the smaller amount of 2 keV-equivalent was injected for the BI device in oder to decrease the expected SCI-related increase in noise in the soft X-ray band, where the BI device has an advantage over the FI devices. The long-term trend in XIS1 had shown increment of the CTI at a faster rate,

[1] In the case of the XIS, the artificial charges are injected periodically in space: every 54 rows.

and therefore, the injected charge amount was changed from 2 keV to 6 keV equivalent also for the BI sensor in 2011.

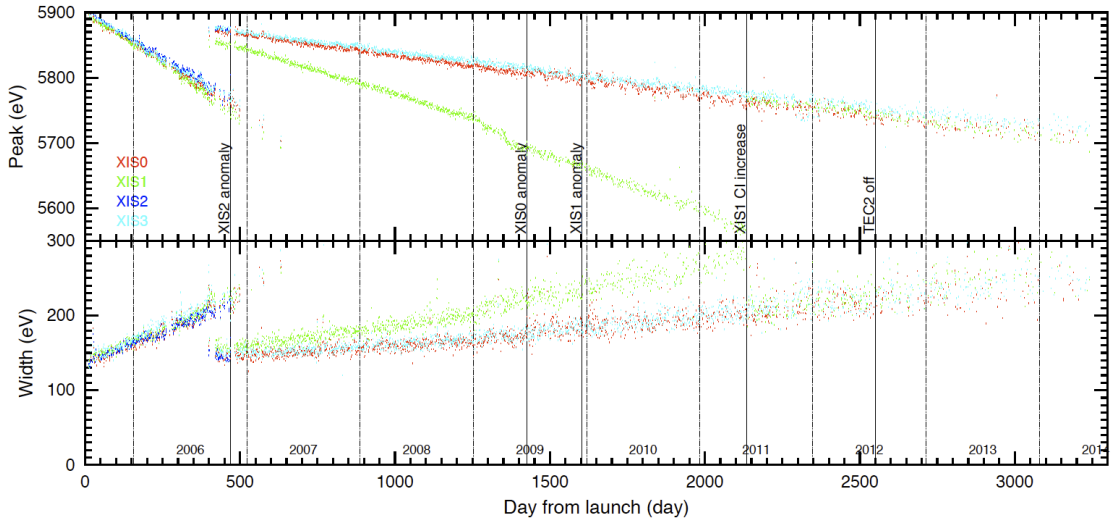

Figure 3.15. Gain history of manganese Kα line for uncalibrated data of the XIS (Suzaku Technical Description).

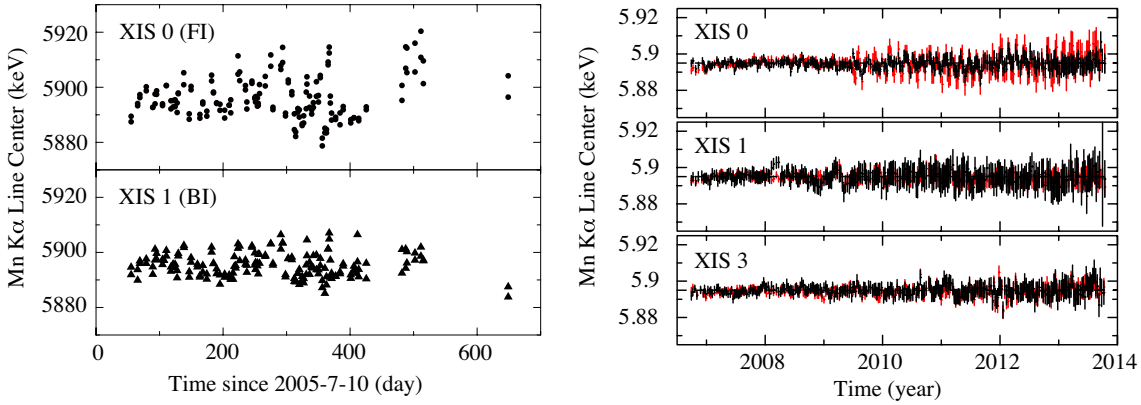

Figure 3.16. Gain history of manganese Kα line for calibrated data of the XIS before turning on the charge injection technique (left) and after (right). The black and red data in the right panel show the segment A and D of each sensor, respectively (Suzaku Technical Description).

Although the SCI technique extremely improves the gain and energy resolution, the degree of CTI depends on the distance from the preceding charge-injected row, and hence the SCI technique can cause positional variations in gain on the CCD chip. This results in degradation of the energy resolution and the determination accuracy of the incident energy. Therefore, all the XIS data in the SCI mode are calibrated with a new method to correct the non-uniformity of the pulse heights. The details of the CTI correction are described in Uchiyama *et al.* (2009).

Figure 3.16 shows the time history of the center energy of the manganese Kα line in the calibrated data. The center energy has been constantly 5.895 keV. The uncertainty of the energy-scale determination is less than $\sim$ 20 eV (0.3%). The energy resolution of the XIS is defined as the width

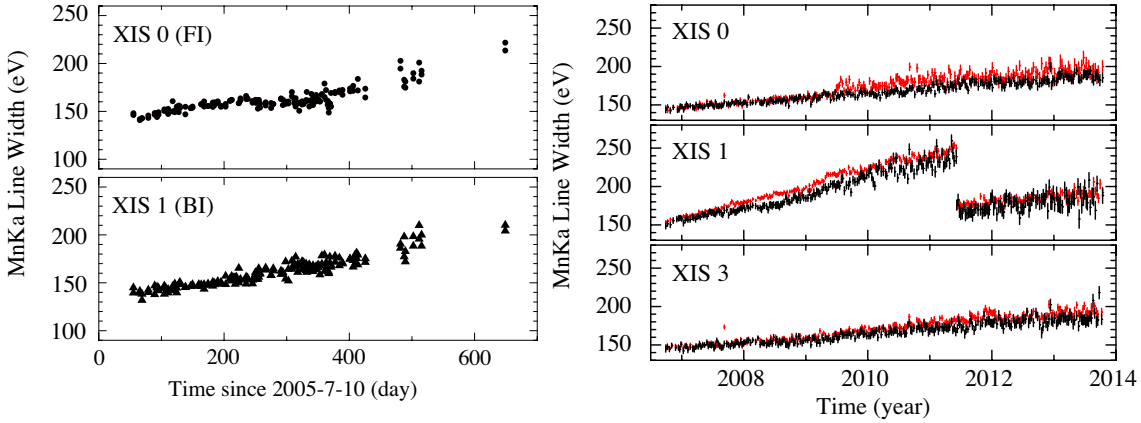

Figure 3.17. Energy-resolution history of manganese Kα line for calibrated data of the XIS before turning on the charge injection technique (left) and after (right; Suzaku Technical Description). The black and red data in the left panel show the segment A and D of each sensor, respectively.

of the main peak in the response function. The time history of the line widths of manganese Kα is shown in figure 3.17. The energy resolution of the BI, which had degraded more rapidly than that of the FI in the SCI mode, was improved by the change of the injected charge amount.

3.3.4 Non X-ray background

One of the advantages of the XIS compared with Chandra and XMM-Newton is its low and stable non X-ray background (NXB; figure 3.18), which is thanks to its lower altitude of the orbit. It is known that the NXB of the XIS is very stable on time scales of months and thus the NXB spectrum can be constructed using data obtained when the spacecraft is pointed toward the Earth at night. The NXB of the XIS is caused by ionization losses of charged cosmic-ray particles, fluorescence X-rays from materials used in the spacecraft, and the ^{55}Fe calibration sources. Figure 3.19 shows spectra of the NXB extracted from the whole region of the CCD, except for the regions illuminated by the calibration sources. The spectra show fluorescence lines from aluminum, silicon, gold, manganese, and nickel in the XIS and the XRT. The 5.9 keV and 6.5 keV lines are due to scattered X-rays from the calibration sources (manganese Kα and Kβ). The XIS 0 shows relatively strong manganese K-shell lines, which is due to stray X-rays from the ^{55}Fe calibration source although the reason is unknown why the radiation was detected outside the calibration source regions. The background counting rate in the 0.4–12 keV band is 0.1–0.2 counts s^{-1} for the FI CCDs and 0.3–0.6 counts s^{-1} for the BI CCD.

The intensity of the NXB is not uniform over a CCD chip. Figure 3.20a represents position dependence of the NXB. When the pixel position is farther from the readout node (namely, larger ACTY), the NXB becomes higher. This is because some fraction of the NXB is generated in the frame-store region and pixels in larger ACTY take longer time to be read out: the integrated intensity of the NXB during readout becomes higher in larger ACTY pixels. The NXB strongly depends on the geomagnetic cut-off rigidity. Figure 3.20b shows the NXB count rate as a function of the cut-off rigidity. Tawa *et al.* (2008) successfully modeled the NXB spectra as a function of the cut-off rigidity and the position on the CCDs. The model reproduce the NXB spectra within the accuracy of 5%.

The good energy resolution, large effective area, and the low and stable NXB background of the

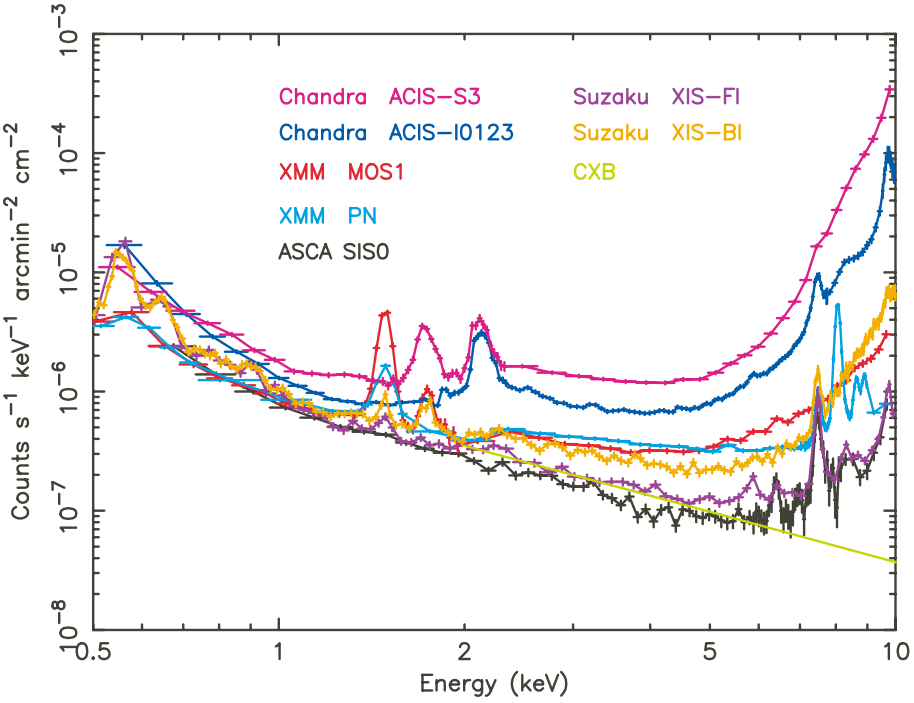

Figure 3.18. Background counting rate as a function of energy for the XIS and other instruments (Mitsuda *et al.*, 2007). The background rate was normalized with the effective area and the field of view, which is a good measure of the sensitivity determined by the background for spatially extended sources.

XIS offer a good spectral performance especially for diffuse sources with low surface brightness such as the GDXE in the 5–10 keV band, including iron K-shell lines.

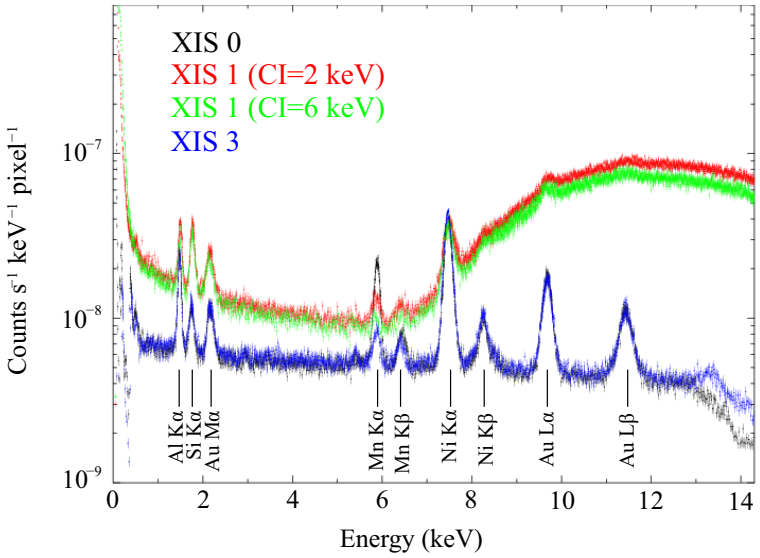

Figure 3.19. Spectra of the NXB for XIS0 (black), XIS1 (CI=2 keV: red, CI=6 keV: green), and XIS3 (blue), which are constructed from night Earth observations (Suzaku Technical Description).

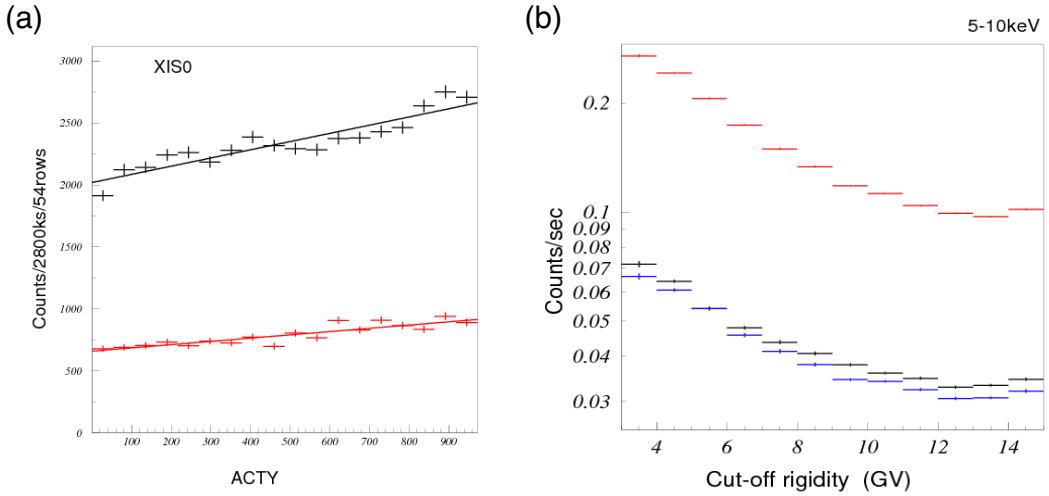

Figure 3.20. Coordinate and cut-off rigidity dependency of the NXB. (a) Coordinate dependence of the intensity of the NXB for XIS 0. Black lines indicate the continuum component (2.5–5.5 keV), while the red lines indicate the nickel Kα line component (7.2–7.8 keV). (b) Cut-off rigidity dependency of the NXB (average intensity for 5–10 keV). Both are taken from Suzaku Technical Description.

Chapter 4

Observations and Data Reductions

In this dissertation, we used the Suzaku observation data of the Galactic plane, including the series of the Key and Large projects on and near the Galactic center region as well as the archival data. We chose the data which were obtained in the normal clocking mode without window option. We reprocessed the cleaned data by using `xispi` in the analysis software package HEAsoft, and the Suzaku calibration database (`CALDB`) version 2015 March. The observation log is listed in table 4.1. We used in total 153 pointings with the total exposure time of 8.8 Ms. This is 2.5 times larger than the data set analyzed by Uchiyama *et al.* (2013).

Using `xissimarfgen` (Ishisaki *et al.*, 2007) and `xisrmfgen`, the effective area of the XRT and the response of the XIS were calculated. The ancillary response files (`arf`) and redistribution file (`rmf`) for the XIS sensors were produced for each observation. The NXB with the cut-off rigidity values was estimated with `xisnxbgen` (Tawa *et al.*, 2008) released by the Suzaku team. We subtracted the NXB from the raw spectral data with the same cut-off rigidity.

Table 4.1. Observation log.

Obs. ID	Pointing direction		Obs. start	Exp.[a]	XIS 2[b]	Win.[c]	CI[d]	Target name
	l (°)	b (°)	(UT)	(ks)				
100026020	347.63	0.71	2005-09-25 19:11:40	34.9	OK	-	off	RXJ1713−3946−BKGD1
100026030	345.81	−0.54	2005-09-28 07:09:13	37.5	OK	-	off	RXJ1713−3946−BKGD2
100027020	359.76	−0.05	2005-09-24 14:17:17	42.8	OK	-	off	Sgr_A_west
100028010	332.40	−0.15	2005-09-19 12:00:02	41.4	OK	-	off	HESS J1616−508
100028020	332.00	−0.15	2005-09-18 22:47:36	19.3	OK	-	off	HESS J1616−508_BGD1
100028030	332.70	−0.15	2005-09-20 19:40:17	21.9	OK	-	off	HESS J1616−508_BGD2
100037010	359.76	−0.05	2005-09-29 04:35:41	43.7	OK	-	off	Sgr_A_west
401026010	25.27	−0.10	2007-03-05 12:49:14	42.2	-	-	on	HESS J1837−069
401052010	340.00	0.11	2006-09-09 09:12:56	22.5	OK	-	off	IGRJ16465−4507
401054010	341.32	0.58	2006-10-05 21:10:30	21.2	OK	-	off	IGRJ16493−4348
401056010	333.49	0.30	2006-09-20 20:25:12	39.1	OK	-	off	IGRJ16195−4945
401092010	9.94	−0.27	2006-09-09 22:13:43	48.9	OK	-	off	SGR 1806−20
401101010	12.87	0.01	2007-03-01 21:35:58	63.8	-	-	on	HESSJ1813−178
402094010	9.95	−0.27	2007-10-14 05:35:49	52.2	-	-	on	SGR 1806−20
403005010	288.24	−0.47	2008-11-30 23:02:01	100.4	-	-	on	1E 1048.1−5937
404020010	33.17	0.84	2010-03-12 00:22:33	34.9	-	-	on	V603 AQL
404056010	338.00	0.08	2010-03-12 23:40:40	50.6	-	-	on	IGRJ16393−4643
404081010	29.77	−0.20	2009-04-15 19:37:17	104.3	-	-	on	PSR J1846−0258
405025010	311.64	0.22	2011-01-28 13:24:43	24.6	-	-	on	EMS0918
405027010	340.44	−0.18	2011-02-11 03:42:23	20.9	-	-	on	EMS01095
405028010	54.62	0.11	2010-04-27 10:28:40	23.9	-	-	on	EMS1308
406069010	10.00	−0.23	2012-03-24 10:47:46	70.6	-	-	on	SGR 1806−20
406078010	340.17	−0.12	2012-02-23 22:39:06	149.8	-	-	on	IGRJ16479−4514
407018010	333.61	−0.20	2012-08-21 23:55:27	40.5	-	XIS3	on	AX J1622.1−5005
407020010	333.72	0.22	2012-08-19 12:30:06	44.3	-	-	on	AX J1620.7−4942
407021010	316.98	0.19	2012-08-04 06:47:27	41.1	-	XIS3	on	AX J1445.7−5931
407091010	333.89	0.41	2012-08-18 19:16:15	29.3	-	-	on	J1620−4927
407092010	8.14	0.19	2012-09-21 08:05:31	32.0	-	-	on	J1803−2149
407094010	322.06	−0.42	2012-08-15 15:34:02	30.0	-	-	on	J1522−5734
408021010	352.17	−0.27	2013-09-05 00:04:43	37.3	-	-	on	CXO J172641.7−354052
500007010	8.44	−0.05	2006-04-06 14:41:18	37.5	OK	-	off	HESS J1804−216
500008010	8.04	−0.04	2006-04-07 11:49:16	40.7	OK	-	off	HESS J1804−216 BGD
500009010	28.46	−0.21	2005-10-28 02:40:08	93.3	OK	-	off	GALACTIC RIDGE
500009020	28.46	−0.21	2006-10-15 02:15:12	98.9	OK	-	on	GALACTIC RIDGE
501008010	359.84	−0.19	2006-09-26 14:18:16	129.6	OK	-	on	GC SOUTH
501009010	359.93	0.18	2006-09-29 21:26:07	51.2	OK	-	on	GC SOUTH BGD
501042010	331.57	−0.53	2006-09-15 16:00:48	40.2	OK	-	off	HESS J1614-518
501043010	330.40	−0.38	2006-09-16 11:02:03	43.6	OK	-	off	HESS J1614-518 BG
501044010	17.87	−0.70	2006-10-17 19:37:16	50.3	OK	-	off	HESS J1825-137
501045010	18.44	−0.84	2006-10-19 04:03:16	52.2	OK	-	off	HESS J1825-137 BG
501046010	359.83	0.34	2007-03-10 15:03:10	25.2	-	-	on	GALACTIC CENTER
501052010	358.50	−0.00	2006-10-10 06:45:09	21.0	-	-	on	GALACTIC CENTER
501053010	358.17	−0.00	2006-10-10 21:18:59	23.4	-	-	on	GALACTIC CENTER
501060010	1.50	0.00	2007-03-17 05:07:04	68.1	-	-	on	GC SGR D EAST
501099010	287.89	−0.37	2006-06-05 13:21:42	76.9	OK	-	off	CAR-D1
501105010	348.80	−0.54	2007-02-23 08:36:38	20.7	-	-	off	HESS J1718-385
502001010	11.95	−0.09	2007-10-02 14:17:21	53.8	-	-	on	G12.0-0.1

[a] Effective exposure time of the cleaned data.

[b] Availability of the XIS 2 sensor.

[c] The sensor which is not used for analysis because its observation is performed in the window mode.

[d] The SCI technique was operated (on) or not (off) in the observation.

Table 4.1. Observation log.

Obs. ID	Pointing direction		Obs. start	Exp.[a]	XIS 2[b]	Win.[c]	CI[d]	Target name
	l (°)	b (°)	(UT)	(ks)				
502002010	0.17	−0.67	2007-10-09 16:40:54	23.2	-	-	on	GC14
502003010	359.83	−0.67	2007-10-10 03:41:13	21.5	-	-	on	GC15
502004010	0.17	−1.00	2007-10-10 15:21:17	19.9	-	-	on	GC16
502005010	359.83	−1.00	2007-10-11 01:01:17	20.6	-	-	on	GC17
502006010	0.17	0.33	2007-10-11 11:34:01	22.6	-	-	on	GC18
502007010	0.17	0.66	2007-10-11 23:09:15	22.0	-	-	on	GC19
502008010	359.83	0.66	2007-10-12 09:52:59	23.8	-	-	on	GC20
502009010	1.83	−0.00	2007-10-12 21:52:24	22.9	-	-	on	GC21
502049010	344.26	−0.22	2008-03-25 11:00:23	215.7	-	-	on	HESS J1702-420
502053010	15.82	−0.85	2007-10-07 02:16:29	71.5	-	-	on	M17 EAST BKG
502059010	360.00	−2.00	2007-09-29 01:40:51	136.8	-	-	on	GALACTIC BULGE
502068010	296.03	−0.32	2007-08-09 06:05:33	77.2	-	-	on	G296.1-0.5N
502077010	54.06	0.21	2007-10-30 15:56:49	101.6	-	-	on	G54.1+0.3
503007010	0.33	0.17	2008-09-02 10:15:27	52.2	-	-	on	GC_LARGEPROJECT1
503008010	0.00	−0.38	2008-09-03 22:53:29	53.7	-	-	on	GC_LARGEPROJECT2
503014010	357.90	−0.05	2008-09-18 04:46:49	59.7	-	-	on	GC_LARGEPROJECT8
503015010	357.65	−0.05	2008-09-19 07:33:05	61.4	-	-	on	GC_LARGEPROJECT9
503016010	357.40	−0.05	2008-09-22 06:47:49	57.4	-	-	on	GC_LARGEPROJECT10
503017010	357.15	−0.05	2008-09-23 08:08:10	56.5	-	-	on	GC_LARGEPROJECT11
503018010	356.90	−0.05	2008-09-24 09:27:54	31.9	-	-	on	GC_LARGEPROJECT12
503018020	356.90	−0.05	2008-10-03 18:05:13	13.3	-	-	on	GC_LARGEPROJECT12
503018030	356.90	−0.05	2009-02-19 07:32:01	12.9	-	-	on	GC_LARGEPROJECT12
503019010	356.65	−0.05	2009-02-19 16:37:49	56.8	-	-	on	GC_LARGEPROJECT13
503020010	356.40	−0.05	2009-02-21 01:15:55	66.2	-	-	on	GC_LARGEPROJECT14
503022010	356.00	0.70	2009-03-18 23:11:24	41.3	-	-	on	LOOP 1 L=356.00
503023010	356.33	0.70	2009-03-26 06:37:01	31.2	-	-	on	LOOP 2 L=356.33
503026010	5.89	−0.38	2008-04-06 07:34:41	31.7	-	-	on	HESS J1800−240B
503027010	5.72	−0.06	2008-04-07 00:21:13	31.0	-	-	on	HESS J1800−240C
503028010	17.61	−0.84	2008-10-15 21:49:50	57.2	-	-	on	HESS J1825−137
503029010	17.73	−0.44	2008-10-17 11:01:12	57.2	-	-	on	HESS_J1825-137_2
503030010	17.47	−0.58	2008-10-19 04:41:55	55.5	-	-	on	HESS_J1825-137_3
503072010	359.58	0.17	2009-03-06 02:39:12	140.6	-	-	on	EXTENDED CHIMNEY
503073010	331.30	−0.76	2008-09-20 18:18:35	53.7	-	-	on	HESSJ1614−A
503074010	331.47	−0.64	2008-09-21 13:31:03	52.6	-	-	on	HESSJ1614−B
503078010	11.03	0.07	2008-03-31 14:05:55	51.5	-	-	on	HESS_J1809-193_N
503079010	10.84	0.04	2008-04-01 16:33:52	44.2	-	-	on	HESS_J1809-193_S
503081010	0.03	−1.66	2009-03-09 15:41:50	59.2	-	-	on	GC(0,−1.6)
503087010	12.82	−0.02	2009-03-04 19:45:39	56.2	-	-	on	G12.8−0.0
503099010	359.78	1.13	2009-03-10 19:39:08	29.7	-	-	on	GCL1
503103010	359.99	1.20	2009-03-11 10:56:59	18.3	-	-	on	SLX 1737−282
503108010	348.92	−0.45	2008-08-28 05:36:23	23.5	-	-	on	HESS J1718−385
504001010	358.53	−0.26	2010-02-26 09:15:00	51.2	-	-	on	HESS J1745−303A
504002010	358.47	−0.58	2010-02-27 16:14:41	53.1	-	-	on	HESS J1745−303B
504003010	358.55	−0.87	2010-02-25 04:33:17	50.9	-	-	on	HESS J1745−303C
504034010	314.40	−0.14	2010-01-13 13:49:39	104.1	-	-	on	HESS J1427−608
504036010	357.71	−0.12	2009-08-29 12:05:20	136.5	-	-	on	TORNADO
504043010	40.17	−0.88	2009-04-15 03:40:44	24.5	-	-	on	ASO0431

[a] Effective exposure time of the cleaned data.

[b] Availability of the XIS 2 sensor.

[c] The sensor which is not used for analysis because its observation is performed in the window mode.

[d] The SCI technique was operated (on) or not (off) in the observation.

Table 4.1. Observation log.

Obs. ID	Pointing direction		Obs. start	Exp.[a]	XIS 2[b]	Win.[c]	CI[d]	Target name
	l (°)	b (°)	(UT)	(ks)				
504044010	65.88	−0.33	2009-05-23 15:19:43	38.7	-	-	on	ASO0449
504045010	285.07	−0.49	2009-07-08 08:12:56	22.8	-	-	on	ASO0218
504046010	65.26	0.41	2009-04-07 18:02:07	20.5	-	-	on	ASO0447
504049010	356.29	0.99	2009-09-08 03:36:55	17.9	-	-	on	ASO0376
504050010	0.10	−1.42	2010-03-06 03:55:37	100.4	-	-	on	NONE
504052010	26.45	0.13	2009-04-13 15:32:05	41.1	-	-	on	ASO0418
504077010	11.61	−0.25	2009-09-09 04:55:29	51.9	-	-	on	HESS J1809−193A
504078010	11.33	−0.06	2009-09-10 11:36:47	52.5	-	-	on	HESS J1809−193B
504079010	10.72	0.33	2009-09-11 17:59:44	51.0	-	-	on	HESS J1809−193E
504088010	360.00	−0.83	2009-10-14 11:30:56	47.2	-	-	on	GALACTIC_BULGE1
504089010	359.95	−1.20	2009-10-09 04:05:59	55.3	-	-	on	GALACTIC_BULGE2
504090010	358.51	−1.18	2009-10-13 04:17:20	41.3	-	-	on	GALACTIC_BULGE7
504091010	358.50	−1.60	2009-09-14 19:37:36	51.3	-	-	on	GALACTIC_BULGE8
504092010	358.56	−2.15	2009-09-16 07:21:35	50.9	-	-	on	GALACTIC_BULGE9
504093010	358.50	−2.80	2009-09-17 13:54:31	53.2	-	-	on	GALACTIC_BULGE10
504094010	358.50	−3.80	2009-09-19 03:40:31	93.1	-	-	on	GALACTIC_BULGE11
504095010	358.50	−5.00	2009-10-15 15:32:28	48.3	-	-	on	GALACTIC_BULGE12
504099010	25.50	0.01	2009-04-06 02:57:46	52.7	-	-	on	G25.5+0.0
505025010	22.00	0.00	2010-04-16 14:27:26	50.5	-	-	on	G22.0+0.0
505026010	23.49	0.04	2010-10-20 13:34:39	49.0	-	-	on	G23.5+0.1
505027010	37.00	−0.09	2010-04-17 17:35:13	51.0	-	-	on	G37.0−0.1
505029010	319.62	0.29	2010-08-05 03:45:12	51.4	-	-	on	FVW319.8+0.3
505030010	319.32	0.29	2010-08-05 22:21:12	51.6	-	-	on	FVW319.8+0.3_BGD
505049010	339.01	−0.93	2010-09-10 18:33:35	51.9	-	-	on	WESTERLUND1_1
505050010	339.79	−1.14	2010-09-12 04:52:53	52.7	-	-	on	WESTERLUND1_2
505051010	339.43	−0.80	2010-09-23 06:09:00	50.2	-	-	on	WESTERLUND1_3
505052010	340.77	−1.01	2010-09-24 09:32:21	49.6	-	-	on	WESTERLUND1_4
505074010	304.58	0.13	2010-09-03 21:54:15	99.6	-	-	on	SNR G304.6+0.1
505076010	347.85	−0.23	2011-02-16 01:17:29	32.6	-	-	on	AX J1714.1−3912
505079010	359.96	−2.79	2011-03-12 06:36:20	50.2	-	-	on	GALACTIC_BULGE4
505080010	359.95	−3.80	2010-04-07 17:15:10	56.1	-	-	on	GALACTIC_BULGE5
505082010	356.41	−0.39	2011-03-15 13:54:28	54.8	-	-	on	GALACTIC_BULGE13
505083010	356.39	−0.81	2010-10-10 14:04:38	56.9	-	-	on	GALACTIC_BULGE14
505084010	356.41	−1.49	2011-03-06 05:36:44	50.3	-	-	on	GALACTIC_BULGE15
505085010	356.39	−2.31	2010-10-13 06:04:47	55.0	-	-	on	GALACTIC_BULGE16
505086010	356.39	−3.51	2010-10-14 13:31:50	53.1	-	-	on	GALACTIC_BULGE17
505088010	26.31	−0.00	2011-03-25 07:00:01	49.7	-	-	on	HESS_J1741-055_1
505089010	26.40	−0.31	2011-03-26 10:41:12	50.0	-	-	on	HESS_J1741-055_2
505090010	26.71	−0.15	2011-03-27 15:21:16	49.6	-	-	on	HESS_J1741-055_3
505091010	27.13	−0.28	2011-03-28 19:01:23	51.3	-	-	on	HESS_J1741-055_4
506019010	36.00	0.05	2011-09-18 22:04:29	40.9	-	-	on	HESSJ1857−A
506021010	23.30	0.31	2011-04-08 06:06:16	40.3	-	-	on	HESSJ1832
506051010	18.78	0.40	2012-03-08 22:01:58	52.0	-	-	on	G18.8+0.3
507027010	318.36	−0.44	2012-09-15 02:32:40	31.0	-	-	on	HESS J1457−593
507044010	19.57	0.01	2012-10-15 13:05:48	171.8	-	-	on	NONE
507068010	337.21	−0.73	2012-09-02 13:16:23	304.2	-	-	on	G337.2−0.7
507069010	2.00	−0.04	2013-03-15 09:48:19	110.3	-	-	on	GRXE_E_2

[a] Effective exposure time of the cleaned data.

[b] Availability of the XIS 2 sensor.

[c] The sensor which is not used for analysis because its observation is performed in the window mode.

[d] The SCI technique was operated (on) or not (off) in the observation.

Table 4.1. Observation log.

Obs. ID	Pointing direction		Obs. start	Exp.[a]	XIS 2[b]	Win.[c]	CI[d]	Target name
	l (°)	b (°)	(UT)	(ks)				
507070010	2.25	−0.04	2013-03-17 18:39:56	111.8	-	-	on	GRXE_E_3
507071010	2.50	−0.04	2013-03-20 02:41:04	112.3	-	-	on	GRXE_E_4
507072010	2.75	−0.04	2013-03-22 07:20:36	110.7	-	-	on	GRXE_E_5
507073010	3.00	−0.04	2013-03-24 08:46:03	108.9	-	-	on	GRXE_E_6
507074010	3.15	0.16	2013-04-03 21:33:46	104.1	-	-	on	GRXE_E_9
507075010	3.25	0.41	2013-03-11 09:06:19	109.6	-	-	on	GRXE_E_10
508021010	35.57	−0.59	2013-10-27 20:00:53	51.7	-	-	on	HESSJ1858−A
508022010	35.61	−0.40	2013-10-28 23:25:55	52.6	-	-	on	HESSJ1858−B
508075010	1.75	−0.04	2014-03-10 01:33:32	109.3	-	-	on	GRXE_E_1
508076010	3.25	−0.04	2014-02-28 12:46:16	109.8	-	-	on	GRXE_E_7
508077010	3.50	−0.04	2014-03-02 17:00:51	109.4	-	-	on	GRXE_E_8
509038010	39.19	−0.30	2014-04-26 06:42:08	82.8	-	-	on	3C 396

[a] Effective exposure time of the cleaned data.
[b] Availability of the XIS 2 sensor.
[c] The sensor which is not used for analysis because its observation is performed in the window mode.
[d] The SCI technique was operated (on) or not (off) in the observation.

Chapter 5

Result I: Global structure of the GDXE –the 6.4 keV and 6.7 keV lines and the continuum emission

5.1 Analytical procedure

We make an X-ray image in the energy band of 2–8 keV for each FOV. We exclude point-like sources with flux higher than 1×10^{-13} erg s^{-1} cm^{-2} and bright diffuse sources from the observation data. The FOV images and excluded regions are summarized in Appendix. In some FOVs, a fan-like shaped emission is clearly seen. Since the structures are different among XIS 0, 1, 2 (if it is valid), and 3, this emission must be artificial and caused by stray light from a bright X-ray point source outside the FOV. Such regions require special care. Most of the stray light sources which affect our used data are low mass X-ray binaries: GX 3+1, GX 5−1, GX 340+0, and Cir X−1. Low mass X-ray binaries generally have continua (e.g. blackbody, disk blackbody, or power law) often accompanied by a broad emission line; do not have narrow emission lines. This means that the stray light does not affect the observed intensities of the 6.4 keV, 6.7 keV and 7.0 keV lines while it affects the continuum flux.

Next, we extract a spectrum from each pointing. The spectra in the 4–10 keV band are fitted with a phenomenological model which consists of four Gaussian lines and an absorbed bremsstrahlung as well as the CXB model (Kushino *et al.*, 2002). The line energies of the Gaussians are fixed to 6.40 keV (neutral iron Kα), 6.68 keV (helium-like iron Kα), 6.97 keV (hydrogen-like iron Lyα), and 7.06 keV (neutral iron Kβ) (Smith *et al.*, 2001; Kaastra and Mewe, 1993). The intensity of the neutral iron Kβ line is fixed to 0.125 times that of the neutral iron Kα line (Kaastra and Mewe, 1993), while those of the other lines are free parameters. The interstellar absorption column densities are fixed to 6×10^{22} cm^{-2} for the GCXE region ($|l| < 5^\circ$ and $|b| < 0.^\circ 5$), 1×10^{22} cm^{-2} for the GBXE region ($|b| > 1^\circ$), and 3×10^{22} cm^{-2} for the GRXE region ($|l| > 5^\circ$ and $|b| < 1^\circ$) (e.g. Uchiyama *et al.*, 2013; Ebisawa *et al.*, 2001). The normalization and temperature of the bremsstrahlung component are allowed to vary. We then obtain the intensities of the 6.4 keV, 6.7 keV, and 7.0 keV lines and the continuum in the 5–8 keV band. Here we exclude the contribution of the CXB. We show an example of the spectral fitting in figure 5.1.

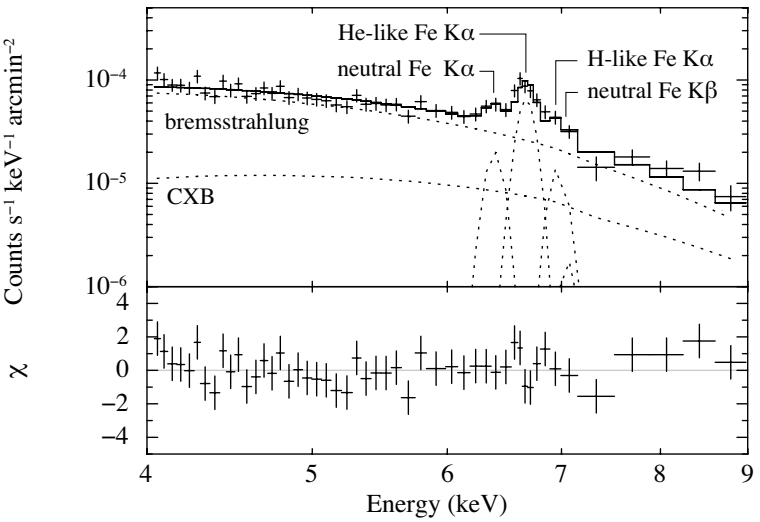

Figure 5.1. Example of the spectrum (ObsID=503020010) fitted by the phenomenological model consisting of an absorbed bremsstrahlung and Gaussians as well as the CXB.

5.2 Latitudinal distribution of the iron lines and continuum of the GDXE

Using the observed intensities of the 6.4 keV, 6.7 keV, and 7.0 keV lines and the continuum of the GDXE, we investigate the spatial distribution of them. The intensity of each component decreases with the Galactic latitude approximately in an exponential manner with an e-folding scale height, which is one of the most important keys to resolving its origin. Figure 5.2 and 5.3 shows latitudinal distributions of the 6.4 keV, 6.7 keV, and 7.0 keV lines, and the 5–8 keV flux in the regions of (a) $|l| < 0.^\circ 5$, (b) $l = 358.^\circ 5$, (c) $l = 356.^\circ 0$–$356.^\circ 4$, (d) $10^\circ < l < 30^\circ$, and (e) $330^\circ < l < 350^\circ$.

Each distribution of the upper panels in figure 5.2 and figure 5.3 cannot be represented by a single exponential function. Thus, the data plots in and near the GC region, especially for the $|l| < 0.^\circ 5$ region, require two exponential functions. We simultaneously fit the data of (a), (b) and (c) with the model described by

$$A_{\rm GCXE} \times \exp(-|b_*|/b_{\rm GCXE}) + A_{\rm GBXE} \times \exp(-|b_*|/b_{\rm GBXE}). \tag{5.1}$$

The normalizations, $A_{\rm GCXE}$ and $A_{\rm GBXE}$, would vary depending on the Galactic longitude. We scaled the $A_{\rm GCXE}$ assuming the e-folding scale length of $0.^\circ 63$ (Uchiyama *et al.*, 2013). The normalization of $A_{\rm GBXE}$ are free parameters among the three regions. The e-folding scales of $b_{\rm GCXE}$ and $b_{\rm GBXE}$ in (b) and (c) are linked to those in (a).

The data of (d) and (e) are fitted with an exponential model described by

$$A_{\rm GRXE} \times \exp(-|b_*|/b_{\rm GRXE}) + A_2 \times \exp(-|b_*|/b_{\rm GRXE}). \tag{5.2}$$

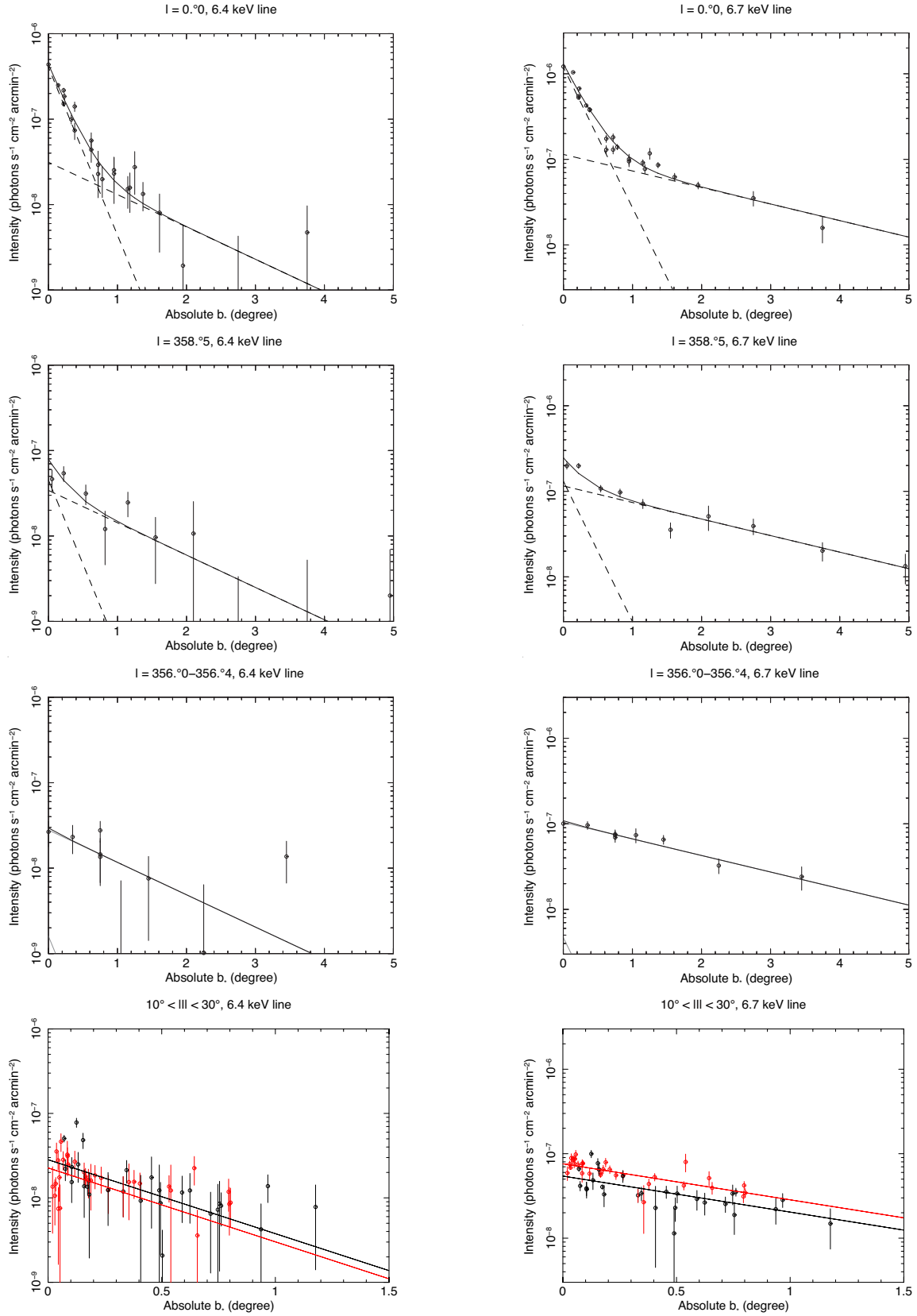

Figure 5.2. Latitudinal distributions of the 6.4 keV line and the 6.7 keV line flux in the regions of $|l| < 0.^\circ5$, $l = 358.^\circ5$, $l = 356.^\circ0$–$356.^\circ4$ and $10^\circ < |l| < 30^\circ$. The solid lines show the best-fit model. The red and black data and lines in the bottom panel show the data and best-fit result in the east ($10^\circ < l < 30^\circ$) and the west ($330^\circ < l < 350^\circ$), respectively.

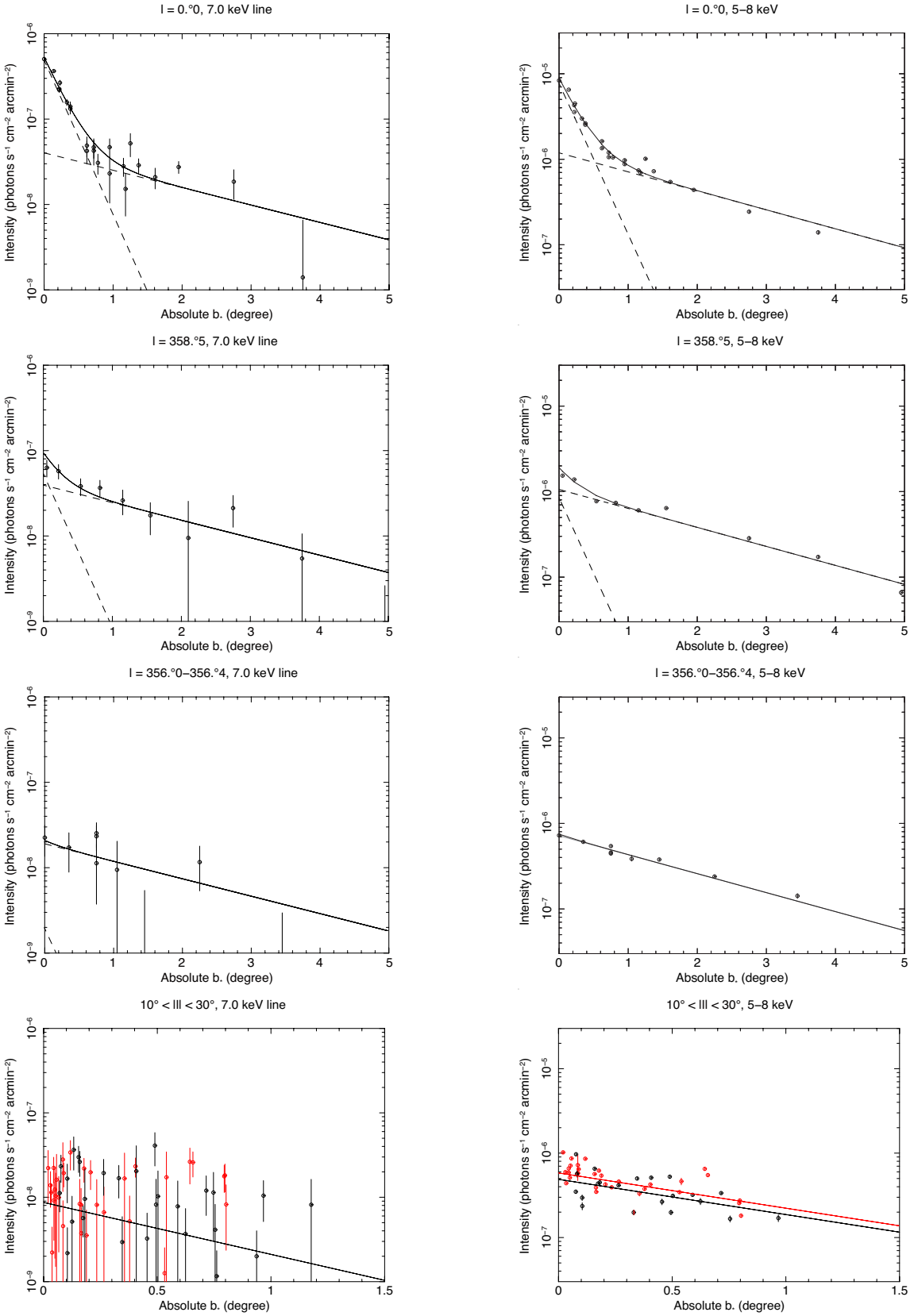

Figure 5.3. Same as figure 5.2, but those of the 7.0 keV line and the continuum in the 5–8 keV band.

Since the longitudinal distribution of the GDXE on the plane is asymmetric with respect to the GC especially for $|l| > 10°$ (e.g. Revnivtsev *et al.*, 2006a), the normalization $A_{\rm GRXE}$ are varied between the east and west longitude regions. The scale heights of $b_{\rm GRXE}$ in both the regions are linked to each other. We exclude the regions contaminated by stray light in fitting the distributions of the continuum. The best-fit parameters are summarized in table 5.1.

If we assume the distance to the emission region to be 8 kpc, the scale heights of the 6.7 keV line of the GCXE, GBXE, and GRXE are 36 ± 3 pc, 314 ± 95 pc, and 142 ± 17 pc, respectively, and those of the 7.0 keV and the continuum coincide within the error with them. On the other hand, the scale heights of the 6.4 keV line in the GCXE, GBXE, and GRXE are 31 ± 3 pc, 161 ± 50 pc, and 70 ± 17 pc, respectively, which are systematically smaller than those of the 6.7 keV line.

Table 5.1. Scale height of the GDXE*.

Region	Component	GCXE		GBXE		GRXE	
		$A_{\rm GCXE}$ †	$b_{\rm GCXE}$ (degree)	$I_{\rm GBXE}$ †	$b_{\rm GBXE}$ (degree)	$A_{\rm GRXE}$ †	$b_{\rm GRXE}$ (degree)
(a) $l = 0°$	6.4 keV	4.1±0.2	0.22±0.02	0.31±0.15	1.15±0.36	-	-
	6.7 keV	11.9±0.6	0.26±0.02	1.14±0.34	2.25±0.68	-	-
	7.0 keV	4.9±0.2	0.24±0.02	0.40±0.12	2.13±0.66	-	-
	5–8 keV	77.0±3.6	0.25±0.02	11.9±1.8	1.96±0.25	-	-
(b) $l = 358.°5$	6.4 keV	0.45‡	0.22§	0.35±0.10	1.15§	-	-
	6.7 keV	1.31‡	0.26§	1.15±0.27	2.25§	-	-
	7.0 keV	0.54‡	0.24§	0.39±0.10	2.13§	-	-
	5–8 keV	8.47‡	0.25§	10.6±1.4	1.96§	-	-
(c) $l = 356.°2$	6.4 keV	0.02‡	0.22§	0.28±0.07	1.15§	-	-
	6.7 keV	0.05‡	0.26§	1.04±0.21	2.25§	-	-
	7.0 keV	0.02‡	0.24§	0.19±0.06	2.13§	-	-
	5–8 keV	0.31‡	0.25§	7.2±0.9	1.96§	-	-
(d) $l = 10°$–$30°$	6.4 keV	-	-	-	-	0.23±0.03	0.50±0.12
	6.7 keV	-	-	-	-	0.76±0.02	1.02±0.12
	7.0 keV	-	-	-	-	0.09±0.02	0.71±0.29
	5–8 keV	-	-	-	-	5.8±0.4	1.04±0.20
(e) $l = 330°$–$350°$	6.4 keV	-	-	-	-	0.28±0.04	0.5¶
	6.7 keV	-	-	-	-	0.54±0.03	1.0¶
	7.0 keV	-	-	-	-	0.09‖	0.71¶
	5–8 keV	-	-	-	-	4.9±0.5	1.0¶

* The error ranges in this table are calculated at 68% confidence levels.
† The units are 10^{-7} photons s^{-1} cm^{-2} arcmin^{-2}.
‡ These normalizations are fixed to $I_{\rm GCXE(l=0°)} \times 0.11$ at $l = 358.°5$ and $I_{\rm GCXE(l=0°)} \times 0.004$ at $l = 356.°2$ based on the scale length of the GCXE obtained by Uchiyama *et al.* (2013).
§ These scale heights are linked to those of $l = 0°$.
‖ The normalization is linked to that of $l = 10°$–$30°$.
¶ These scale heights are linked to those of $l = 10°$–$30°$.

5.3 Equivalent widths of the iron K-shell lines

We investigate a typical value of the equivalent width of the GCXE ($|l| < 1.^\circ 5$ and $|b| \leq 0.^\circ 5$), GBXE ($|l| < 4.^\circ 0$ and $|b| \geq 1.^\circ 0$), and GRXE ($10^\circ < |l| < 30^\circ$ and $|b| < 1.^\circ 0$). The mean equivalent widths of the 6.4 keV line in the GCXE, GBXE and GRXE are calculated to be 145 ± 3 eV, 61 ± 11 eV, and 97 ± 12 eV, respectively, while those of the 6.7 keV lines are 527 ± 4 eV, 443 ± 14 eV, 428 ± 15 eV, and those of the 7.0 keV lines are 221 ± 3 eV, 160 ± 14 eV, and 117 ± 19 eV, respectively. Figure 5.4 shows the equivalent width diagrams of the 6.4 keV and 6.7 keV lines in the GCXE, GBXE, and GRXE.

5.4 Intensity profile along the Galactic longitude

In order to investigate the longitudinal distributions of the 6.4 keV line along the Galactic plane, especially in the GRXE region (outside the range in figure 1.10), we make the intensity profile of the 6.4 keV line, and for a comparison, those of the 6.7 keV and 7.0 keV lines and the continuum in the 5–8 keV band in the $|l| > 1.^\circ 5$ region as shown in figure 5.5. The data points are extracted from the $|b| < 0.^\circ 5$ and are not corrected for the b-dependence. The continuum emissions in $1.^\circ 5 < l < 3.^\circ 5$, $l \sim -20^\circ$, and $l \sim -38^\circ$ are contaminated by stray light from GX 3+1, GX 340+0, and Cir X−1, respectively. In particular, the $1.^\circ 5 < l < 3.^\circ 5$ and $l \sim -38^\circ$ regions are severely contaminated by bright second-reflection components. We excluded the regions contaminated by the second reflection from the $1.^\circ 5 < l < 3.^\circ 5$ and the $l \sim -38^\circ$ regions; the data points in the two regions are still contaminated by backside reflection. In the $l \sim -20^\circ$ region, we leave the stray-light component in the data points because the stray light in the region is not so bright.

We discover enhancements of the 6.4 keV line intensity distribution compared with the 6.7 keV line. The flux ratio of the 6.4 keV and 6.7 keV lines in figure 5.5e clearly shows local excesses in the $1.^\circ 5 < l < 3.^\circ 5$ and $-20^\circ < l < -30^\circ$ regions. These enhancements should have a different origin from that of the 6.7 keV and and the continuum. In the following chapter, we will discuss the origin of these enhancements.

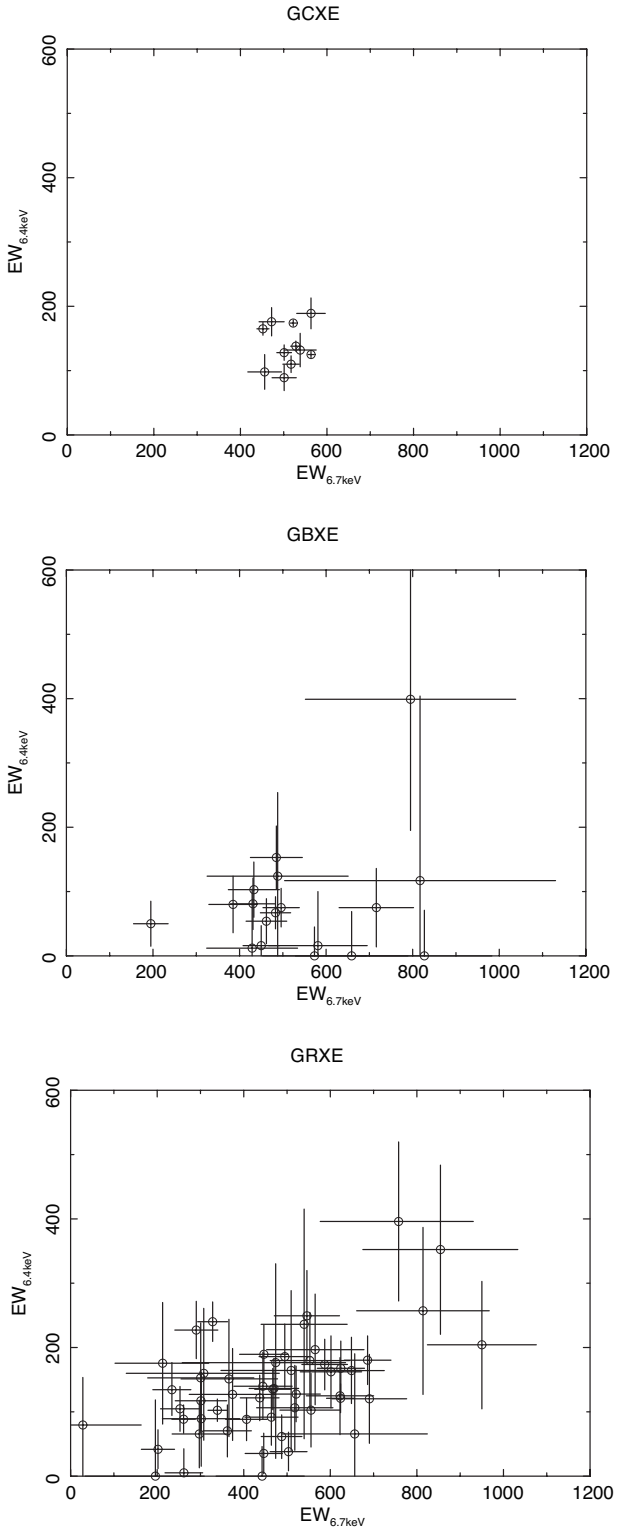

Figure 5.4. Equivalent width diagrams of the 6.4 keV and 6.7 keV lines in the GCXE (top), the GBXE (middle), and the GRXE (bottom).

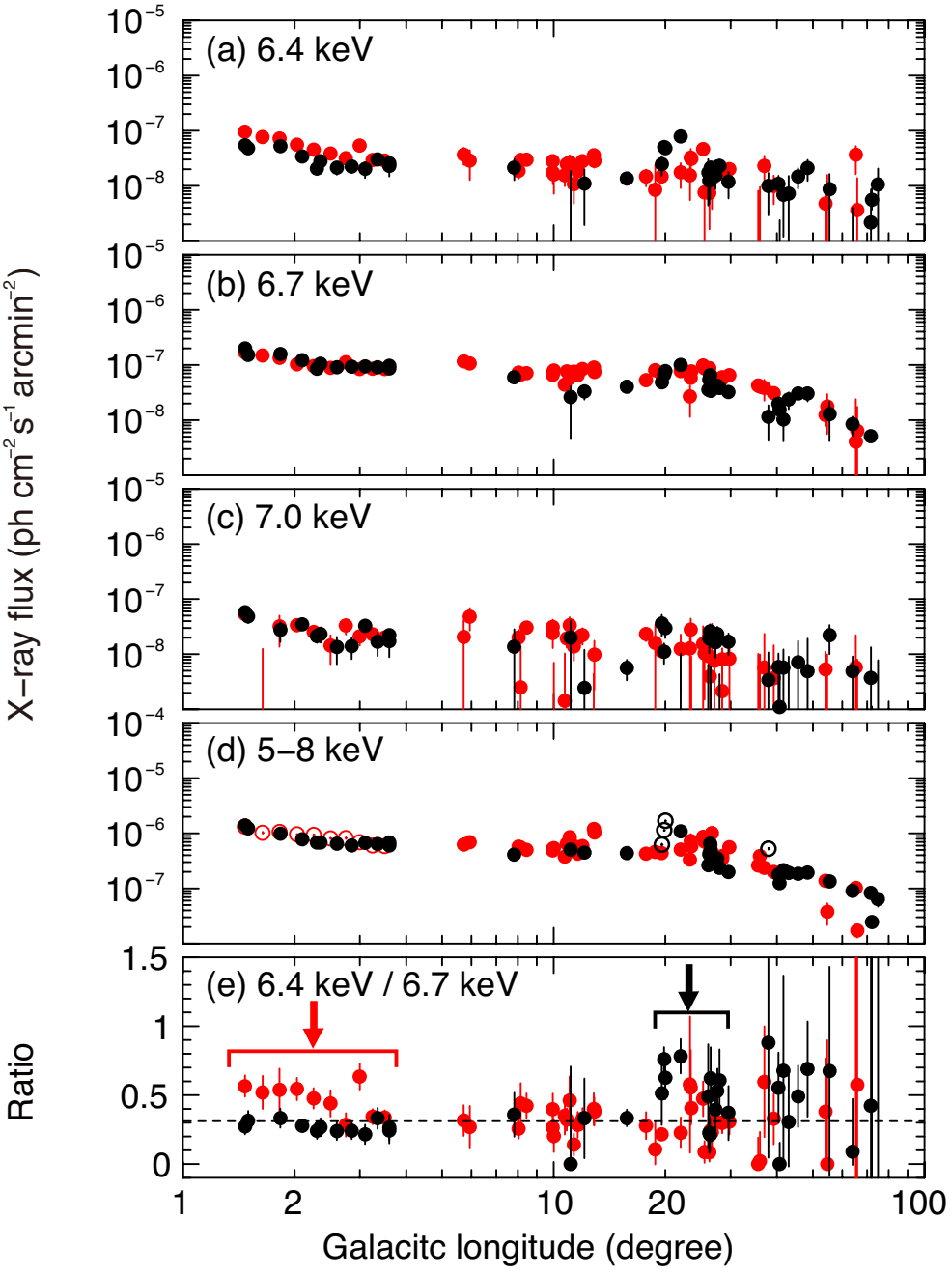

Figure 5.5. Intensity profiles of X-rays along the Galactic plane. The red and black circles indicate the data in the east and west regions, respectively. (a) The 6.4 keV line. (b) The 6.7 keV line. (c) The 7.0 keV line. (d) The continuum in the 5–8 keV band. The open circles are the data contaminated by stray light (see text). (e) Intensity ratio of the 6.4 keV and 6.7 keV lines. The dashed line shows the averaged value on the Galactic plane ($|l| > 1.°5$). The two regions indicated by the arrows, namely the $1.°5 < l < 3.°5$ and the $-20° < l < -30°$ regions, show excesses in the ratio.

Chapter 6

Results II: Discovery of local enhancements in the 6.4 keV line

Figure 5.5 shows local enhancements in the two regions in the longitudinal distribution of the 6.4 keV line; (a) $1.^\circ5 < l < 3.^\circ5$ and (b) $-20^\circ < l < -30^\circ$ regions. In this chapter, we perform a more detailed analysis of the two regions. We analyze all the data in the $1.^\circ5 < l < 3.^\circ5$ region for the region (a), and call them the GC east region. For analysis of the region (b), we use the data of the three FOVs (ObsID=406078010, 401052010, and 404056010) which have the strongest intensity of the 6.4 keV line, in order to increase the signal-to-noise ratio, and call them the $l = -20^\circ$ region. We caution that most of the FOVs in the (a) and (b) regions, unfortunately, are affected by stray light. It is important to estimate the stray light in extracting and analysing the spectra of the enhancements. First we describe the estimation of the stray light, and then we investigate the spectral features of the enhancements.

6.1 Estimation of stray light

6.1.1 Stray light in the GC east region

A bright low mass X-ray binary, GX 3+1, is located at $(l, b) = (2.^\circ294, 0.^\circ794)$, which is $\sim 50'$–$90'$ apart from each pointing in the GC east region. Some regions of the FOVs are contaminated by the stray light from GX 3+1. Stray light pattern in the FOVs are shown in figure 6.1 with the position of GX 3+1 and the ObsIDs. Most of the pointings are contaminated by stray light of secondary and backside reflection. Since two FOVs (ObsID = 508077010 and 508076010) are $89'$ and $77'$ apart from GX 3+1, respectively, these observations are free from secondary-only stray (Suzaku Technical Description); the region in the FOVs near side to the stray light source is free from stray light. Some FOVs (ObsID = 508075010, 502009010, 507075010, and 507074010) are located at quadrant boundary, and thus a part of the FOVs are stray-light free region.

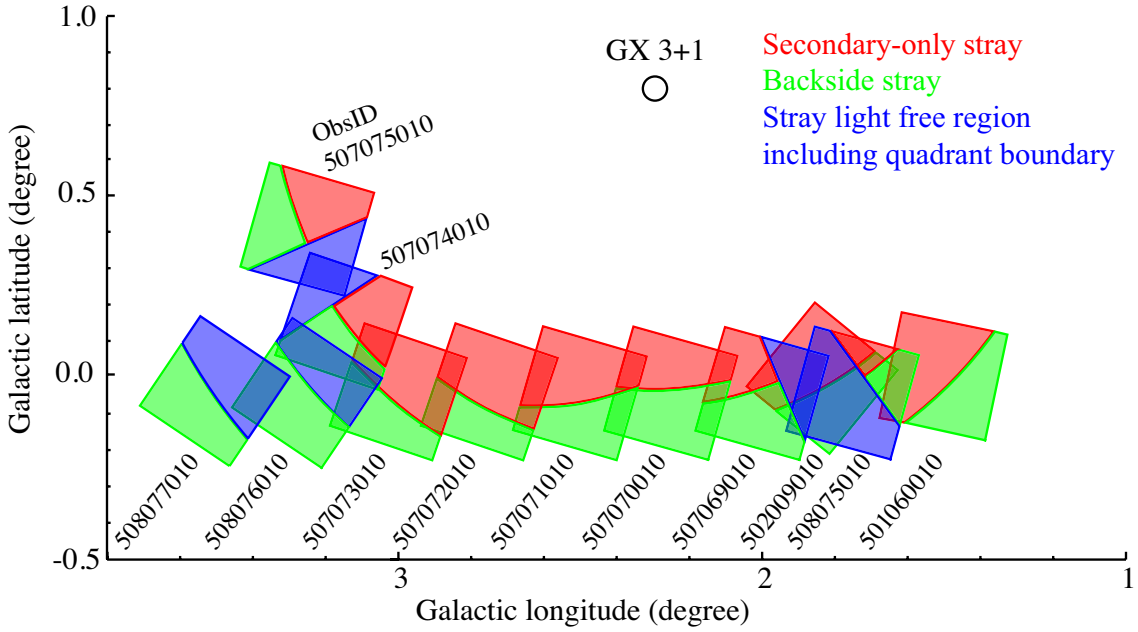

Figure 6.1. Stray light pattern for each FOV in the observation of the GC east region. Red and green regions show those contaminated by the stray light of secondary reflection and backside reflection, respectively. Blue regions show the stray-light free region including the quadrant boundary region. The position of the stray light source GX 3+1 is represented by a circle. The observed images are shown in Appendix.

Since the low mass X-ray binary GX 3+1 does not emit narrow lines (Piraino *et al.*, 2012), the stray light does not affect the line intensity of the GDXE, but affects the continuum. We exclude the region contaminated by secondary reflection because the flux of the secondary-reflection component is far beyond the intensities of the GDXE. On the other hand, the flux of the backside-reflection component is about 10% of that of the GDXE. In order to estimate the backside stray, we integrate X-ray spectra from the region contaminated by the backside reflection and the stray-light free region, and subtract the latter from the former. Here, we performed the correction for the Galactic coordinate dependence of the GDXE emission on the basis of chapter 5. Figure 6.2 shows the stray light spectrum. For comparison, we simulate the stray light spectrum by `xissim` using the X-ray spectral model of GX 3+1 adapted in Piraino *et al.* (2012), which consists of a blackbody with temperature of 1.7 keV and a multicolor disk blackbody with temperature of 0.93 keV and has the flux of $\sim 4.5 \times 10^{-9}$ erg s^{-1} cm^2 in the 2–10 keV band. The simulated spectrum is presented by the red curve in figure 6.2. The observed spectrum is well fitted with the simulated spectrum with the null hypothesis probability of 3% (figure 6.2). The absolute observed flux is required to be multiplied by 1.3 and obtained to be $(5.8^{+1.2}_{-1.1}) \times 10^{-9}$ erg s^{-1} cm^2. This would be due to calibration uncertainty as described in section 3.2.3. Thus we will adopt the obtained flux by the subtraction.

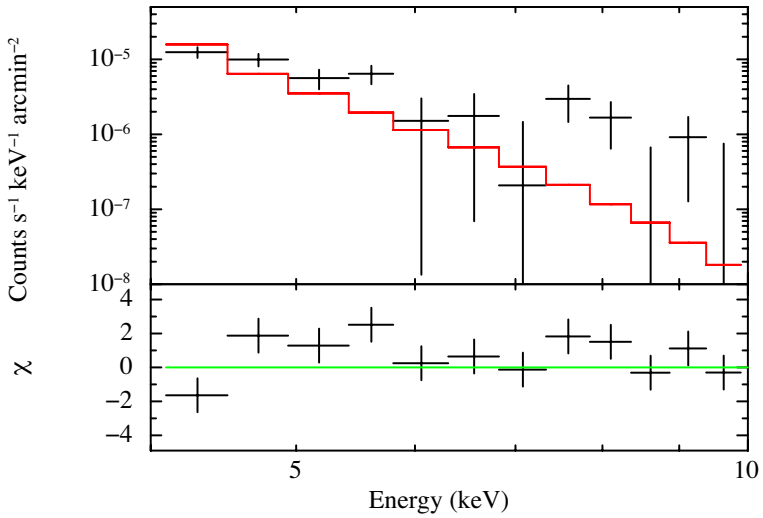

Figure 6.2. Stray-light spectrum of GX 3+1. The data were obtained by subtracting the stray-light free spectrum from the spectrum contaminated by backside reflection. The red curve shows the simulated spectrum of stray light from GX 3+1 that was estimated by `xissim` with the model and parameters reported by Piraino *et al.* (2012) (see text). The bottom panel shows the difference between the observed and simulated spectra.

6.1.2 Stray light in the $l = -20°$ region

A bright X-ray binary, GX 340+0, which is also a low mass X-ray binary, is 30′–60′ apart from two FOVs in the $-20°$ region, and they are contaminated by stray light from the binary. In the off-set angle of 30′–60′, the secondary reflection is considerably low (see figure 3.7). Therefore we use the entire FOV, of course excluding point sources. Church *et al.* (2006) reported that the X-ray spectrum of GX 340+0 is represented by a cut-off power law and multiclolor disk blackbody as well as a broad iron line. In order to estimate the stray light spectrum in a similar way as in the case of the GC east region, we use quadrant boundary region in a FOV (ObsID=406078010). A nearby FOV (ObsID=405027010) is also contaminated by stray light from GX 340, but in the same time the FOV has a quadrant boundary, and thus we used also the region to increase statistics. We perform simulation by `xissim` to determine the position of the quadrant boundary regions. The results are shown in figure 6.3.

We integrate spectra extracted from the quadrant boundary regions (the blue regions in figure 5.3) in ObsID=406078010 and 405027010. We then extract the spectrum from the region contaminated by stray light (the green region in figure 5.3) in ObsID=406078010, and subtract the former from the latter. The stray light spectrum is shown in the left-side panel in figure 6.4. In a similar way, the stray light spectrum of ObsID=401052010 is also obtained as is shown in the right-side panel. The red curves in both the panel are simulated spectra by using `xissim`, assuming the spectral model of GX 340+0, which consists of a multicolor disk blackbody with temperature of 2.44 keV, a cut-off power law with photon index of 1.7 and cut-off energy of 5.8 keV and a broad line at 6.9 keV with the line width of 0.5 keV, and has the flux of $\sim 9.0 \times 10^{-9}$ erg s^{-1} cm^{-2} in the 2–10 keV band based on Church *et al.* (2006). The observed spectra are well fitted with the simulated spectrum with the null hypothesis probability of 0.2% and 30% for ObsID=406078010 and 401052010, respectively. The absolute observed fluxes are required to to be multiplied by 2.1 for both the FOVs and obtained

to be $(1.9 \pm 0.1) \times 10^{-8}$ erg s^{-1} cm^{-2}. We will adopt the obtained flux by the subtraction as the flux of the stray light.

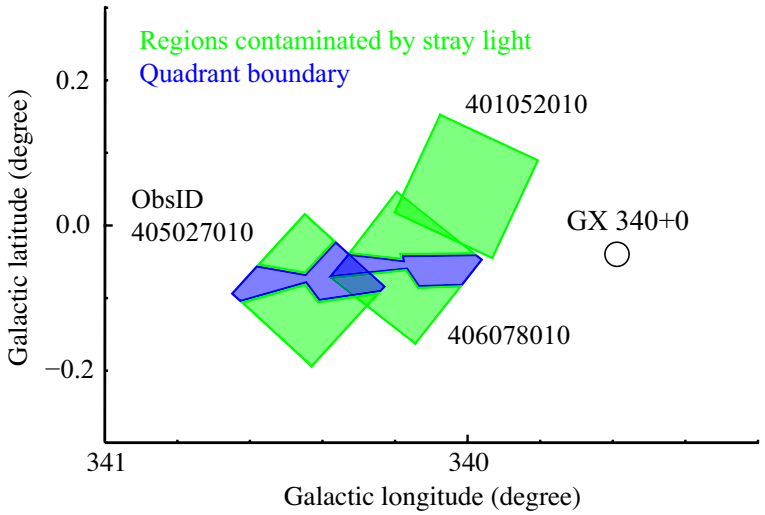

Figure 6.3. Stray light pattern for each FOV in the observation of the $l = -20°$ region estimated with `xissim`. Green and blue regions show the region contaminated by the stray light and the quadrant boundary region, respectively. The position of the stray light source GX 340+0 is represented by a circle. See Appendix for the observed images.

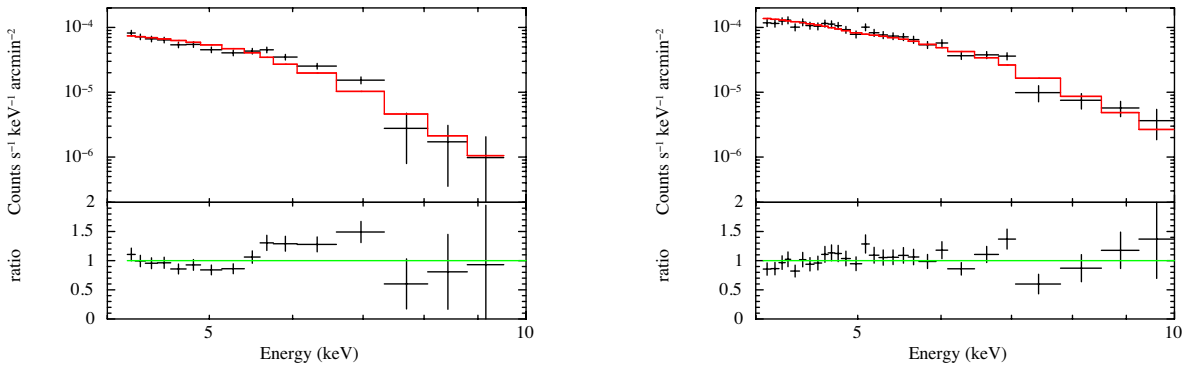

Figure 6.4. Stray-light spectrum of GX 340+0. (left) Spectra differential between the observed spectra extracted from the region contaminated by stray light in the observation of ObsID=406078010 and the quadrant boundary regions in the two observations (ObsID=405027010 and 406078010). The red curve shows the simulated spectrum of stray light from GX 340+0 that was estimated by `xissim` with the model and parameters reported by Church *et al.* (2006) (see text). The bottom panel shows the difference between the observed and simulated spectra. (right) Same as the left panel, but in the case of the stray light in the observation of ObsID=401052010.

6.2 Excess in the GC east

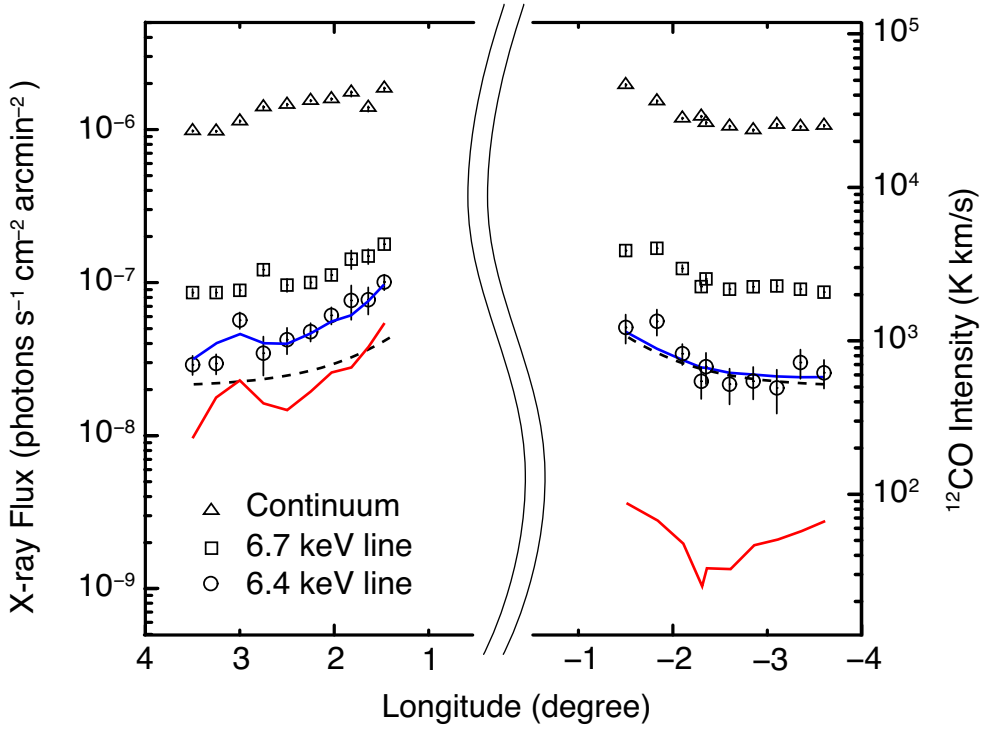

Figure 6.5. Intensity profiles of X-rays and ^{12}CO molecular clouds in $-4.^\circ5 < l < 4.^\circ5$. The triangles, squares, and circles show the fluxes of the continuum in the 4–10 keV band (where the 6–7 keV band was excluded), the 6.7 keV line, and the 6.4 keV line, respectively. Errors are quoted at 68% confidence levels. The dashed lines show a model of stellar distribution, which is symmetric with respect to Sgr A* (Nishiyama *et al.*, 2013; Launhardt *et al.*, 2002; Revnivtsev *et al.*, 2006a). The red lines are the ^{12}CO intensity profile (the unit is the right-side axis). The blue lines are the sum of the symmetric distribution model and the ^{12}CO intensity multiplied by α, where α is a factor to convert the ^{12}CO intensity to the 6.4 keV flux (see text). The figure is taken from Nobukawa *et al.* (2015a, figure 1).

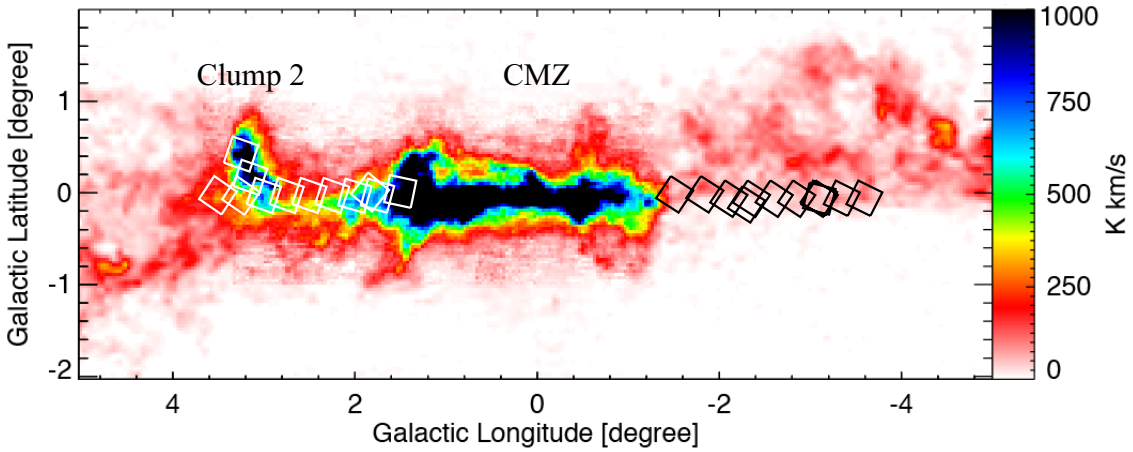

Figure 6.6. Integrated intensity map of ^{12}CO in $-4.^\circ5 < l < 4.^\circ5$. Integrated range is -300 km s^{-1} to $+300$ km s^{-1} (Torii *et al.*, 2010), where the local components are excluded (see text). White and black squares show the FOVs of the XIS.

We show a longitudinal profile of the intensity of the 6.4 keV and 6.7 keV lines and the continuum in the 4–10 keV band (where the 6–7 keV band was excluded) in the GC east region in figure 6.5. A popular scenario for the origin of the GDXE is a collection of faint stars (Revnivtsev *et al.*, 2009, 2006a; Yuasa *et al.*, 2012; Warwick *et al.*, 2014). The stellar mass distribution has been constructed from infrared observations, and has an east-west symmetry (Nishiyama *et al.*, 2013; Launhardt *et al.*, 2002; Revnivtsev *et al.*, 2006a). The profile is given by the dashed lines in figure 6.5. All the X-ray flux distributions, except that of the 6.4 keV line in the east, are consistent with the stellar distribution curve. A remarkable structure is an excess of the 6.4 keV line flux in the east compared to the west, and hence the excess should have a different origin from the symmetrical components which would be due to point sources.

We plot in figure 6.5 the ^{12}CO line intensity taken by NANTEN integrated over the velocity range from -300 km s^{-1} to $+300$ km s^{-1} (Torii *et al.*, 2010). Here, the local components uniformly distributed around -20 km s^{-1} to $+30$ km s^{-1} and the Near 3 kpc arm having a velocity gradient from -80 km s^{-1} at $l = -5^\circ$ to -30 km s^{-1} at $l = 5^\circ$ (Dame and Thaddeus, 2008) are excluded. The ^{12}CO profile is similar to the excess distribution of the 6.4 keV line in the east, which suggests that its origin is due to molecular gas. The excess at $l = 3^\circ$ coincides with the intersection point of the Galactic plane and the giant molecular cloud, Bania's Clump 2, which extends towards the north (Bania, 1977; Tsuru *et al.*, 2014).

Figure 6.7a shows integrated X-ray spectra from the east and west sides. The CXB is subtracted from both the spectra according to Kushino *et al.* (2002). The stray light from GX 3+1, which is estimated in section 6.1.1, is also subtracted from the east spectrum. Each spectrum is fitted with an absorbed power law plus four Gaussian lines at 6.4, 6.7, 7.0, and 7.06 keV. The interstellar absorption column density is fixed to 6×10^{22} cm^{-2}. The intensity of 7.06 keV (the neutral iron Kβ) line is fixed to 0.125 times that of 6.4 keV (the neutral iron Kα) line. The best-fit parameters are summarized in table 6.1.

We subtract the west spectrum from the east one to make the X-ray spectrum of the east excess as is shown in figure 6.7b. The excess spectrum is fitted with a power law plus a Gaussian line at 6.4 keV. The best-fit line and continuum fluxes are $(2.5 \pm 0.6) \times 10^{-8}$ photons s^{-1} cm^{-2} arcmin^{-2} and $(1.9 \pm 0.3) \times 10^{-8} (E/6.4\,\mathrm{keV})^{-3\pm1}$ photons s^{-1} keV^{-1} cm^{-2} arcmin^{-2}, respectively, as shown in table 6.1. The 6.7 keV line flux has the symmetry between the east and west, but at the same time, there are statistic errors by ±7%. It means that the 6.7 keV line flux has a possible asymmetry between the east and west by ±7%. Thus we take this error into account as the uncertainty of the symmetry. Then the equivalent width is estimated to be $1.3 \pm 0.4^{+4.2}_{-0.2}$ keV, where the second and third terms are the statistical and systematical errors, respectively.

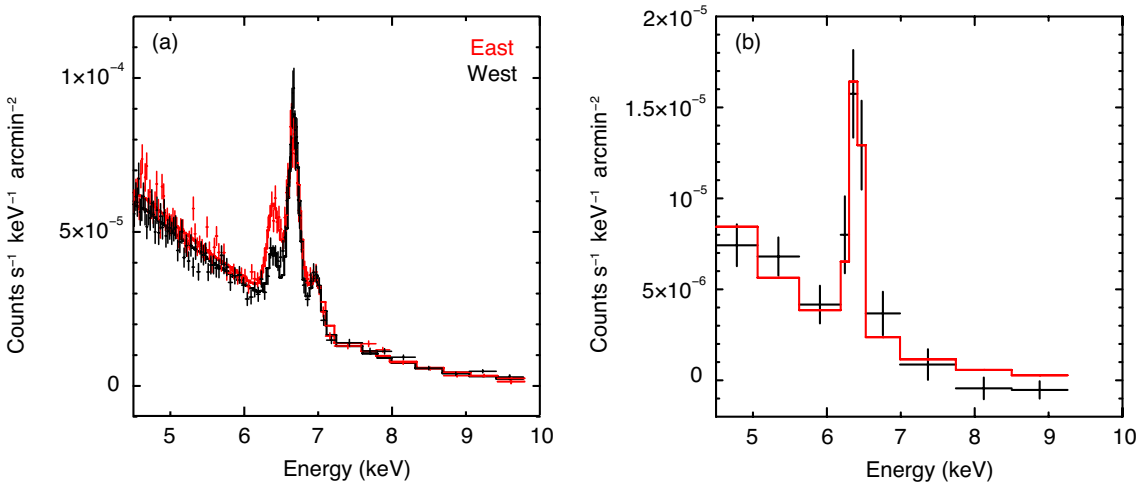

Figure 6.7. (a) X-ray spectra extracted from the east (red) and west (black) sides. The red and black lines show the best-fit model consisting of an absorbed power law plus four Gaussian lines at 6.4 keV, 6.7 keV, 7.0 keV, and 7.06 keV. (b) X-ray spectrum of the excess emission in the east. The red line shows the best-fit model consisting of a power law plus a Gaussian line at 6.4 keV. Errors are quoted at 68% confidence levels for the both panels. The both figures are taken from Nobukawa *et al.* (2015a, figure 2).

Table 6.1. Best-fit parameters of the X-ray spectra from the east and west sides (Nobukawa *et al.*, 2015a, table 2).*

	Emission lines			Continuum	
	6.4 keV	6.7 keV	7.0 keV	photon index	normalization
Unit	$(10^{-8})^{\dagger}$	$(10^{-8})^{\dagger}$	$(10^{-8})^{\dagger}$		$(10^{-8})^{\ddagger}$
east	5.1±0.4	10.3±0.5	2.5±0.4	2.3±0.1	22.9±0.1
west	2.5±0.4	10.3±0.5	2.8±0.4	2.2±0.1	21.7±0.1
excess	2.5±0.6	–	–	3±1	1.9±0.3

* The error ranges in this table are calculated at 90% confidence levels.
† Absorption-corrected line flux in the units of photons s^{-1} cm^{-2} $arcmin^{-2}$.
‡ Normalization at 6.4 keV in the units of photons s^{-1} keV^{-1} cm^{-2} $arcmin^{-2}$.

6.3 Excess in the $l = -20°$ region

As in the GC east region, the excess of the intensity of the 6.4 keV line in the $l = -20°$ region would be due to a different origin from the 6.7 keV and 7.0 keV lines and the continuum. Interestingly, the Near 3 kpc arm tangent is located at $l \sim -20°$ (see figure 1.1), and thus it is expected that there is enhancement in molecular gas distribution. Integrated intensity of ^{12}CO obtained by NANTEN around $l \sim -20°$ is shown in figure 6.8 (Kazufumi Torii, private communication). The FOVs of ObsID = 406078010, 401052010, and 404056010 are represented by squares, and we find enhancements in the molecular gas distribution in the three FOV regions. Actually, the FOV regions of ObsID = 406078010 and 404056010 have the highest integrated intensity of ^{12}CO among all of the Suzaku FOVs in $-40° < l < -5°$ region that we analyzed. This fact suggests that the 6.4 keV excess in the $l = -20°$ region is also due to the molecular gas. We call the enhancement in the molecular gas distribution around the FOVs of ObsID = 406078010 and 40105201 as cloud 1 and that of the FOV of 404056010 as cloud 2. Figure 6.9 gives a velocity channel distribution of ^{12}CO in the $l = -20°$ region. Cloud 1 consists of molecular gas in the velocity ranges from -140 km s^{-1} to -120 km s^{-1} and from -60 km s^{-1} to -20 km s^{-1}. The former component would come from the Near 3 kpc arm while the latter component would belong to molecular clouds located in ~ 4 kpc distance (Kazufumi Torii, private communication). Cloud 2, given its corresponding velocity range, would belong to the Near 3 kpc arm.

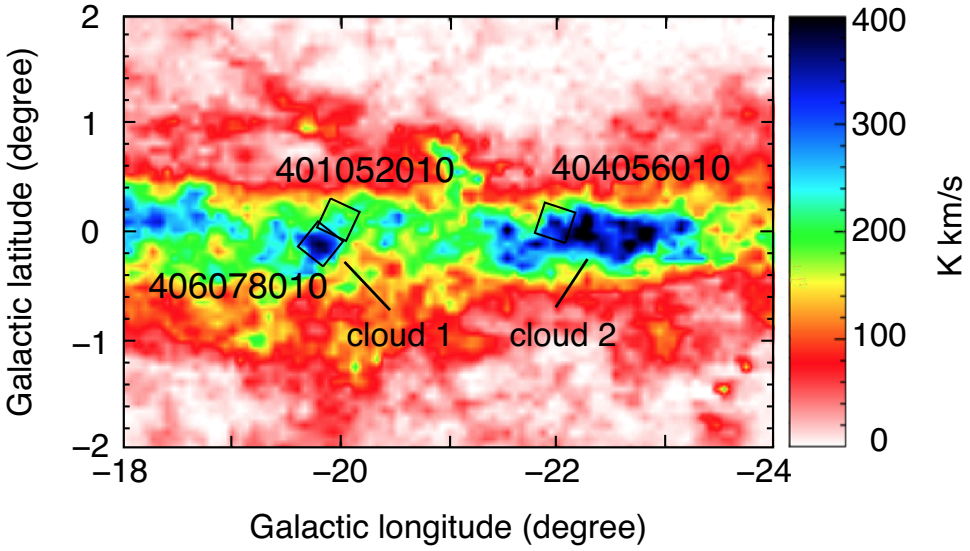

Figure 6.8. Integrated intensity map of ^{12}CO around the $l = -20°$ region. All velocities are integrated. Black squares show the FOVs of the XIS.

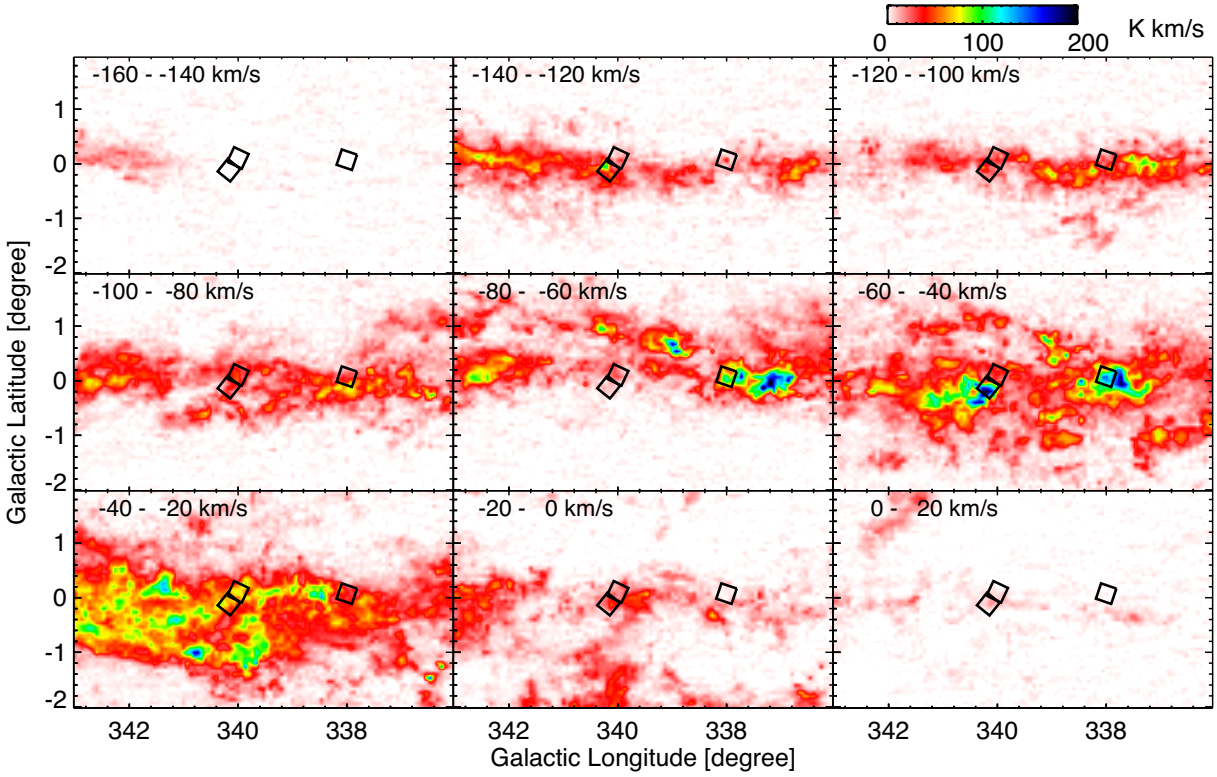

Figure 6.9. Channel map of ^{12}CO around the $l = -20°$ region. Black squares show the FOVs of the XIS.

We extract the spectrum associated with the 6.4 keV excess in the same manner as the case of the GC east. We construct an integrated spectrum from the $-20°$ region and an integrated GRXE spectrum using the data in the $10° < |l| < 30°$ and $|b| < 0.5°$ region. The CXB is subtracted from both the spectra according to Kushino *et al.* (2002). The stray light from GX 340+0, which was estimated in the previous subsection as the model spectrum, is subtracted from the $l = -20°$-region spectrum. The Galactic-coordinate dependence is corrected by adjusting the 6.7 keV line intensity as is shown in figure 6.10a. We, then, extract the spectrum of the excess emission by subtraction of the GRXE spectrum.

The excess spectrum is fitted with a power law plus a Gaussian line at 6.4 keV (figure 6.10b). The best-fit line and continuum fluxes are $(3.9 \pm 1.1) \times 10^{-8}$ photons s^{-1} cm^{-2} arcmin^{-2} and $(5.7 \pm 1.9) \times 10^{-8} (E/6.4 \text{ keV})^{-1.2}$ photons s^{-1} keV^{-1} cm^{-2} arcmin^{-2}, respectively. Here, there is a statistical uncertainty of $\pm 21\%$ in the adjustment of the 6.7 keV line intensity: there are the statistical errors by $\pm 21\%$ in the ratio of 6.7 keV line intensity between the integrated spectrum from the $-20°$ region and the integrated GRXE spectrum. This makes a systematical uncertainty in the subtraction of spectra. Then the equivalent width is estimated to be $0.67 \pm 0.22^{+1.6}_{-0.1}$ keV, where the second and third terms are the statistical and systematical uncertainties, respectively.

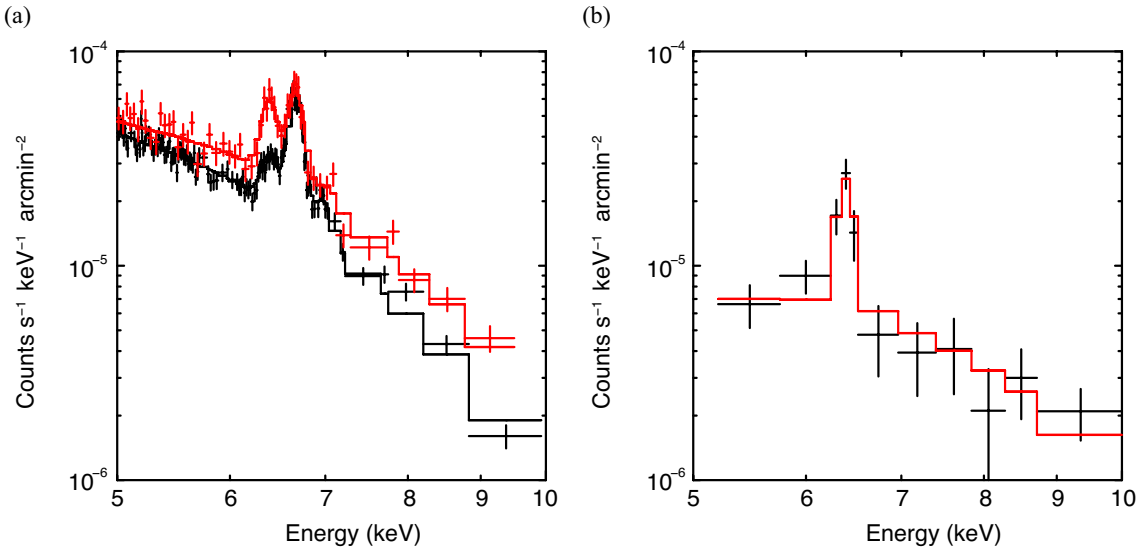

Figure 6.10. (a) X-ray spectrum extracted from $l = 20°$ (red) and the integrated spectrum extracted from the other regions on the Galactic plane ($10° < |l| < 30°$; black). The red and black lines show the best-fit model consisting of an absorbed powerlaw plus four Gaussian lines at 6.4 keV, 6.7 keV, 7.0 keV, and 7.06 keV. (b) X-ray spectrum of the excess emission in the $l = -20°$ region. The red line shows the best-fit model consisting of a power law plus a Gaussian line at 6.4 keV. Errors are quoted at 68% confidence levels for both the panels.

Table 6.2. Best-fit parameters of the X-ray spectra from the $l = -20°$ regions and the other region on the Galactic plane ($10° < |l| < 30°$) before correcting the Galactic-coordinate dependence by adjusting the 6.7 keV line intensity.*

	Emission lines			Continuum	
	6.4 keV	6.7 keV	7.0 keV	photon index	normalization
Unit	$(10^{-8})^{\dagger}$	$(10^{-8})^{\dagger}$	$(10^{-8})^{\dagger}$		$(10^{-8})^{\ddagger}$
$l = -20°$	6.3±1.0	8.9±1.0	< 1.4	1.6±0.1	27±1
$10° < \|l\| < 30°$	1.6±0.2	5.8±0.3	0.9±0.2	2.5±0.1	12.6±0.1
excess	3.9±1.1	–	–	< 1.2	5.7±1.9

* The error ranges in this table are calculated at 90% confidence levels.
† Absorption-corrected line flux in the units of photons s^{-1} cm^{-2} arcmin^{-2}.
‡ Normalization at 6.4 keV in the units of photons s^{-1} keV^{-1} cm^{-2} arcmin^{-2}.

Chapter 7

Discussion

In chapter 5 and 6, we have separately measured the scale heights and equivalent widths of the 6.4 keV, 6.7 keV, and 7.0 keV lines in the GCXE, GBXE, GRXE. Furthermore, we have found that there are enhancements of the 6.4 keV line relative to the 6.7 keV distribution in the GC east and $l = -20°$ regions and that the enhancements are associated with molecular gas. In this chapter, we will first discuss the origin of the 6.4 keV enhancements based on the result of spectral analysis. Then, we will discuss the origin of the GDXE on the basis of the observed scale heights and equivalent widths.

7.1 Origin of the 6.4 keV enhancements

Recently, a common candidate of the origin of 6.4 keV line emission in the GDXE has been considered to be CVs (Yuasa *et al.*, 2012). However, the excess emissions discovered in this dissertation have only the 6.4 keV line while the CVs usually exhibit the 6.4 keV, 6.7 keV, and 6.9 keV lines (Hellier *et al.*, 1998; Ezuka and Ishida, 1999; Hellier and Mukai, 2004). The spatial distribution of the 6.4 keV line intensity strongly indicates that the excess emissions are emitted from neutral iron atoms in molecular gas. Since temperature of the molecular gas in interstellar space is at most 100 K, X-rays cannot be generated. Some particles with higher energy than the ionization energy of an iron K-shell electron, such as cosmic-ray protons, electrons, or X-rays, should be bombarded on the molecular gas.

The equivalent width of a 6.4 keV line depends on the irradiating particles and their spectral index as shown in figure 7.1. In the case of cosmic-ray bombardment, the 6.4 keV line is produced via inner-shell ionization by protons (Dogiel *et al.*, 2011) or by electrons (Valinia *et al.*, 2000; Yusef-Zadeh *et al.*, 2002), while the continuum is due to inverse bremsstrahlung (for protons) or bremsstrahlung (for electrons). Figure 7.2 shows the cross sections for producing the 6.4 keV line and bremsstrahlung at 6.4 keV by the impact of electrons and protons. The energy range of the protons that produce the 6.4 keV line is mainly the MeV band while that of the electrons is mainly the keV band. The photon index of the observed X-ray spectrum is not the same as the particle index. We calculate the photon index in the case of a certain particle index assuming optically-thin line emission based on Baring *et al.* (2000). The result is shown in figure 7.3.

As for the X-ray irradiation, the 6.4 keV line is produced via photoionization by X-rays with energy higher than 7.1 keV (K-edge) while the continuum is due to Thomson scattering. The photon index of the observed X-ray spectrum is the same as that of the irradiating X-rays in the energy band

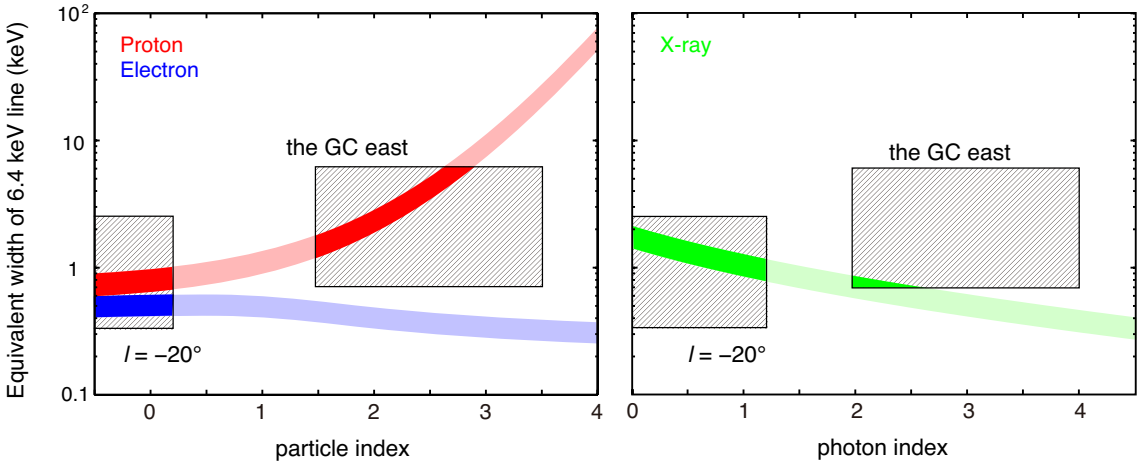

Figure 7.1. (left) Equivalent width of the 6.4 keV line as a function of particle index (Dogiel *et al.*, 2011) with the iron abundance of 1–1.5 solar (see text). The error regions of the particle index and equivalent width for the GC east and the $l = 20°$ regions are shown by the hatched region. The red and blue belts are the calculated values for protons and electrons, respectively. The thick red and blue regions are the acceptable ranges for the proton and electron scenarios, respectively. (right) Same as the left, but of photon index (Tsujimoto *et al.*, 2007). The green belt and the thick green region are the calculated values and the acceptable range for the X-ray scenario, respectively.

of 2–10 keV, which we treat in this dissertation.

In both the scenarios, the equivalent width depends on the iron abundance (Tsujimoto *et al.*, 2007; Dogiel *et al.*, 2011). The metal abundances were determined in the GC region by X-ray observations of the HP to be ~ 1.9 solar for sulfur, argon, calcium but $\sim$1.2 solar for iron (Nobukawa *et al.*, 2010; Uchiyama *et al.*, 2013). Muno *et al.* (2004) reported a similar result. The iron abundance of 1–1.5 solar was also measured in the XRNe in Sgr B with the absorption of the iron K-edge (Nobukawa *et al.*, 2011). Giveon *et al.* (2002) obtained 2 solar for heavy elements of neon, sulfur, and argon (not of iron), and Cunha *et al.* (2007) and Martin *et al.* (2015) measured the iron abundance to be 1–1.5 solar. Therefore, we adopt the iron abundance of 1–1.5 solar as is shown in figure 7.1 with the colored belts. The equivalent width in the X-ray scenario also depends on the angle θ between the line of sight and the incident photon direction (Tsujimoto *et al.*, 2007). Figure 7.1 shows the result of the reflection angle $\theta = 90°$, which gives the maximum equivalent width. The shapes of the equivalent width curves roughly reflect the ratio of cross sections for producing the 6.4 keV line and bremsstrahlung (figure 7.2). The hatched regions in figure 7.1 indicates the equivalent width ranges of the statistical and systematic errors in the GC east and $l = -20°$ regions.

All the scenarios are accepted for the $l = -20°$ region. On the other hand, in the GC east region, the allowed parameter region completely excludes the electron origin. Then, we discuss the others, the X-ray and proton scenarios for the GC east in the next subsection.

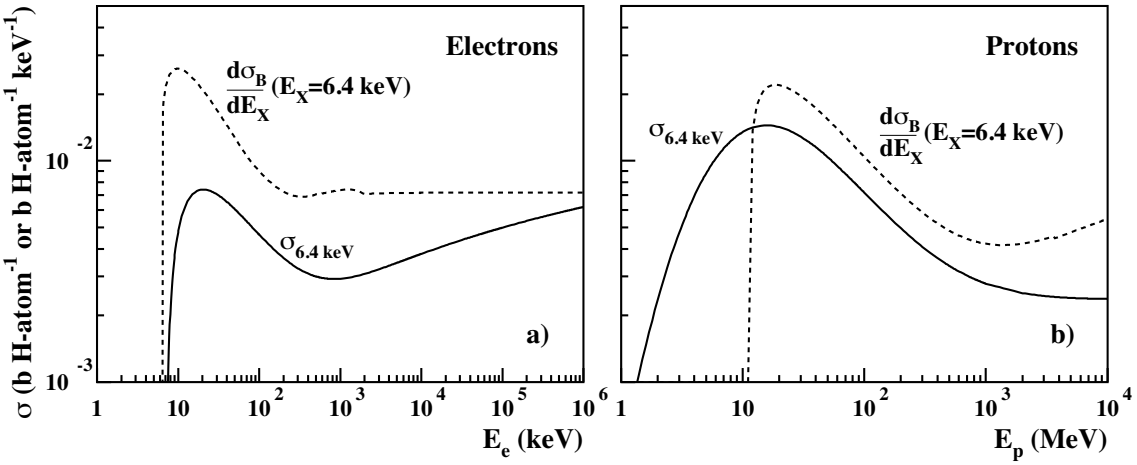

Figure 7.2. Cross section for producing the 6.4 keV line by the impact of fast electrons and protons. Solid lines show the cross section (in units of barn per ambient H-atom) for producing the 6.4 keV line by the impact of fast protons or electrons with the abundance of 1 solar. Dashed lines show the differential cross section (in barn per H-atom per keV) for producing 6.4 keV X-rays by bremsstrahlung (electrons; left panel) and inverse bremsstrahlung (protons; right panel) in a medium composed of hydrogen and helium with the density ratio of 1 : 0.1. Both the panels are taken from Tatischeff *et al.* (2012).

7.1.1 The GC east region

X-ray irradiation

In the X-ray irradiation scenario, the 6.4 keV line flux depends on the irradiating source flux, the hydrogen column density ($N_{\rm H}$) of the molecular gas (or cloud), and the distance (D) between the irradiating source and the target. The hydrogen column density $N_{\rm H}$ =(2–6)×10^{22} cm^{-2} is obtained by multiplying the ^{12}CO line intensity in figure 6.5 by the conversion factor (called X-factor) of 0.7×10^{20} cm^{-2} (K·km s^{-1})$^{-1}$ (Torii *et al.*, 2010), which is measured near the GC.

A possible irradiating source is the supermassive black hole Sgr A*, as for the XRN model invoked for the GC region (Sunyaev *et al.*, 1993; Koyama *et al.*, 1996; Ponti *et al.*, 2010). In this case, the source luminosity should be $L_{\rm X}\sim10^{40}$ (D/450 pc)^2 erg s^{-1} about 1500×(D/450 pc) years ago, where D is the distance of the 6.4 keV line emitting region from Sgr A*. For the XRN in Sgr B, the luminosity of Sgr A* was $\sim10^{39}$ erg s^{-1} about 300 years ago (Murakami *et al.*, 2000; Revnivtsev *et al.*, 2004). Brighter flares of $\sim10^{41-43}$ erg s^{-1} in the far past (10^5–10^7 years ago) have been proposed to explain the Fermi bubbles and the recombining plasma in the south region of the GC (Su *et al.*, 2010; Nakashima *et al.*, 2013). Thus, many big flares in the interval period between these two epochs (∼700–1500 years ago) may be conceivable. However, this scenario has two difficulties.

The first difficulty comes from the longitudinal distribution of the excess flux of the 6.4 keV line. The observed excess flux is proportional to the ^{12}CO intensity, which means that the X-ray intensity from Sgr A* is almost constant, and does not decrease as the square of the Galactic longitude, or the distance from Sgr A*; the past Sgr A* flares should have smoothly increasing flux with the square of the look-back time. A monotonous smooth decrease of flux should continue during 700–1500 years ago, which is artificial, although not completely rejected.

The second difficulty comes from the flux ratio of the 6.4 keV line to the ^{12}CO intensity (here, α)

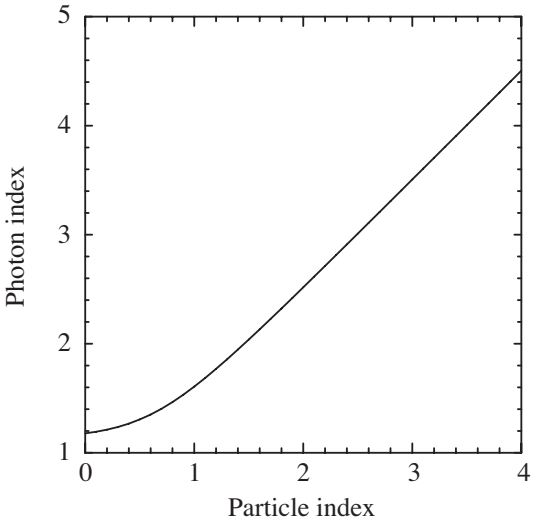

Figure 7.3. Calculated photon index of X-ray radiated by cosmic-ray particles as a function of the particle index based on Baring *et al.* (2000).

in the molecular cloud Clump 2 (see figure 6.6). Clump 2 extends toward the north from the Galactic plane and has an elliptical shape with major and minor axes of $\sim 1.^\circ 1$ and $\sim 0.^\circ 5$, respectively. We estimate the excess 6.4 keV line flux from the on-plane ($b \sim -0.^\circ 04$; Obs. ID=507073010) and off-plane ($b \sim 0.^\circ 15 - -0.^\circ 40$; Obs.ID=507074010 and 507075010) parts of Clump 2 by subtracting the symmetrical component from the observed flux, and obtained α of $(5.9 \pm 0.7) \times 10^{-11}$ and $(2.1 \pm 0.6) \times 10^{-11}$ for the on- and off-plane parts, respectively (unit is photons s^{-1} cm^{-2} $arcmin^{-2}$ $(K \cdot km\ s^{-1})^{-1}$). Since the flux from Sgr A* would be equal in the small separation angle between on- and off-plane parts, α should be also equal, which is in conflict with the observed values. From these two difficulties, we regard that the X-ray irradiation by Sgr A* is unlikely.

The other possibility is that irradiation of many X-ray binaries in the east is responsible for the 6.4 keV line. This idea is essentially the same as Molaro *et al.* (2014). Assuming that a mean spectrum of the relevant X-ray binaries is a power law with the photon index of $\Gamma = 3$, and is surrounded by cold material with $N_{\rm H} = 2\text{–}6 \times 10^{22}$ cm^{-2}, a fraction of 0.03–0.1% of the total 2–10 keV flux is converted to 6.4 keV X-rays. We estimate the excess 6.4 keV luminosity in total to be 3×10^{33} erg s^{-1} in the relevant area of $2.^\circ 0 \times 0.^\circ 2$. Then, a total luminosity of 3×10^{36}–10^{37} erg s^{-1} is required to the sources inside the area. This flux exceeds the total luminosity of the GRXE in this region ($\sim 3 \times 10^{35}$ erg s^{-1}) by one or two orders of magnitude. No source brighter than 10^{35} erg s^{-1} is found in this area. Therefore, this scenario requires a source with more than one or two orders of magnitude brighter flares within the relevant regions and duration of the past ~ 1000 years. In addition, the reflection angle θ should be distributed randomly. Then the equivalent width integrated over the reflection angle θ is ~ 1.3 times lower than the green belt in figure 7.1 (reflection angle $\theta = 90°$), and hence is out of the allowed range. Thus this scenario is also unlikely. We regard the proton-bombardment scenario as the most probable origin of the excess in the GC east region.

Cosmic-ray Bombardment

In the proton model, the excess flux of the 6.4 keV line $I_{6.4\,\mathrm{keV}}$ is given by

$$I_{6.4\,\mathrm{keV}} = \frac{1}{4\pi} N_{\mathrm{H}} \int \sigma_{6.4\,\mathrm{keV}}\, v\, A \left(\frac{E_{\mathrm{p}}}{1\ \mathrm{MeV}}\right)^{-p} dE_{\mathrm{p}}, \tag{7.1}$$

where $\sigma_{6.4\ \mathrm{keV}}$, v, A, E_{p} and N_{H} are the cross section to produce the 6.4 keV line by protons, the velocity, the number density at 1 MeV and the energy of protons, and the line-of-sight hydrogen column density, respectively. The spectral index p of 2.5 is adopted from the best-fit photon index of 3 (see figre 7.3). Using the X-factor of 0.7×10^{20} cm^{-2} (K$\cdot$km s^{-1})$^{-1}$ (Torii *et al.*, 2010), the 6.4 keV line flux is expressed as the ^{12}CO line intensity multiplied by the conversion factor α, which is measured to be 4.2×10^{-11} photons s^{-1} cm^{-2} arcmin^{-2} (K$\cdot$km s^{-1})$^{-1}$ in figure 6.5. The cross section $\sigma_{6.4\mathrm{keV}}$ has a peak at 10 MeV and rapidly decreases below 1 MeV and above 50 MeV (Paul and Sacher, 1989). We set the integration range to be 1–50 MeV, and then obtained the normalization $A = 1.4 \times 10^{-5}$ protons cm^{-3} and the energy density of 20 eV cm^{-3}. When the integration range is expanded to be 0.1–1000 MeV, the energy density becomes 80 eV cm^{-3}. This is about one or two orders of magnitude higher than the canonical value ~ 1 eV cm^{-3} that is determined by observing high-energy cosmic rays (Neronov *et al.*, 2012).

Tatischeff *et al.* (2012) calculated an energy conversion rate from protons to the 6.4 keV line to be 10^{-6} or less. Since the total luminosity of the 6.4 keV line emission is 3×10^{33} erg s^{-1}, the proton power of $> 3 \times 10^{39}$ erg s^{-1} is estimated. This is not far from the energy $\sim 2 \times 10^{39}$ erg s^{-1} that protons input to the GC (Dogiel *et al.*, 2013).

7.1.2 The $l = -20°$ region

X-ray irradiation

Figure 7.1 does not exclude any scenario in the $l = -20°$ region. We first discuss the X-ray origin in the following. The hydrogen column density N_{H} =(5–6)$\times 10^{22}$ cm^{-2} is obtained by multiplying the ^{12}CO line intensity in figure 6.8 by the conversion factor (X-factor) of 2×10^{20} cm^{-2} (K$\cdot$km s^{-1})$^{-1}$ (Dame *et al.*, 2001).

A possible irradiating source is a nearby bright X-ray binary (Molaro *et al.*, 2014). The source luminosity should be $L_{\mathrm{X}} \sim 4 \times 10^{38}$ (D/100 pc)^2 erg s^{-1}, where D is the distance of the 6.4 keV line emitting region from the irradiating source. This luminosity is comparable to or higher than the Eddington luminosity of a neutron star $L_{\mathrm{Eddington}} = 2 \times 10^{38}$ (D/100 pc)^2 erg s^{-1}. There are two possible sources which located at the projected distance of 70–150 pc: the LMXB GX 340+0 and the blackhole candidate 4U 1630−472. However, both the sources are located at 10–11 kpc from the sun (Grimm *et al.*, 2002; Seifina *et al.*, 2014)[1] while the molecular clouds which associated with the 6.4 keV excess located at 4–8 kpc. There is no possible irradiating source in the vicinity. In the GC region, the supermassive black hole, Sgr A* was active and irradiated the surrounding molecular clouds several hundred years ago (e.g. Koyama *et al.*, 1996). However, there is no such a special source in this area.

[1] Since no optical counter part has not been identified for 4U 1630−472, its distance from the Sun has an uncertainty. Seifina *et al.* (2014) estimate that the distance is large ($\geqslant 10$ kpc) because the source is heavily absorbed in soft X-rays.

In the same manner as the case of the GC east, we also discuss contribution of many faint point sources. This scenario was rejected for the GC east. The hydrogen column density $N_{\rm H}$ = 5–6 × 10^{22} cm^{-2} and the surface intensity of the excess 6.4 keV line is $\sim 4{\times}10^{-8}$ photons s cm^{-2} arcmin^{-2} are comparable to those of the GC east. Thus, the luminosity of the many point sources $L_{\rm X} > 10^{36}$ erg s^{-1} is required assuming the same emitting region as the GC east. However, the total luminosity of the GDXE in this region is $\sim 2 \times 10^{35}$ erg s^{-1}, and hence this scenario is rejected. Therefore, the X-ray scenario would be unlikely.

Cosmic-ray bombardment

Also in the $l = -20°$ region, the most plausible scenario is the cosmic-ray bombardment. Since whether the irradiating particles are protons or electrons cannot be constrained, we estimate the energy density for both the case. Using equation (7.1), we obtained the energy density of 20 eV cm^{-3} in the energy range of 0.1–1000 MeV and 0.03 eV cm^{-3} in the energy range of 0.1–1000 keV for protons and electrons, respectively. Although the LECR electron origin cannot be ruled out, the proton origin is acceptable as is adopted to the case of the GC east region.

The total observed luminosity of the excess 6.4 keV line emission is at least 1×10^{33} erg s^{-1}. Here, we assume the excess mainly comes from molecular clouds located at the distance of 5 kpc. Since the efficiency for the production of the 6.4 keV line is 10^{-6} or less in both of the proton and electron cases (Tatischeff *et al.*, 2012), the kinematic power of $> 1 \times 10^{39}$ erg s^{-1} is estimated.

7.2 Scale heights and equivalent widths of the GDXE

7.2.1 Comparison with previous study

Scale height

The Tenma satellite, which discovered the intense iron line, found that the scale heights of the continuum (2–10 keV) and the iron lines are 100–300 pc assuming the emission comes from a disk with a radius of 10 kpc (Koyama *et al.*, 1986b). Yamauchi and Koyama (1993) determined the scale height of the 6.7 keV line to be 100 pc by the Ginga survey of the Galactic ridge. Valinia and Marshall (1998) found that the continuum emission in the 5–8 keV band from the $|l| < 15°$ region has two exponential components and the scale heights of the thin and broad ones are 70 pc and 500 pc, respectively. Revnivtsev and Molkov (2012) made the surface brightness profile of the GRXE continuum in the 4.3–10.5 keV band across the Galactic plane from $b = 0°$ to $b = -30°$ at $l = 18.^{\circ}5$ by using RXTE, and obtained the scale height of 107 ± 5 pc. Uchiyama *et al.* (2013) measured the latitudinal distributions of the 6.4 keV and 6.7 keV lines separately as well as the 5–8 keV continuum in the GCXE and GRXE by using Suzaku. They reported that the e-folding scale heights of the 6.4 keV in the GCXE and GRXE are ∼30 pc and ∼150 pc, respectively, while those of the 6.7 keV and the continuum in the GCXE and the GRXE are ∼40 pc and ∼400 pc, respectively.

The measured scale heights of the 6.4 keV, 6.7 keV, and 7.0 keV lines and the hard X-ray continuum of the GCXE in this work are almost consistent with the results in Uchiyama *et al.* (2013), but there is discrepancy for the GRXE. Our result of the scale height of the 6.7 keV and 7.0 keV lines and the hard continuum in the GRXE of ∼140 pc is almost consistent with the results obtained by Tenma,

Ginga, and RXTE. The scale heights of the GRXE measured by Uchiyama *et al.* (2013) are systematically large but are closer to those in the GBXE in our work. Actually, a majority of the data that Uchiyama *et al.* (2013) used for the GRXE are extracted from the $2^\circ < |l| < 4^\circ$ region, which mainly consists of the GCXE and GBXE based on our result.

Revnivtsev *et al.* (2009) performed a Chandra deep observation (∼1 Msec) at $(l, b) = (0.^\circ1, -1.^\circ4)$ (CBF). It is true that the CBF is near the GC. However, figure 5.2 and figure 5.3 show that contribution of the GCXE is ≤ 10% of the GBXE at $b_* = 1.^\circ4$ in the $0.^\circ0 < l < 385.^\circ5$ region, and thus the CBF is dominated by the GBXE.

Equivalent width

In section 4.3, we obtained the equivalent widths of the iron lines as is listed in table 7.1. Uchiyama *et al.* (2013) show the mean equivalent widths of the 6.4 keV and 6.7 keV lines in the GRXE ∼ 110 eV and ∼ 490 eV, respectively. Given the mixture of the GCXE and GBXE in the data used in Uchiyama *et al.* (2013) as mentioned before, our result would be consistent with them.

7.2.2 Comparison with point sources

A common idea for the origin of the GDXE is a superposition of many point sources such as CVs and ABs (e.g. Revnivtsev *et al.*, 2009). Previous studies focused on an X-ray luminosity function or spectra of point sources, and thus verified whether the integrated surface brightness and spectrum match the observed GDXE. In chapter 5, we separately measured the scale heights and equivalent widths of the 6.4 keV, 6.7 keV, and 7.0 keV lines and discovered that the values are different among the GCXE, GBXE, and GRXE. We below examine the point-source scenario by comparing the scale heights and equivalent widths of CVs and ABs with those of the GCXE, GBXE, and GRXE.

Scale heights of CVs in the solar neighbourhood (distance $\lesssim$ 1 kpc) are measured by several authors (Patterson, 1984; Ak *et al.*, 2008; Revnivtsev *et al.*, 2008). Most ABs composed of G or K stars and a small fraction (∼15%) are F stars (Strassmeier *et al.*, 1993). We adopt scale heights of G and K stars as that of ABs. We show the scale heights of CVs and ABs in table 7.2.

Molecular gas distribution may provide a hint of the origin of the GDXE. We measure latitudinal distributions of the molecular gas using NANTEN data in the GC region ($|l| < 1^\circ$) and the Galactic plane ($2^\circ < |l| < 40^\circ$). Latitude distributions of the two regions are shown in figure 7.4. By fitting the plots in the range of $|b| < 2^\circ$ with an exponential function, we obtained the scale heights of the ^{12}CO as shown in table 7.2.

The typical equivalent widths of CVs are listed in table 7.1. CVs are divided into two categories by their magnetic field strengths, namely magnetic CVs and non-magnetic CVs. The mass accretion in magnetic CVs and non-magnetic CVs are different; typical equivalent widths of iron K-shell lines from the two categories are also different. In magnetic CVs, namely polars and intermediate polars, magnetic filed of a white dwarf is so strong that it controls the accretion flow from a companion star. The accretion matter forms an accretion column, which radiate mainly in X-rays. Magnetic CVs typically have luminosities of $\sim 10^{32}$–10^{34} erg s^{-1}. The equivalent widths of the three iron K-shell lines of magnetic CVs are well studied by many authors (e.g. Hellier *et al.*, 1998; Ezuka and Ishida, 1999; Hellier and Mukai, 2004). Although there is dispersion of ∼ 30 eV between authors, typical equivalent widths are ∼ 130 eV, ∼ 160 eV, and ∼ 90 eV for the 6.4 keV, 6.7 keV, and 7.0 keV lines,

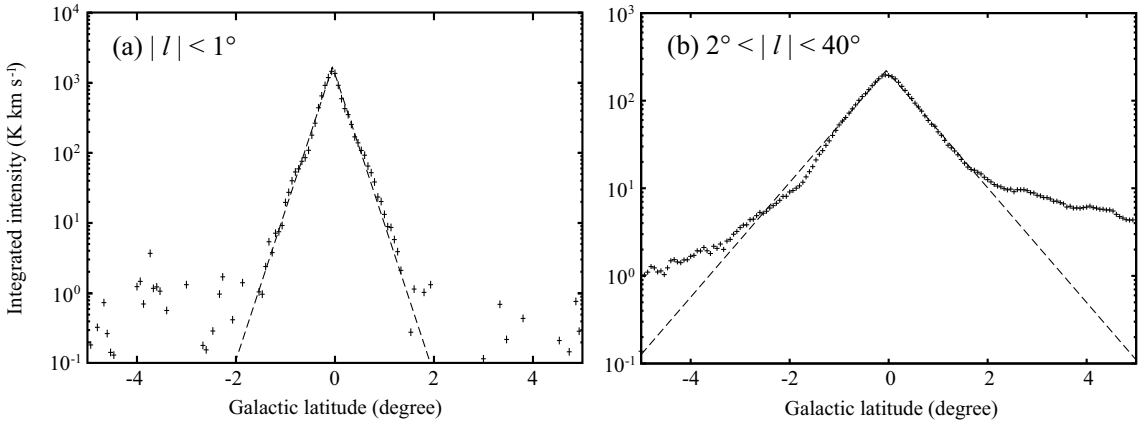

Figure 7.4. (a) Latitudinal distribution of integrated in intensity of ^{12}CO in the CMZ ($|l| < 1.°0$). Integrated range is the same as figure 6.5 and 6.6. The dashed line shows the best-fit model consisting of an exponential function, which is symmetric with respect to the Galactic plane ($b = -0.°046$). (b) same as (a), but in the Galactic plane ($2° < |l| < 40°$). All velocities are integrated. The data are provided by Kazufumi Torii (private communication).

respectively. On the other hand, 90% of CVs fall into non-magnetic CVs. Most common type of non-magnetic CVs are dwarf novae with luminosities of $\sim 10^{30}$–10^{32} erg s^{-1} (e.g. Patterson, 1984). Dwarf novae are considered to change their luminosities via instabilities in accretion disk (Osaki, 1974). Dwarf novae show the 6.7 keV line whereas they do not so strongly emit the 6.4 keV line. ABs, which have luminosities of 10^{27}–10^{31} erg s^{-1}, emit a strong 6.7 keV line, but they show little emission for the other two lines. Although X-ray spectra from thermal plasma in non-magnetic CVs and ABs are well studied, there is few study that gives direct information about the equivalent widths for the three iron K-shell lines. We use the averaged equivalent widths obtained by Suzaku observations of 9 dwarf novae and 9 ABs (Nobukawa *et al.* in prep.).

Sazonov *et al.* (2006) estimate contribution of ABs and CVs to the GDXE of $(2-3):1$ in the luminosity range of 10^{28}–10^{31} erg s^{-1}, based on an X-ray luminosity function of nearby X-ray sources. In a similar way, Warwick (2014) also claimed that the bulk of the GRXE signal (80% in the restricted 6–10 keV band) can be attributed to the X-ray emission of these two populations, with a rough 3 : 1 split between the ABs and CVs contributions. Since ABs and CVs represent old stellar populations, their X-ray luminosity function normalized to the stellar mass is not expected to vary significantly across the Galaxy (Sazonov *et al.*, 2006). We thus assume that ABs and CVs contribute to the iron K-shell iron with a 3 : 1 split. We also assume that magnetic CVs and non-magnetic CVs account for 90% and 10% in the total CVs, respectively, because the number density of non-magnetic CVs is considered to be 10 times larger than the magnetic CVs but the luminosity of non-magnetic CVs is 100 times less than the magnetic CVs. Then superposition of these point sources gives the equivalent widths of 50 eV, 300 eV, and 70 eV for the 6.4 keV, 6.7 keV, and 7.0 keV lines, respectively. We compare these values (hereafter 3ABs+CVs) with equivalent widths in the GRXE, GCXE and GBXE.

Table 7.1. Equivalent widths of CVs and ABs.

Object	Equivalent width (eV)		
	6.4 keV	6.7 keV	7.0 keV
magnetic CVs*	~ 130	~ 160	~ 90
non-magnetic CVs†	~ 70	~ 500	~ 130
ABs†	~ 20	~ 340	~ 60
3ABs+CVs	~ 50	~ 300	~ 70
GCXE	145 ± 3	527 ± 4	221 ± 3
GBXE	61 ± 11	443 ± 14	160 ± 14
GRXE	97 ± 12	428 ± 15	117 ± 19

* Hellier *et al.* (1998); Ezuka and Ishida (1999); Hellier and Mukai (2004).
† Nobukawa *et al.* in prep.

7.2.3 GRXE

Difference between 6.4 keV and 6.7 keV lines

We found that the scale height of the 6.4 keV line in the GRXE is systematically smaller than those of the 6.7 keV and continuum X-rays. This indicates that the 6.4 keV and 6.7 keV lines in the GRXE have different origins. The 6.7 keV line in the GRXE of ~ 140 pc is consistent with the point sources (ABs and CVs). The equivalent width of the 6.7 keV line (428 ± 15 eV) cannot be explained by superposition of 3ABs+CVs ($\sim$300 eV) as estimated in section 6.2.2 (table 7.1). Dwarf novae with the equivalent width ~ 500 eV might contribute to the GRXE more significantly.

On the other hand, any mixing ratio of the point sources cannot explain the equivalent widths of the 6.4 keV line. In the case of the combination of 3AB+CVs, the 6.4 keV line equivalent width is only 50 eV, which is 50% of the 6.4 keV line intensity. Another origin is required to account for at least the half of the 6.4 keV line emission in the GRXE. The scale height of the 6.4 keV line is similar to that of the molecular gas on the Galactic plane. As already mentioned, if the molecular gas is irradiated by X-rays or cosmic-ray particles, prominent 6.4 keV line emission is generated. In fact, as investigated in chapter 6, the excesses of the 6.4 keV line emission in the GC east and $l = -20^\circ$ regions are associated with the molecular gas.

Origin of the 6.4 keV line

As with discussion about the origin of the 6.4 keV excesses, we discuss the X-ray-irradiating scenario in the global scale. This scenario is in principle the same as Molaro *et al.* (2014), who claimed that scattered photons from the ISM originating LMXBs are able to contribute, on average, 10%–30% of the GRXE. In the $10^\circ < |l| < 30^\circ$ region, averaged ^{12}CO integrated intensity is ~ 150 K (km/s)$^{-1}$, which is translates into $N_{\rm H} \sim 3 \times 10^{22}$ cm^{-2} using the X-factor (Dame *et al.*, 2001). X-ray observations in this region also give $N_{\rm H}$ of 3–4$\times 10^{22}$ cm^{-2} (e.g. Yasumi *et al.*, 2014; Takata *et al.*, 2015; Nobukawa *et al.*, 2015b).

Here we caution that an X-ray source illuminate only its vicinity and the source cannot illuminate all the cold matter along the ($\sim$ 10 kpc) line of sight because the X-ray intensity decreases with

Table 7.2. Scale heights of CVs, ABs, and molecular gas (^{12}CO).

Object		Scale height (pc)
CV*		130–160
AB†		150–300
molecular gas	($\|l\| < 1°$)	28 ± 1
	($2° < \|l\| < 40°$)	92 ± 1
GCXE	6.4 keV	31 ± 3
	6.7 keV	36 ± 3
GBXE	6.4 keV	161 ± 50
	6.7 keV	314 ± 95
GRXE	6.4 keV	70 ± 17
	6.7 keV	142 ± 17

* Obtained from the vicinity of the solar system (< 1 kpc) (Patterson, 1984; Ak *et al.*, 2008; Revnivtsev *et al.*, 2008).
† Obtained from the vicinity of the solar system (< 1 kpc) (Gilmore & Zeilik 2000).

the squared distance between the source and the target. The scale height of the cold matter, i.e. molecular gas, is ~ 100 pc, and the line-of-sight length is assumed to be the same as the Galactic diameter, ~ 10 kpc. If the X-ray source with the same spectral shape as GX 3+1 (Piraino *et al.*, 2012) is surrounded by molecular gas with the above size, 0.005% of the total 2–10 keV flux of the irradiating source is converted to the 6.4 keV line emission. We estimate the 6.4 keV luminosity in total to be 3×10^{35} erg s^{-1} in the relevant area of $2 \times (20° \times 1.\!°0)$ using the parameters in table 5.1. Then, a total luminosity of 6×10^{39} erg s^{-1} is required to the sources inside the area. Since the total luminosity of LMXBs in the same region is $\sim 6 \times 10^{38}$ erg s^{-1} (Grimm *et al.*, 2002; Molaro *et al.*, 2014), the 6.4 keV line due to the X-ray irradiation contributes only 10% of the 6.4 keV line emission in the GRXE.

The most possible origin is still cosmic-ray bombardment as with the GC east and the $l = -20°$ regions. We already estimated that at least $\sim 50\%$ of the 6.4 keV line emission should have another origin than the point sources. If this is of the cosmic-ray bombardment, the energy densities would be ~ 10 eV cm^{-3} and ~ 0.01 eV cm^{-3} for the protons and electrons cases, respectively. Combined with the energy density obtained in the GC east region (80 eV cm^{-3}) and the $l = -20°$ region (20 eV cm^{-3}), the energy density of LECR protons on the Galactic plane would commonly be higher than the canonical value ~ 1 eV cm^{-3} that is determined by observing high-energy cosmic rays (Neronov *et al.*, 2012). The total luminosity of the 6.4 keV line emission requires the energy injection to cosmic rays of $> 3 \times 10^{41}$ erg s^{-1}.

Among the Galactic plane, the regions where molecular gas is rich would show the 6.4 keV line enhancements. The GC east region contains the giant molecular cloud Clump 2. The $l = -20°$ region is located at the line of sight tangent to the Near 3 kpc arm; the molecular gas column density increases at a tangent to a spiral arm. There exists other tangent regions in the Suzaku observation range: the tangents to the Far 3 kpc arm at $l \sim 25°$ and the Scutum-Centaurus arm at $l \sim -50°$. Also these regions exhibit the indication of the 6.4 keV line enhancement (figure 5.5e) although not

statistically significant. The 6.4 keV line enhancements should be also due to the higher density of LECRs than other regions on the Galactic plane.

7.2.4 GCXE

The scale heights of the 6.4 keV and 6.7 keV lines in the GCXE of $\sim$ 30 pc and $\sim$ 40 pc are much smaller than the CVs and ABs although there is an uncertainty whether the scale heights of point sources obtained in solar neighbourhood can be adopted even in the peculiar environment of the GC. Uchiyama *et al.* (2011) measured the scale height of the 6.7 keV in the GC, and found that it shows 3.8 times larger excess than the stellar distribution model assuming all of the GBXE and GRXE are due to point sources. A similar result was obtained by comparing a stellar density map constructed from an infrared observation with the latitudinal profiles of the 6.7 keV line (Nishiyama *et al.*, 2013; Yasui *et al.*, 2015). The smaller scale heights of the 6.4 keV and 6.7 keV lines than the stellar distribution require contribution of other origins, which would be diffuse emission in the GCXE. Interestingly, the scale heights of the 6.4 keV and 6.7 keV lines in the GCXE are consistent with that of the molecular gas in the GC. It is possible that the major fraction of the 6.4 keV line in the GC come from the molecular gas origin and the 6.7 keV line may also originate from sources correlated with the molecular clouds.

The equivalent widths of the three lines in the GCXE are larger than those in the GBXE and GRXE. Any mixing ratio of ABs and CVs cannot explain either iron line. The assumption that the iron abundance in the GC is 2–3 times larger than the solar one may be explained the observed equivalent widths. However, observational results are against the assumption. As discussed in section 7.1, a reasonable iron abundance in the GC should be 1–1.5 solar, and thus the large equivalent widths in the GCXE also require other origins than the superposition of point sources.

7.2.5 GBXE

The scale heights of the 6.4 keV and 6.7 keV lines in the GBXE of $\sim$ 160 pc and $\sim$ 320 pc are consistent with those of the CVs and ABs although those values are obtained from data in the solar neighbourhood (section 7.2.2). The equivalent width of the 6.4 keV and 6.7 keV lines in the GBXE is marginally consistent with those of 3ABs+CVs while the equivalent widths of the 7.0 keV line in the GBXE are 2 times higher. The equivalent widths of the three lines are almost explained when dwarf novae more contribute to the GBXE than the assumption. Combination of ABs and CVs would significantly contribute to the GBXE. Our result is consistent with Revnivtsev *et al.* (2009), who reported that more than 80% of the X-ray emission in the GBXE is resolved into point sources.

7.3 Where low-energy cosmic rays come from?

We demonstrated that significant fraction of the 6.4 keV line emission in the GRXE is generated by the LECR protons (~MeV) or electrons (~keV). LECRs are affected by solar modulation, and hence their intensity and spectral shape in the interstellar space cannot be measured inside the solar system. In fact, while characteristics of GeV and TeV cosmic rays have gradually been revealed thanks to GeV and TeV gamma-ray observations, the LECRs have been a totally unknown component. Only

Voyager-I, which has got away from the heliosphere and reached 122 astronomical units in 2012, measured LECRs in the interstellar space (Stone *et al.*, 2013).

The energy density of the LECR protons measured by Voyager-I is ∼1 eV cm^{-3} although the LECR intensity immediately outside the heliosphere may be lower than the Galactic intensity because of modulation in the local interstellar medium (Stone *et al.*, 2013). Our measurement using the 6.4 keV line has been performed on the Galactic intensity for the first time. The energy density of LECR protons measured in the GC east, $l = -20°$ region and the entire GRXE ranges from $\sim$ 10–80 eV cm^{-3} in the 0.1–1000 MeV band, which is one order of magnitude higher than the Voyager-I result. Above the GeV band, the cosmic-ray spectrum has the particle index of 2.7 and the energy density above the GeV band is 1 eV cm^{-3}. In the case that the cosmic-ray spectrum keeps its shape below 1 GeV, the energy density in the 0.1–1000 MeV band is estimated to be $\sim$ 600 eV cm^{-3}. Our result is one order of magnitude lower than the estimation.

The origin of LECRs have rarely discussed so far due to poor information. One clue to the origin may come from the diffusion length of LECRs: only a few tens of parsecs (Dogiel *et al.*, 2011). Therefore LECRs should be produced *in situ*. SNRs and pulsar wind nebulae are thought to generate Galactic cosmic rays. However, in either the GC east, $l = -20°$ region or the entire GRXE, no candidate source is found in the vicinity of the observed regions. Another acceleration mechanism is required.

One possible scenario is stochastic acceleration. However, the acceleration is too slow in general. Amano *et al.* (2011) argued that stochastic acceleration powered by Alfvénic turbulence can efficiently generate cosmic rays and that large velocity dispersion of $\sim$ 100 km s^{-1} in the CMZ indicates the presence of turbulence. Since also Clump 2 at $l = 3°$ exhibits large velocity dispersion of $\sim$ 100 km s^{-1} (Bania, 1977; Torii *et al.*, 2010), the stochastic acceleration can produce the LECR protons in the GC east region. Nevertheless, the stochastic acceleration would not be necessarily efficient in the other regions.

Another possibility is a reconnection of magnetic field (Lesch and Reich, 1992; Yokoyama *et al.*, 2000). The magnetic field is amplified by the rotation of the Galactic disk, and expands from the disk to outside by the Parker instability. The expanding magnetic loop collides with ambient field lines and induces magnetic reconnection. Since the velocity dispersion of Clump 2 suggests the existence of magnetic loop (Fukui *et al.*, 2006), the LECR protons in the GC east can be accelerated by the reconnection. Also High-velocity clouds or supernovae can trigger the magnetic reconnection in the Galactic disk (Kerp *et al.*, 1994; Tanuma *et al.*, 1999). The LECRs in the $l = -20°$ region and the entire ridge region can be energized by the magnetic reconnection.

The LECRs may be secondary particles that are produced by interactions of higher-energy cosmic rays with the ISM. In the proton scenario, the energy density of $\sim$ 10–80 eV cm^{-3} in the MeV band is far higher than 1 eV cm^{-3} that is measured above the GeV band, and thus the secondary protons cannot explain the measured LECRs. In the electron case, on the other hand, the energy density in the keV band would be $\sim$ 0.01–0.03 eV cm^{-3}, which is much below that of the GeV band. Therefore the LECR electrons could be the second electrons.

The LECRs could be possibly produced by undiscovered SNRs on the Galactic plane or an unknown acceleration mechanism. In any origin, since no observational result that demonstrates excess emission in the GeV gamma-ray has been reported in ether the GC east or $l = -20°$ regions, the cosmic-ray particles are not necessary to be accelerated up to the GeV band.

In order to investigate the origin of LECRs, we need more information about their spectra and spatial distribution as well as about the ambient ISM. ASTRO-H (Takahashi *et al.*, 2014), the next Japanese X-ray astronomy satellite, will provide new clues as described in the next chapter.

LECRs are an efficient heating source of the ISM, and hence play a crucial role in the energetics and chemical evolution of the Milky Way. Our results demonstrate that the 6.4 keV line can be a unique probe to investigate LECRs. We found that their energy density could be one or two orders of magnitude higher than the canonical value of 1 eV cm^{-3} on the Galactic plane including the excess regions (in the proton origin). This means that the LECRs, which have been little focused on so far, should be taken into account in exploring characteristics of hydrodynamic process in our galaxy.

Chapter 8

Prospect for ASTRO-H

We have investigated the origin of the GDXE, especially of the 6.4 keV line emission, through this dissertation, and found that interaction of cosmic rays (protons) with molecular gas contributes to the 6.4 keV line emission in the GRXE. However, its attributable fraction has a large uncertainty because the equivalent width of the diffuse emission and the particle index of cosmic rays are unknown on the Galactic plane; even in the GC east and $l = -20°$ regions, there remain uncertainty in the spectral shape. ASTRO-H, which is planned to be launched in February 2016, will offer new insights into the origin of 6.4 keV line in the GDXE and contribution of LECRs.

ASTRO-H will provide high resolution spectroscopy (energy resolution < 7 eV at 6 keV; FWHM) with a micro-calorimeter array, the soft X-ray spectrometer (SXS). The SXS will discriminate the origin of the 6.4 keV emission by the line width. While electrons and X-rays generate a very narrow line with the line width of 1 eV, a proton-induced fluorescence line would be broad to ~ 10 eV due to multiple simultaneous ionization (Garcia *et al.*, 1973).

Figure 8.1 shows simulation of an SXS observation in the GC east region. We assume the spectral parameters of the GRXE obtained by Uchiyama *et al.* (2013) in principle. The ratio of intensities of neutral iron Kα_1 and Kα_2 lines is assumed to be 2 : 1 and the sum intensity of two lines is assumed to be the best-fit 6.4 keV line intensity in the integrated spectrum from the GC east region. We assume that a half of the 6.4 keV emission comes from point sources, where the line does not broad. Figure 8.1a shows the case that the other half originates from X-ray reflection. Only the upper limit of the line width of < 2 eV is obtained as shown in table 8.1. On the other hand, figure 8.1b shows the case that the other half of the 6.4 keV line emission is due to proton bombardment. The obtained line width is 5±2 eV. We can discriminate the two cases. As in the Suzaku observation of the GC east region, it would be meaningful to observe not only the east side but also the west side for comparison. We will definitely conclude the proton origin in the GC east region, and probably in the $l = -20°$region in a similar way.

The new satellite will also provide a broadband observation combined with a soft X-ray imaging spectrometers covering 0.4–12 keV and hard X-ray imaging spectrometers covering 5–80 keV, which will achieve more accurate determination of the spectral index of the continuum associated with cosmic rays induced the 6.4 keV line. ASTRO-H would open a new chapter of the study of LECRs as well as the GDXE study.

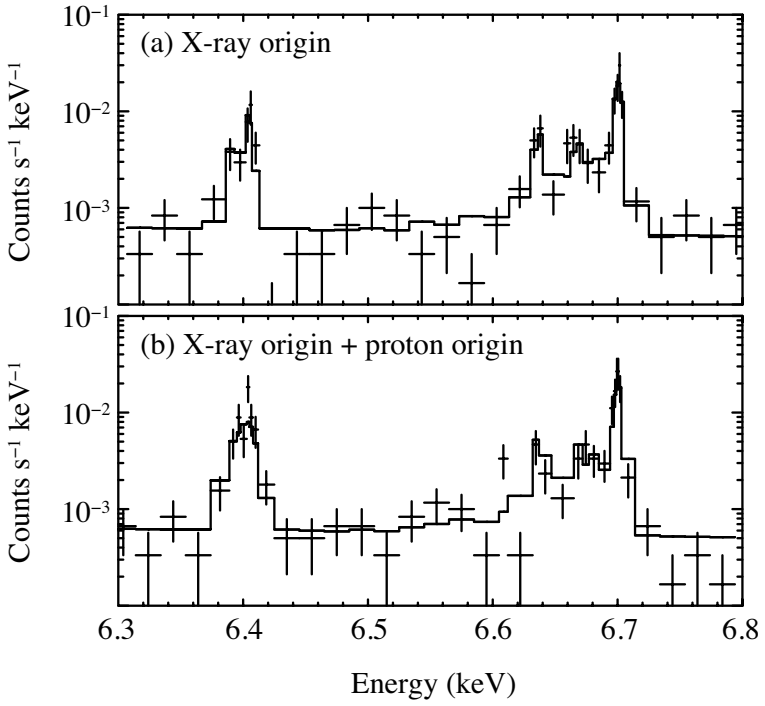

Figure 8.1. Simulation of an SXS/ASTRO-H observation in the GC east region with the exposure time of 300 ksec. (a) In the case that all the 6.4 keV line originates from X-ray reflection. (b) In the case that a half of the 6.4 keV line emission originates from X-ray reflection and the rest are due to proton bombardment.

Table 8.1. Simulation result of an SXS/ASTRO-H in the GC east region with the exposure time of 300 ksec (figure 8.1)*.

Origin	Line width of neutral iron Kα_1 and Kα_2
X-ray	< 2 eV
X-rays+Protons	5±2 eV

* Errors are quoted at 68% confidence level.

Chapter 9

Conclusion

We compiled the Suzaku observation data of the Galactic plane in order to measure spatial distributions and equivalent widths of the 6.4 keV line, and for the comparison, the 6.7 keV and 7.0 keV lines and 5–8 keV continuum emission in the GDXE. A summary of this dissertation is as follows:

- The latitudinal distribution of each line of the GDXE demonstrates that the GDXE consists of the three components: the GCXE, GBXE, and GRXE.
- We discover the enhancements of the 6.4 keV line emission relative to the 6.7 keV line in the two regions: (1) the GC east ($1.^\circ5 < l < 3.^\circ5$) and (2) $l = -20^\circ$. Both the enhancements are associated with molecular clouds. The most plausible irradiating particles are LECR protons in the GC east. Also the $l = -20^\circ$ region favors the LECR scenario although whether the irradiating particles are protons or electrons cannot be constrained.
- The scale height and equivalent width of the 6.4 keV line emission in the GRXE indicate that at least a half of the 6.4 keV line emission originates from molecular clouds irradiated by X-rays or cosmic-ray particles. Since the 6.4 keV line due to the X-ray irradiation from the LMXB contributes only 10% of the total 6.4 keV line emission in the GRXE, the most possible origin is cosmic-ray bombardment.
- The energy density of LECR protons in the GC east would be ~ 80 eV cm^{-3} while those in the $l = -20^\circ$ region would be ~ 20 eV cm^{-3} and ~ 0.03 eV cm^{-3} for the proton and electron cases, respectively. In the case that a half of the 6.4 keV line emission in the GRXE originates from the cosmic-ray bombardment, the energy densities of LECRs along the Galactic plane would be $\sim$10 eV cm^{-3} and $\sim$0.01 eV cm^{-3} for protons and electrons, respectively.
- Since the diffuse length of LECRs is only a few tens of parsecs, they should be produced *in situ*. There is neither SNRs nor pulsar wind nebulae in the vicinity of the GC east, $l = -20^\circ$, and the entire GRXE region. The cosmic rays in the two enhancement regions can be energized by stochastic acceleration or magnetic reconnection. The magnetic reconnection may produce the LECR protons in the entire GRXE region. In the electron scenario, they could be the second particles that are produced via interaction of high-energy cosmic rays and the ISM.
- The scale heights and equivalent widths of the iron K-shell lines in the GBXE indicate that the majority of the iron lines is due to point sources although non-magnetic CVs should contribute

much more than previous study discussed.

- The scale heights and equivalent widths of the iron K-shell lines in the GCXE shows that the majority of the iron lines cannot be explained by point sources.

References

[1] T. Ak, S. Bilir, S. Ak, and Z. Eker. 2008, *New Astronomy*, **13**, 3, 133–143.

[2] T. Amano, K. Torii, T. Hayakawa, and Y. Fukui. 2011, *Publications of the Astronomical Society of Japan*, **63**, 6, L63–L66.

[3] B. Aschenbach, U. G. Briel, F. Haberl, H. W. Braeuninger, W. Burkert, A. Oppitz, P. Gondoin, and D. H. Lumb. 2000, *Proc. SPIE Vol. 4012*, **4012**, 731–739.

[4] F. K. Baganoff, *et al.*, 2003, *Astrophysical Journal*, **591**, 2, 891–915.

[5] T. M. Bania. 1977, *Astrophysical Journal*, **216**, 381–403.

[6] M. G. Baring, F. C. Jones, and D. C. Ellison. 2000, *Astrophysical Journal*, **528**, 2, 776–788.

[7] M. W. Bautz, S. E. Kissel, G. Y. Prigozhin, B. LaMarr, B. E. Burke, and J. A. Gregory. 2004, *High-Energy Detectors in Astronomy. Edited by Holland*, **5501**, 111–122.

[8] M. J. Church, G. S. Halai, and M. Bałucińska-Church. 2006, *Astronomy and Astrophysics*, **460**, 1, 233–244.

[9] E. Churchwell, *et al.*, 2009, *Publications of the Astronomical Society of the Pacific*, **121**, 877, 213–230.

[10] K. Cunha, K. Sellgren, V. V. Smith, S. V. Ramirez, R. D. Blum, and D. M. Terndrup. 2007, *Astrophysical Journal*, **669**, 2, 1011–1023.

[11] T. M. Dame, D. Hartmann, and P. Thaddeus. 2001, *Astrophysical Journal*, **547**, 2, 792–813.

[12] T. M. Dame and P. Thaddeus. 2008, *Astrophysical Journal Letters*, **683**, 2, L143–L146.

[13] R. C. Dempsey, J. L. Linsky, T. A. Fleming, and J. H. M. M. Schmitt. 1993, *Astrophysical Journal Supplement Series*, **86**, 599–609.

[14] R. C. Dempsey, J. L. Linsky, T. A. Fleming, and J. H. M. M. Schmitt. 1997, *The Astrophysical Journal*, **478**, 1, 358–366.

[15] V. A. Dogiel, D. O. Chernyshov, V. Tatischeff, K. S. Cheng, and R. Terrier. 2013, *The Astrophysical Journal Letters*, **771**, 2, L43.

[16] V. Dogiel, D. Chernyshov, K. Koyama, M. Nobukawa, and K.-S. Cheng. 2011, *Publications of the Astronomical Society of Japan*, **63**, 3, 535–541.

[17] K. Ebisawa, Y. Maeda, H. Kaneda, and S. Yamauchi. 2001, *Science*, **293**, 5535, 1633–1635.

[18] K. Ebisawa, *et al.*, 2005, *The Astrophysical Journal*, **635**, 1, 214–242.

[19] K. Ebisawa, S. Yamauchi, Y. Tanaka, K. Koyama, Y. Ezoe, A. Bamba, M. Kokubun, Y. Hyodo, M. Tsujimoto, and H. Takahashi. 2008, *Publications of the Astronomical Society of Japan*, **60**, S223–S230.

[20] H. Ezuka and M. Ishida. 1999, *The Astrophysical Journal Supplement Series*, **120**, 2, 277–298.

[21] M. Fich, L. Blitz, and A. A. Stark. 1989, *Astrophysical Journal*, **342**, 272–284.

[22] Y. Fukui, *et al.*, 2006, *Science*, **314**, 106–109.

[23] J. D. Garcia, R. J. Fortner, and T. M. Kavanagh. 1973, *Review of Modern Physics*, **45**, 2, 111–177.

[24] R. Genzel, C. Pichon, A. Eckart, O. E. Gerhard, and T. Ott. 2000, *Monthly Notices of the Royal Astronomical Society*, **317**, 2, 348–374.

[25] A. M. Ghez, M. Morris, E. E. Becklin, A. Tanner, and T. Kremenek. 2000, *Nature*, **407**, 6, 349–351.

[26] A. M. Ghez, *et al.*, 2008, *The Astrophysical Journal*, **689**, 2, 1044–1062.

[27] U. Giveon, A. Sternberg, D. Lutz, H. Feuchtgruber, and A. W. A. Pauldrach. 2002, *The Astrophysical Journal*, **566**, 2, 880–897.

[28] H. J. Grimm, M. Gilfanov, and R. Sunyaev. 2002, *Astronomy and Astrophysics*, **391**, 3, 923–944.

[29] C. Hellier, K. Mukai, and J. P. Osborne. 1998, *Monthly Notices of the Royal Astronomical Society*, **297**, 2, 526–530.

[30] C. Hellier and K. Mukai. 2004, *Monthly Notices of the Royal Astronomical Society*, **352**, 3, 1037–1040.

[31] Institute of Space and Astronautical Science (ISAS/JAXA) and X-ray Astrophysics Laboratory NASA/Goddard Space Flight Center. 2015, The Suzaku Technical Description, Ver. January, 2015.

[32] T. Inui, K. Koyama, H. Matsumoto, and T. G. Tsuru. 2009, *Publications of the Astronomical Society of Japan*, **61**, sp1, S241–S253.

[33] Y. Ishisaki, *et al.*, 2007, *Publications of the Astronomical Society of Japan*, **59**, sp1, S113–S132.

[34] J. S. Kaastra and R. Mewe. 1993, *Astronomy and Astrophysics Supplement Series*, **97**, 443–482.

[35] H. Kaneda, K. Makishima, S. Yamauchi, K. Koyama, K. Matsuzaki, and N. Y. Yamasaki. 1997, *The Astrophysical Journal*, **491**, 2, 638–652.

[36] R. L. Kelley, *et al.*, 2007, *Publications of the Astronomical Society of Japan*, **59**, sp1, 77–112.

[37] J. Kerp, H. Lesch, and K. H. Mack. 1994, *Astronomy and Astrophysics*, **286**, L13–L16.

[38] M. Kokubun, *et al.*, 2007, *Publications of the Astronomical Society of Japan*, **59**, sp1, S53–S76.

[39] K. Koyama, S. Ikeuchi, and K. Tomisaka. 1986a, *Publications of the Astronomical Society of Japan*, **38**, 4, 503–509.

[40] K. Koyama, K. Makishima, Y. Tanaka, and H. Tsunemi. 1986b, *Publications of the Astronomical Society of Japan*, **38**, 1, 121–131.

[41] K. Koyama, H. Awaki, H. Kunieda, S. Takano, and Y. Tawara. 1989, *Nature*, **339**, 6226, 603–605.

[42] K. Koyama, Y. Maeda, T. Sonobe, T. Takeshima, Y. Tanaka, and S. Yamauchi. 1996, *Publications of the Astronomical Society of Japan*, **48**, 2, 249–255.

[43] K. Koyama, *et al.*, 2007, *Publications of the Astronomical Society of Japan*, **59**, sp1, S23–S33.

[44] A. Kushino, Y. Ishisaki, U. Morita, N. Y. Yamasaki, M. Ishida, T. Ohashi, and Y. Ueda. 2002, *Publications of the Astronomical Society of Japan*, **54**, 3, 327–352.

[45] B. LaMarr, M. W. Bautz, S. E. Kissel, G. Y. Prigozhin, K. Hayashida, T. G. Tsuru, and H. Matsumoto. 2004, *High-Energy Detectors in Astronomy. Edited by Holland*, **5501**, 385–391.

[46] R. Launhardt, R. Zylka, and P. G. Mezger. 2002, *Astronomy and Astrophysics*, **384**, 1, 112–139.

[47] H. Lesch and W. Reich. 1992, *Astronomy and Astrophysics*, **264**, 2, 493–499.

[48] R. P. Martin, S. M. Andrievsky, V. V. Kovtyukh, S. A. Korotin, I. A. Yegorova, and I. Saviane. 2015, *Monthly Notices of the Royal Astronomical Society*, **449**, 4, 4071–4078.

[49] K. Masai, V. A. Dogiel, H. Inoue, V. Schönfelder, and A. W. Strong. 2002, *The Astrophysical Journal*, **581**, 2, 1071–1079.

[50] H. Matsumoto, *et al.*, 2006, *Space Telescopes and Instrumentation II: Ultraviolet to Gamma Ray. Edited by Turner*, **6266**, 120–626641–8.

[51] P. A. McGale, J. P. Pye, and S. T. Hodgkin. 1996, *Monthly Notices of the Royal Astronomical Society*, **280**, 627–637.

[52] K. Mitsuda, *et al.*, 2007, *Publications of the Astronomical Society of Japan*, **59**, sp1, S1–S7.

[53] M. Molaro, R. Khatri, and R. A. Sunyaev. 2014, *Astronomy and Astrophysics*, **564**, A107.

[54] H. Mori, *et al.*, 2005, *Publications of the Astronomical Society of Japan*, **57**, 1, 245–257.

[55] M. Morris and E. Serabyn. 1996, *Annual Review of Astronomy and Astrophysics*, **34**, 1, 645–702.

[56] M. P. Muno, F. K. Baganoff, M. W. Bautz, E. D. Feigelson, G. P. Garmire, M. R. Morris, S. Park, G. R. Ricker, and L. K. Townsley. 2004, *The Astrophysical Journal*, **613**, 1, 326–342.

[57] M. P. Muno, F. E. Bauer, R. M. Bandyopadhyay, and Q. D. Wang. 2006, *The Astrophysical Journal Supplement Series*, **165**, 1, 173–187.

[58] H. Murakami, K. Koyama, M. Sakano, M. Tsujimoto, and Y. Maeda. 2000, *Astrophysical Journal*, **534**, 1, 283–290.

[59] H. Murakami, K. Koyama, M. Tsujimoto, Y. Maeda, and M. Sakano. 2001a, *The Astrophysical Journal*, **550**, 1, 297–300.

[60] H. Murakami, K. Koyama, and Y. Maeda. 2001b, *The Astrophysical Journal*, **558**, 2, 687–692.

[61] H. Nakajima, *et al.*, 2008, *Publications of the Astronomical Society of Japan*, **60**, S1–S9.

[62] H. Nakanishi and Y. Sofue. 2003, *Publications of the Astronomical Society of Japan*, **55**, 1, 191–202.

[63] S. Nakashima, M. Nobukawa, H. Uchida, T. Tanaka, T. G. Tsuru, K. Koyama, H. Murakami, and H. Uchiyama. 2013, *The Astrophysical Journal*, **773**, 1, 20.

[64] A. Neronov, D. V. Semikoz, and A. M. Taylor. 2012, *Physical Review Letters*, **108**, 5, 051105.

[65] S. Nishiyama, *et al.*, 2013, *The Astrophysical Journal Letters*, **769**, 2, L28.

[66] K. K. Nobukawa, M. Nobukawa, H. Uchiyama, T. G. Tsuru, K. Torii, T. Tanaka, D. O. Chernyshov, Y. Fukui, V. A. Dogiel, and K. Koyama. 2015a, *The Astrophysical Journal Letters*, **807**, 1, L10.

[67] K. K. Nobukawa, M. Nobukawa, T. G. Tsuru, and K. Koyama. 2015b, *Advances in Space Research*, **55**, 1, 2493–2499.

[68] M. Nobukawa. 2011, Ph.D. dissertation, Kyoto University.

[69] M. Nobukawa, S. G. Ryu, T. G. Tsuru, and K. Koyama. 2011, *The Astrophysical Journal Letters*, **739**, 2, L52.

[70] M. Nobukawa, K. Koyama, T. G. Tsuru, S. G. Ryu, and V. Tatischeff. 2010, *Publications of the Astronomical Society of Japan*, **62**, 2, 423–429.

[71] J. H. Oort, F. J. Kerr, and G. Westerhout. 1958, *Monthly Notices of the Royal Astronomical Society*, **118**, 379–389.

[72] Y. Osaki. 1974, *Astronomical Society of Japan*, **26**, 429–436.

[73] M. Ozawa, *et al.*, 2009, *Publications of the Astronomical Society of Japan*, **61**, sp1, S1–S7.

[74] J. Patterson. 1984, *The Astrophysical Journal Supplement Series*, **54**, 443–493.

[75] H. Paul and J. Sacher. 1989, *Atomic Data and Nuclear Data Tables*, **42**, 1, 105–156.

[76] S. Piraino, A. Santangelo, P. Kaaret, B. Mück, A. D'Aì, T. Di Salvo, R. Iaria, N. Robba, L. Burderi, and E. Egron. 2012, *Astronomy and Astrophysics*, **542**, L27.

[77] G. Ponti, R. Terrier, A. Goldwurm, G. Belanger, and G. Trap. 2010, *The Astrophysical Journal*, **714**, 1, 732–747.

[78] G. Y. Prigozhin, S. E. Kissel, M. W. Bautz, C. Grant, B. LaMarr, R. F. Foster, and G. R. Ricker. 2000, *Proc. SPIE Vol. 4140*, **4140**, 123–134.

[79] M. Revnivtsev. 2003, *Astronomy and Astrophysics*, **410**, 865–870.

[80] M. Revnivtsev, S. Sazonov, M. Gilfanov, E. Churazov, and R. Sunyaev. 2006a, *Astronomy and Astrophysics*, **452**, 1, 169–178.

[81] M. Revnivtsev, S. Molkov, and S. Sazonov. 2006b, *Monthly Notices of the Royal Astronomical Society: Letters*, **373**, 1, L11–L15.

[82] M. Revnivtsev, S. Sazonov, R. Krivonos, H. Ritter, and R. Sunyaev. 2008, *Astronomy and Astrophysics*, **489**, 3, 1121–1127.

[83] M. Revnivtsev, S. Sazonov, E. Churazov, and W. Forman. 2009, *Nature*, **458**, 7242, 1142–1144.

[84] M. G. Revnivtsev, E. M. Churazov, S. Y. Sazonov, R. A. Sunyaev, A. A. Lutovinov, M. R. Gilfanov, A. A. Vikhlinin, P. E. Shtykovsky, and M. N. Pavlinsky. 2004, *Astronomy and Astrophysics*, **425**, 3, L49–L52.

[85] M. G. Revnivtsev and S. V. Molkov. 2012, *Monthly Notices of the Royal Astronomical Society*, **424**, 3, 2330–2338.

[86] S. Sazonov, M. Revnivtsev, M. Gilfanov, E. Churazov, and R. Sunyaev. 2006, *Astronomy and Astrophysics*, **450**, 1, 117–128.

[87] E. Seifina, L. Titarchuk, and N. Shaposhnikov. 2014, *The Astrophysical Journal*, **789**, 1, 57.

[88] P. J. Serlemitsos, *et al.*, 2007, *Publications of the Astronomical Society of Japan*, **59**, sp1, 9–21.

[89] P. J. Serlemitsos and Y. Soong. 1996, *Astrophysics and Space Science*, **239**, 2, 177–196.

[90] R. K. Smith, N. S. Brickhouse, D. A. Liedahl, and J. C. Raymond. 2001, *The Astrophysical Journal*, **556**, 2, L91–L95.

[91] E. C. Stone, A. C. Cummings, F. B. McDonald, B. C. Heikkila, N. Lal, and W. R. Webber. 2013, *Science*, **341**, 6142, 150–153.

[92] K. G. Strassmeier, D. S. Hall, F. C. Fekel, and M. Scheck. 1993, *Astronomy and Astrophysics Supplement Series*, **100**, 173–225.

[93] M. Su, T. R. Slatyer, and D. P. Finkbeiner. 2010, *Astrophysical Journal*, **724**, 2, 1044–1082.

[94] R. A. Sunyaev, M. Markevitch, and M. PAVLINSKY. 1993, *Astrophysical Journal*, **407**, 2, 606–610.

[95] T. Takahashi, *et al.*, 2007, *Publications of the Astronomical Society of Japan*, **59**, 35–51.

[96] T. Takahashi, *et al.*, 2014, in *Proceedings of the SPIE*, 914425, Institute of Space and Astronautical Science, Japan Aerospace Exploration Agency (Japan).

[97] A. Takata, M. Nobukawa, H. Uchida, T. G. Tsuru, T. Tanaka, and K. Koyama. 2015, *Publications of the Astronomical Society of Japan*.

[98] S. Tanuma, T. Yokoyama, T. Kudoh, R. Matsumoto, K. Shibata, and K. Makishima. 1999, *Publications of the Astronomical Society of Japan*, **51**, 1, 161–172.

[99] V. Tatischeff, A. Decourchelle, and G. Maurin. 2012, *Astronomy and Astrophysics*, **546**, A88.

[100] N. Tawa, *et al.*, 2008, *Publications of the Astronomical Society of Japan*, **60**, S11–S24.

[101] K. Torii, *et al.*, 2010, *Publications of the Astronomical Society of Japan*, **62**, 5, 1307–1332.

[102] M. Tsuboi, T. Handa, and N. Ukita. 1999, *The Astrophysical Journal Supplement Series*, **120**, 1, 1–39.

[103] M. Tsujimoto, Y. Hyodo, and K. Koyama. 2007, *Publications of the Astronomical Society of Japan*, **59**, sp1, S229–S235.

[104] T. G. Tsuru, H. Uchiyama, K. K. Nobukawa, M. Nobukawa, S. Nakashima, K. Koyama, K. Torii, and Y. Fukui. 2014, *Suzaku-MAXI 2014: Expanding the Frontiers of the X-ray Universe*.

[105] H. Uchiyama, *et al.*, 2009, *Publications of the Astronomical Society of Japan*, **61**, sp1, S9–S15.

[106] H. Uchiyama, M. Nobukawa, T. Tsuru, K. Koyama, and H. Matsumoto. 2011, *Publications of the Astronomical Society of Japan*, **63**, sp3, 903–S911.

[107] H. Uchiyama, M. Nobukawa, T. G. Tsuru, and K. Koyama. 2013, *Publications of the Astronomical Society of Japan*, **65**, 19.

[108] Y. Ueda, M. Akiyama, K. Ohta, and T. Miyaji. 2003, *The Astrophysical Journal*, **598**, 2, 886–908.

[109] A. Valinia, V. Tatischeff, K. Arnaud, K. Ebisawa, and R. Ramaty. 2000, *The Astrophysical Journal*, **543**, 2, 733–739.

[110] A. Valinia and F. E. Marshall. 1998, *The Astrophysical Journal*, **505**, 1, 134–147.

[111] H. Van Woerden and G. W. Rougoor. 1957, *Comptes Rendus l'Academie des Sciences*, **244**, 1691–1695.

[112] R. S. Warwick. 2014, *Monthly Notices of the Royal Astronomical Society*, **445**, 1, 66–80.

[113] R. S. Warwick, M. J. L. Turner, M. G. Watson, and R. Willingale. 1985, *Nature*, **317**, 6034, 218–221.

[114] R. S. Warwick, K. Byckling, and D. Pérez-Ramírez. 2014, *Monthly Notices of the Royal Astronomical Society*, **438**, 4, 2967–2979.

[115] M. C. Weisskopf, B. Brinkman, C. Canizares, G. Garmire, S. Murray, and L. P. Van Speybroeck. 2002, *The Publications of the Astronomical Society of the Pacific*, **114**, 7, 1–24.

[116] D. M. Worrall, F. E. Marshall, E. A. Boldt, and J. H. Swank. 1982, *Astrophysical Journal*, **255**, 111–121.

[117] N. Y. Yamasaki, *et al.*, 1997, *The Astrophysical Journal*, **481**, 2, 821–831.

[118] S. Yamauchi, M. Kawada, K. Koyama, H. Kunieda, and Y. Tawara. 1990, *Astrophysical Journal*, **365**, 532–538.

[119] S. Yamauchi, H. Kaneda, K. Koyama, K. Makishima, K. Matsuzaki, T. Sonobe, Y. Tanaka, and N. Yamasaki. 1996, *Publications of the Astronomical Society of Japan*, **48**, 2, L15–L20.

[120] S. Yamauchi, K. Ebisawa, Y. Tanaka, K. Koyama, H. Matsumoto, N. Y. Yamasaki, H. Takahashi, and Y. Ezoe. 2009, *Publications of the Astronomical Society of Japan*, **61**, sp1, 225–S232.

[121] S. Yamauchi and K. Koyama. 1993, *Astrophysical Journal*, **404**, 620–624.

[122] K. Yasui, *et al.*, 2015, *Publications of the Astronomical Society of Japan*, **67**, 6, 123.

[123] M. Yasumi, M. Nobukawa, S. Nakashima, H. Uchida, R. Sugawara, T. G. Tsuru, T. Tanaka, and K. Koyama. 2014, *Publications of the Astronomical Society of Japan*, **66**, 4, 68.

[124] T. Yokoyama, S. Tanuma, T. Kudoh, and K. Shibata. 2000, *Advances in Space Research*, **25**, 3–4, 505–508

[125] T. Yuasa, K. Makishima, and K. Nakazawa. 2012, *The Astrophysical Journal*, **753**, 2, 129.

[126] Y. Yusef-Zadeh, C. Law, and M. Wardle. 2002, *Astrophysical Journal*, **568**, 2, L121–L125.

Appendix:
X-ray image and selected region

We show the X-ray images in the energy band of 2–8 keV with the FOVs of the XIS (squares) and excluded regions (those with a red diagonal).

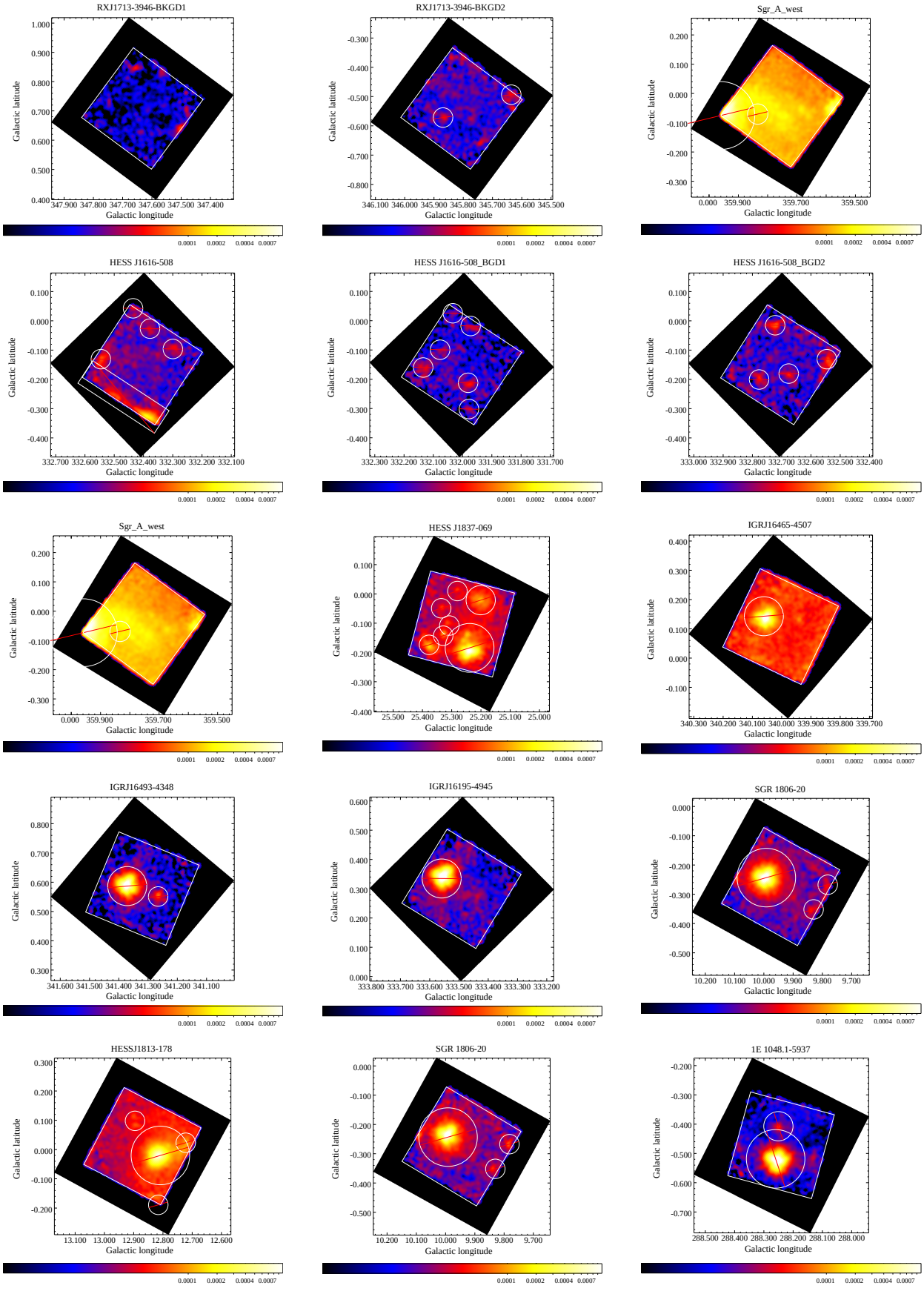
RXJ1713-3946-BKGD1
RXJ1713-3946-BKGD2
Sgr_A_west
HESS J1616-508
HESS J1616-508_BGD1
HESS J1616-508_BGD2
Sgr_A_west
HESS J1837-069
IGRJ16465-4507
IGRJ16493-4348
IGRJ16195-4945
SGR 1806-20
HESSJ1813-178
SGR 1806-20
1E 1048.1-5937
Galactic latitude
Galactic longitude
0.0001 0.0002 0.0004 0.0007

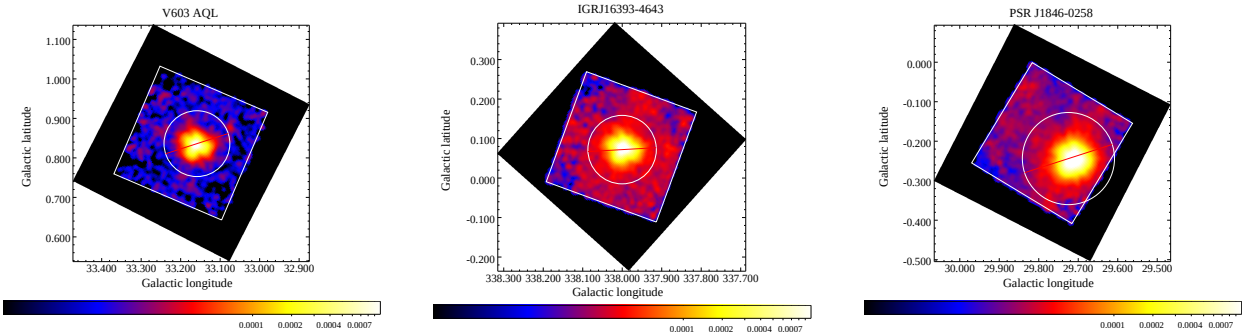
V603 AQL
IGRJ16393-4643
PSR J1846-0258
Galactic latitude
Galactic longitude
0.0001 0.0002 0.0004 0.0007

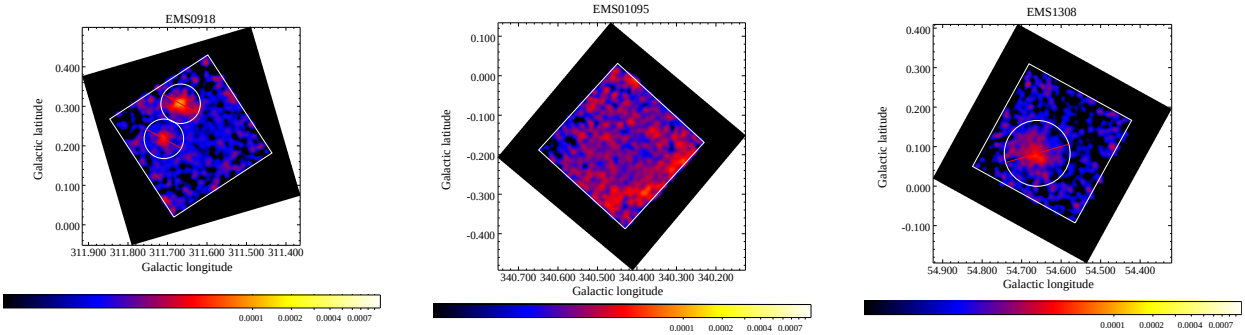
EMS0918
EMS01095
EMS1308
Galactic latitude
Galactic longitude
0.0001 0.0002 0.0004 0.0007

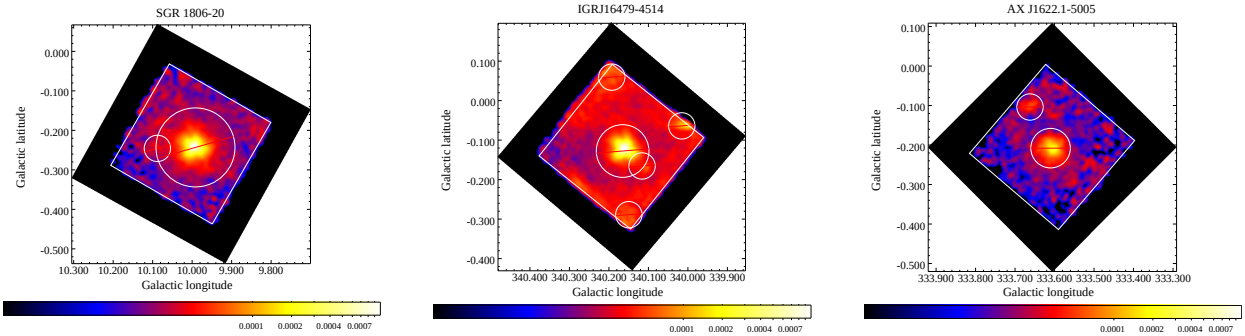
SGR 1806-20
IGRJ16479-4514
AX J1622.1-5005
Galactic latitude
Galactic longitude
0.0001 0.0002 0.0004 0.0007

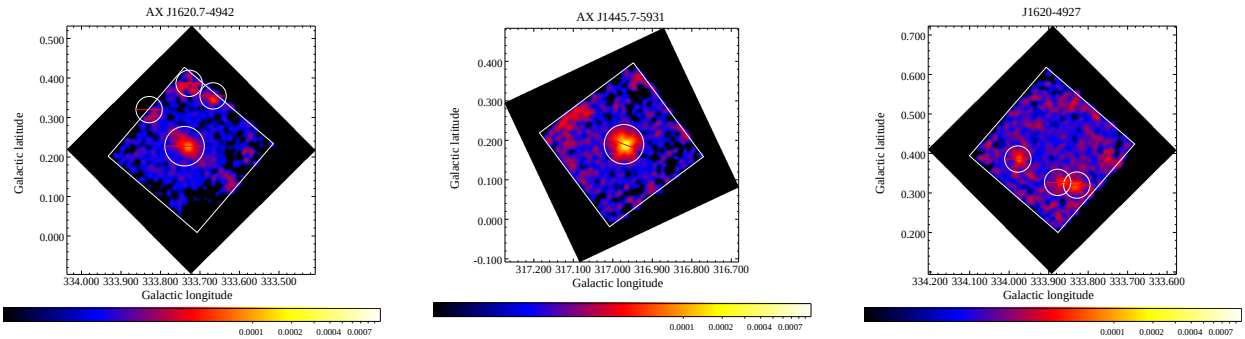
AX J1620.7-4942
AX J1445.7-5931
J1620-4927
Galactic latitude
Galactic longitude
0.0001 0.0002 0.0004 0.0007

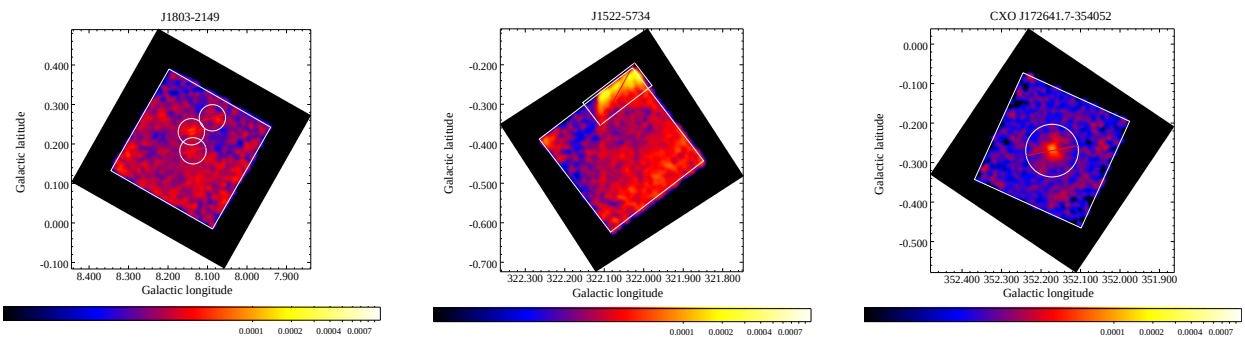
J1803-2149
J1522-5734
CXO J172641.7-354052
Galactic latitude
Galactic longitude
0.0001 0.0002 0.0004 0.0007

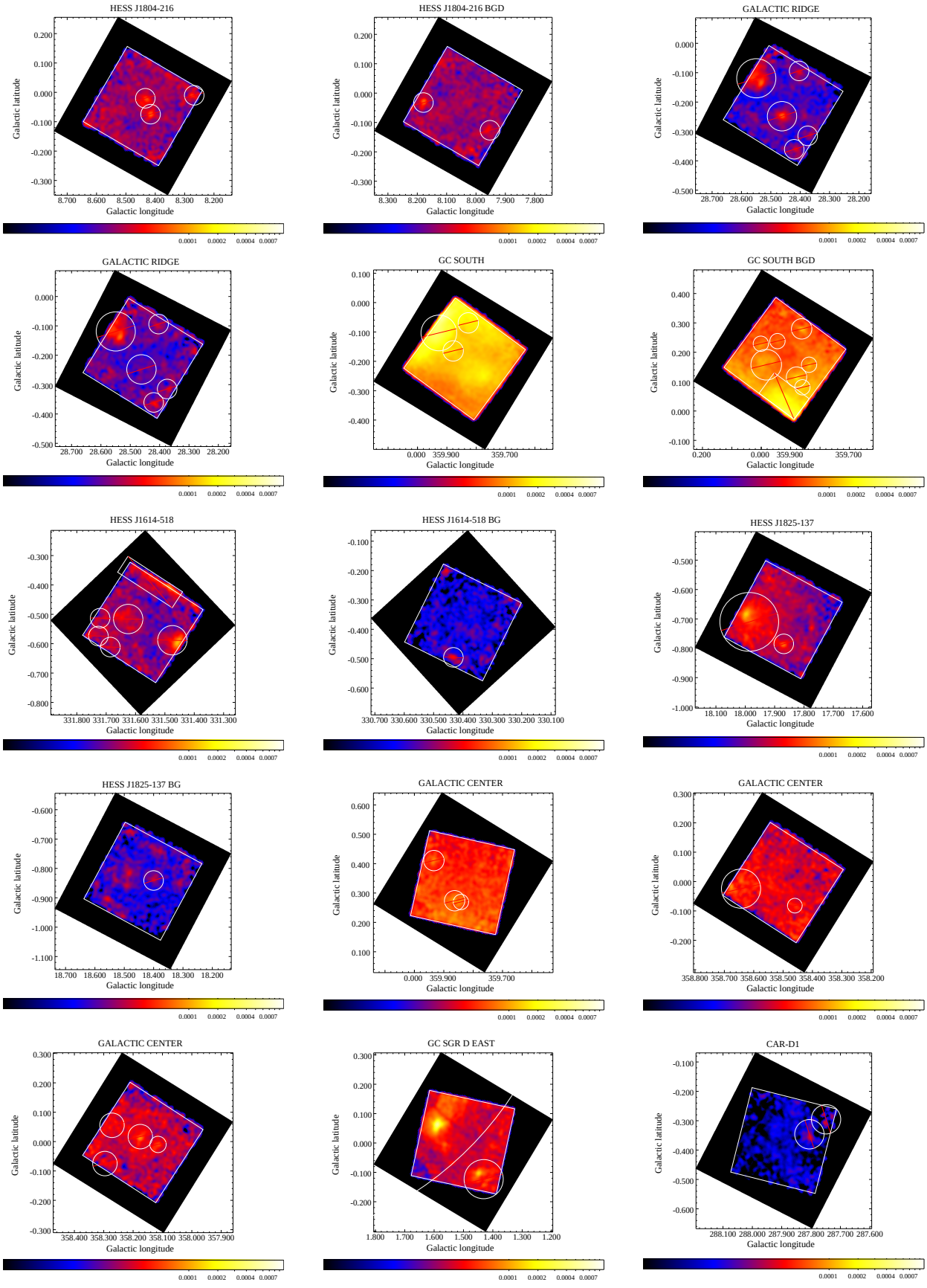
HESS J1804-216
HESS J1804-216 BGD
GALACTIC RIDGE
GALACTIC RIDGE
GC SOUTH
GC SOUTH BGD
HESS J1614-518
HESS J1614-518 BG
HESS J1825-137
HESS J1825-137 BG
GALACTIC CENTER
GALACTIC CENTER
GALACTIC CENTER
GC SGR D EAST
CAR-D1
Galactic latitude
Galactic longitude
0.0001 0.0002 0.0004 0.0007

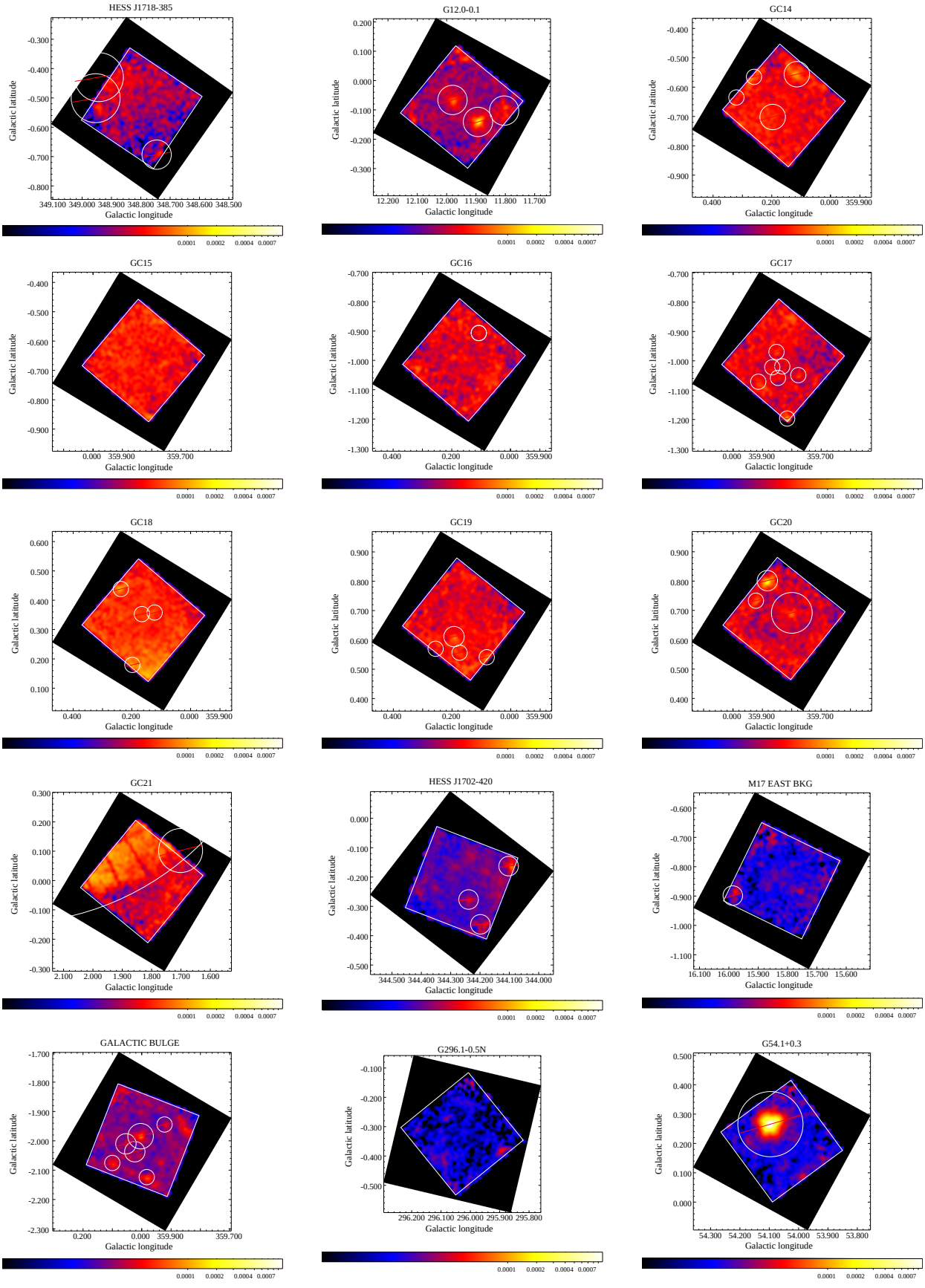
HESS J1718-385
G12.0-0.1
GC14
GC15
GC16
GC17
GC18
GC19
GC20
GC21
HESS J1702-420
M17 EAST BKG
GALACTIC BULGE
G296.1-0.5N
G54.1+0.3
Galactic latitude
Galactic longitude
0.0001 0.0002 0.0004 0.0007

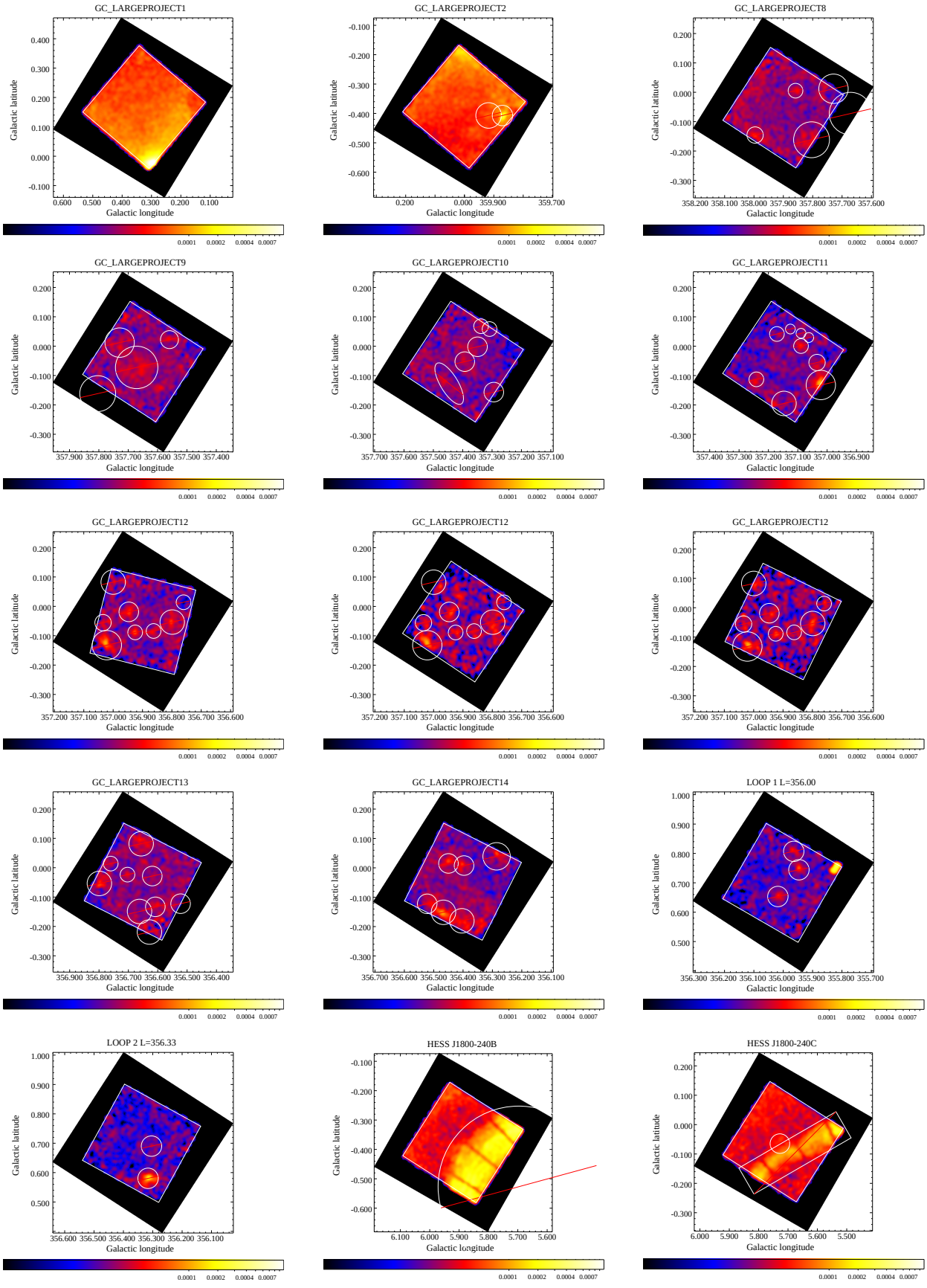
GC_LARGEPROJECT1
GC_LARGEPROJECT2
GC_LARGEPROJECT8
GC_LARGEPROJECT9
GC_LARGEPROJECT10
GC_LARGEPROJECT11
GC_LARGEPROJECT12
GC_LARGEPROJECT12
GC_LARGEPROJECT12
GC_LARGEPROJECT13
GC_LARGEPROJECT14
LOOP 1 L=356.00
LOOP 2 L=356.33
HESS J1800-240B
HESS J1800-240C
Galactic latitude
Galactic longitude
0.0001 0.0002 0.0004 0.0007

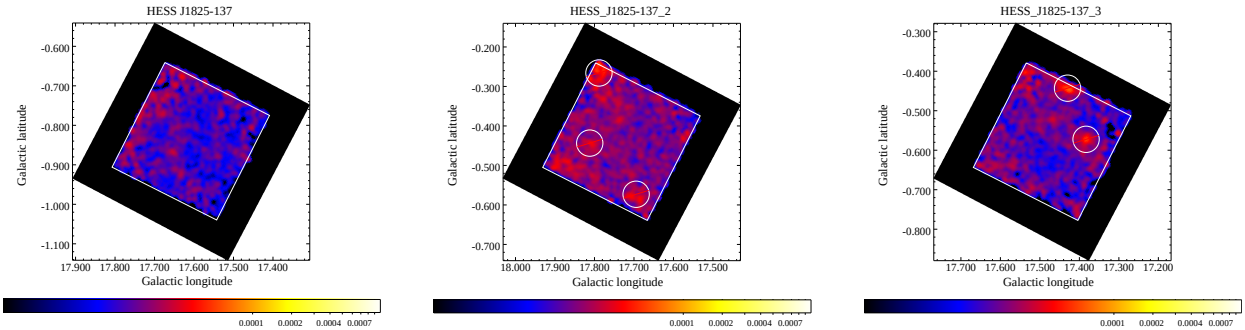
HESS J1825-137
Galactic latitude
Galactic longitude
HESS_J1825-137_2
Galactic latitude
Galactic longitude
HESS_J1825-137_3
Galactic latitude
Galactic longitude

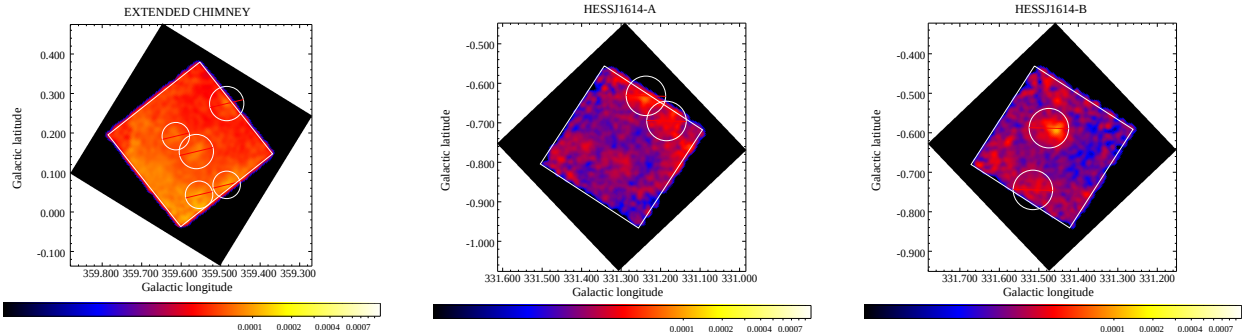
EXTENDED CHIMNEY
Galactic latitude
Galactic longitude
HESSJ1614-A
Galactic latitude
Galactic longitude
HESSJ1614-B
Galactic latitude
Galactic longitude

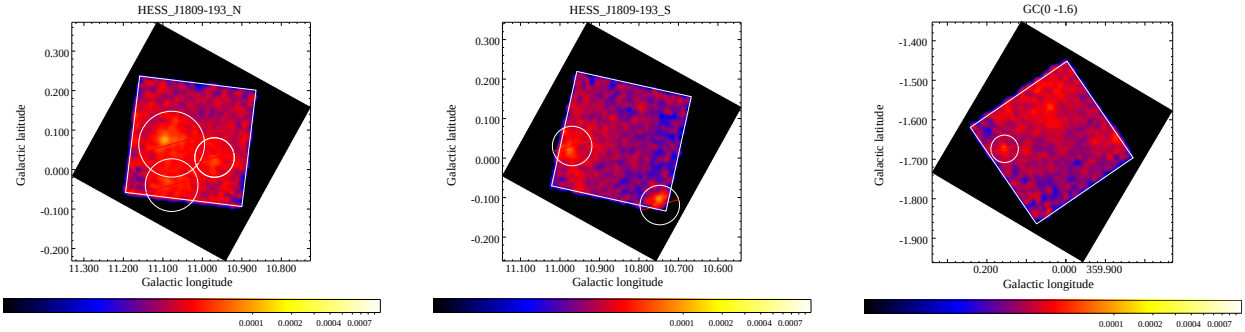
HESS_J1809-193_N
Galactic latitude
Galactic longitude
HESS_J1809-193_S
Galactic latitude
Galactic longitude
GC(0 -1.6)
Galactic latitude
Galactic longitude

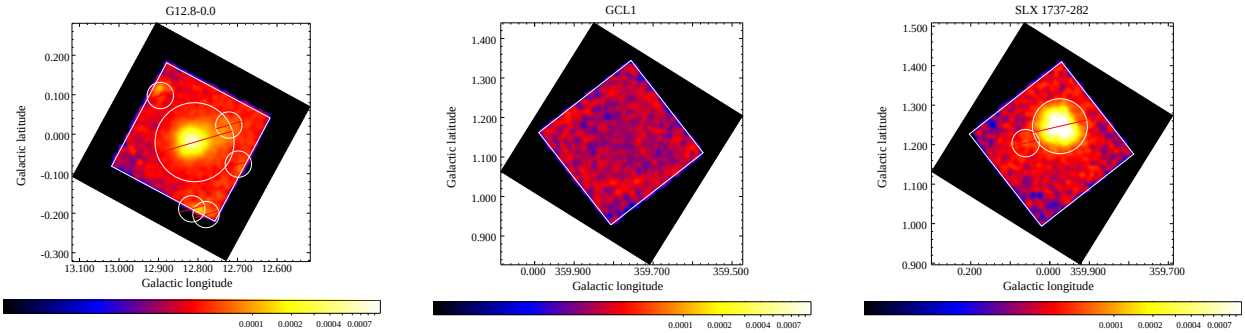
G12.8-0.0
Galactic latitude
Galactic longitude
GCL1
Galactic latitude
Galactic longitude
SLX 1737-282
Galactic latitude
Galactic longitude

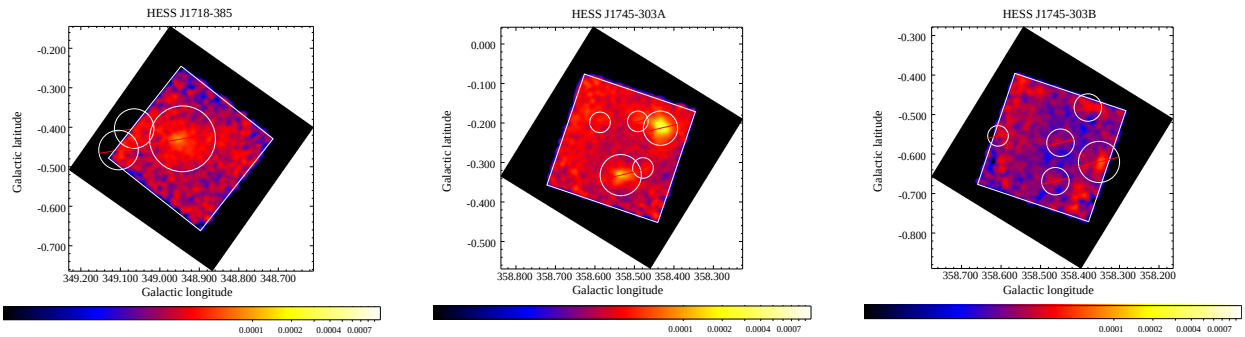
HESS J1718-385
Galactic latitude
Galactic longitude
HESS J1745-303A
Galactic latitude
Galactic longitude
HESS J1745-303B
Galactic latitude
Galactic longitude

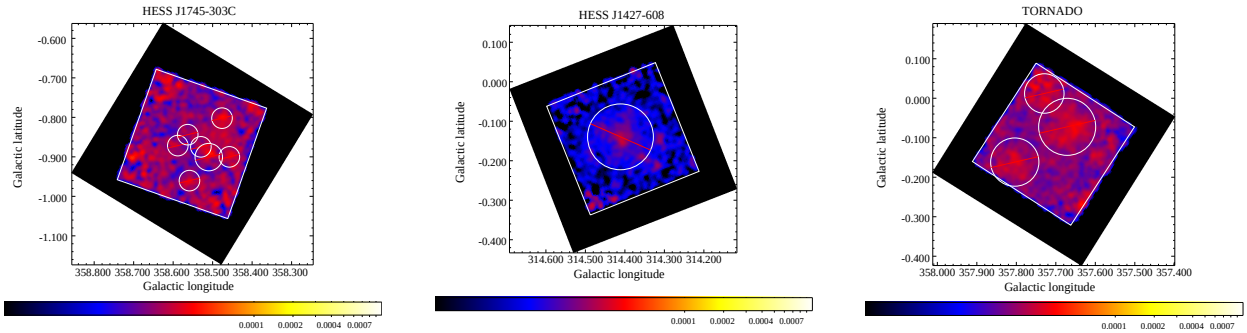
HESS J1745-303C
Galactic latitude
-0.600 -0.700 -0.800 -0.900 -1.000 -1.100
358.800 358.700 358.600 358.500 358.400 358.300
Galactic longitude
0.0001 0.0002 0.0004 0.0007
HESS J1427-608
Galactic latitude
0.100 0.000 -0.100 -0.200 -0.300 -0.400
314.600 314.500 314.400 314.300 314.200
Galactic longitude
0.0001 0.0002 0.0004 0.0007
TORNADO
Galactic latitude
0.100 0.000 -0.100 -0.200 -0.300 -0.400
358.000 357.900 357.800 357.700 357.600 357.500 357.400
Galactic longitude
0.0001 0.0002 0.0004 0.0007
ASO0431
Galactic latitude
-0.600 -0.700 -0.800 -0.900 -1.000 -1.100
40.400 40.300 40.200 40.100 40.000 39.900
Galactic longitude
0.0001 0.0002 0.0004 0.0007
ASO0449
Galactic latitude
-0.100 -0.200 -0.300 -0.400 -0.500 -0.600
66.100 66.000 65.900 65.800 65.700 65.600
Galactic longitude
0.0001 0.0002 0.0004 0.0007
ASO0218
Galactic latitude
-0.200 -0.300 -0.400 -0.500 -0.600 -0.700
285.300 285.200 285.100 285.000 284.900 284.800
Galactic longitude
0.0001 0.0002 0.0004 0.0007
ASO0447
Galactic latitude
0.700 0.600 0.500 0.400 0.300 0.200
65.500 65.400 65.300 65.200 65.100 65.000
Galactic longitude
0.0001 0.0002 0.0004 0.0007
ASO0376
Galactic latitude
1.300 1.200 1.100 1.000 0.900 0.800 0.700
356.500 356.400 356.300 356.200 356.100 356.000
Galactic longitude
0.0001 0.0002 0.0004 0.0007
NONE
Galactic latitude
-1.200 -1.300 -1.400 -1.500 -1.600 -1.700
0.400 0.200 0.000 359.900
Galactic longitude
0.0001 0.0002 0.0004 0.0007
ASO0418
Galactic latitude
0.400 0.300 0.200 0.100 0.000 -0.100
26.700 26.600 26.500 26.400 26.300 26.200
Galactic longitude
0.0001 0.0002 0.0004 0.0007
HESS J1809-193A
Galactic latitude
0.000 -0.100 -0.200 -0.300 -0.400 -0.500
11.900 11.800 11.700 11.600 11.500 11.400
Galactic longitude
0.0001 0.0002 0.0004 0.0007
HESS J1809-193B
Galactic latitude
0.200 0.100 0.000 -0.100 -0.200 -0.300
11.600 11.500 11.400 11.300 11.200 11.100
Galactic longitude
0.0001 0.0002 0.0004 0.0007
HESS J1809-193E
Galactic latitude
0.600 0.500 0.400 0.300 0.200 0.100
11.000 10.900 10.800 10.700 10.600 10.500
Galactic longitude
0.0001 0.0002 0.0004 0.0007
GALACTIC_BULGE1
Galactic latitude
-0.600 -0.700 -0.800 -0.900 -1.000 -1.100
0.200 0.000 359.900 359.700
Galactic longitude
0.0001 0.0002 0.0004 0.0007
GALACTIC_BULGE2
Galactic latitude
-0.900 -1.000 -1.100 -1.200 -1.300 -1.400 -1.500
0.200 0.000 359.900 359.700
Galactic longitude
0.0001 0.0002 0.0004 0.0007

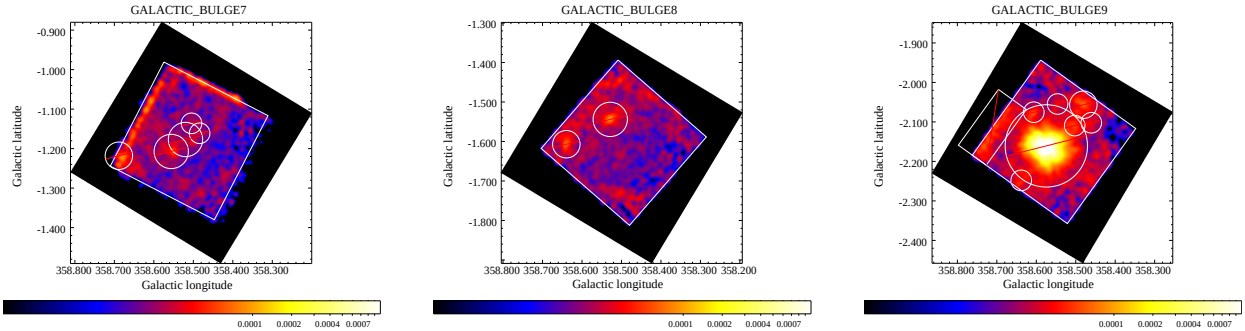
GALACTIC_BULGE7
Galactic latitude
Galactic longitude
GALACTIC_BULGE8
Galactic latitude
Galactic longitude
GALACTIC_BULGE9
Galactic latitude
Galactic longitude

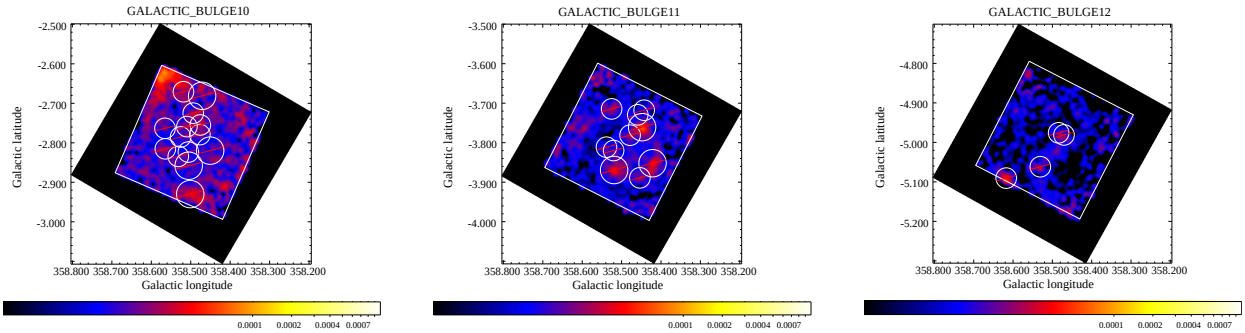
GALACTIC_BULGE10
Galactic latitude
Galactic longitude
GALACTIC_BULGE11
Galactic latitude
Galactic longitude
GALACTIC_BULGE12
Galactic latitude
Galactic longitude

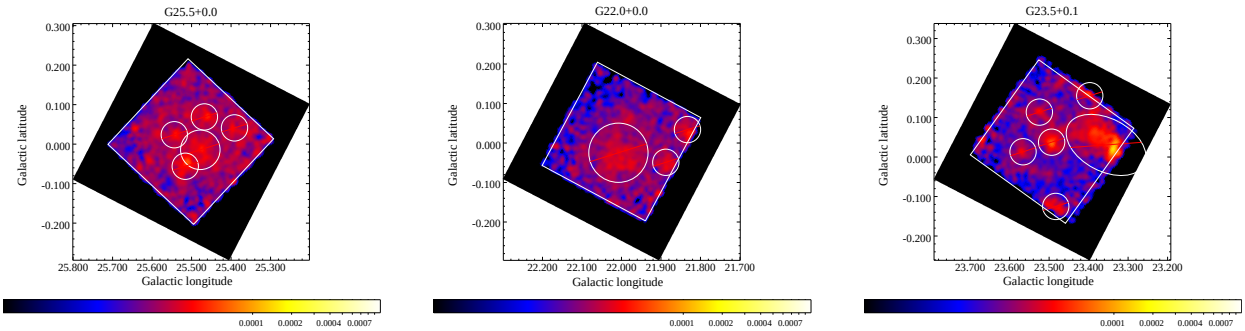
G25.5+0.0
Galactic latitude
Galactic longitude
G22.0+0.0
Galactic latitude
Galactic longitude
G23.5+0.1
Galactic latitude
Galactic longitude

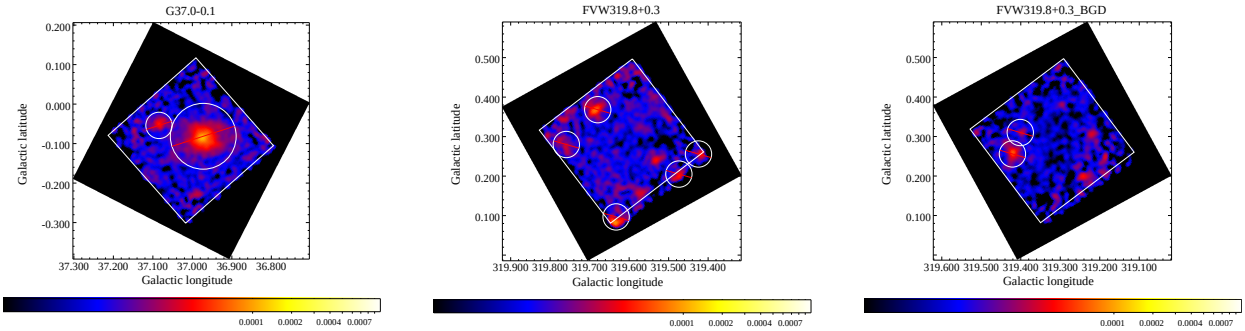
G37.0-0.1
Galactic latitude
Galactic longitude
FVW319.8+0.3
Galactic latitude
Galactic longitude
FVW319.8+0.3_BGD
Galactic latitude
Galactic longitude

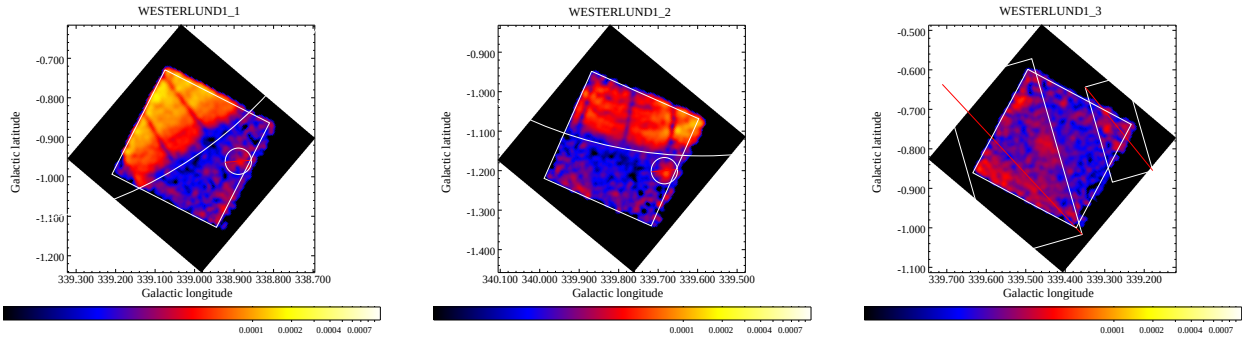
WESTERLUND1_1
Galactic latitude
Galactic longitude
WESTERLUND1_2
Galactic latitude
Galactic longitude
WESTERLUND1_3
Galactic latitude
Galactic longitude

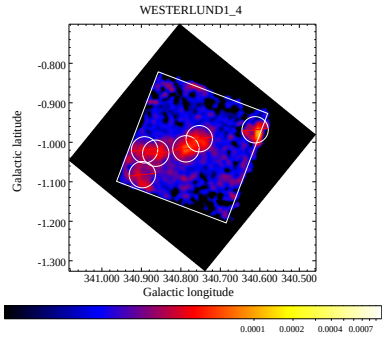
WESTERLUND1_4
Galactic latitude
-0.800
-0.900
-1.000
-1.100
-1.200
-1.300
341.000 340.900 340.800 340.700 340.600 340.500
Galactic longitude
0.0001 0.0002 0.0004 0.0007

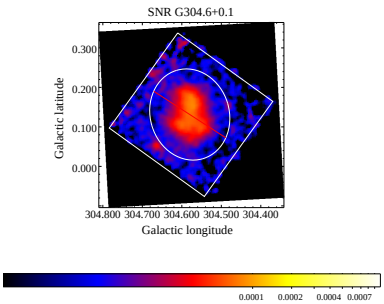
SNR G304.6+0.1
Galactic latitude
0.300
0.200
0.100
0.000
304.800 304.700 304.600 304.500 304.400
Galactic longitude
0.0001 0.0002 0.0004 0.0007

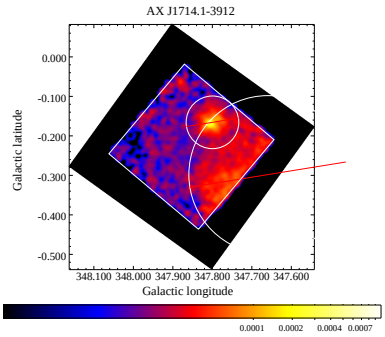
AX J1714.1-3912
Galactic latitude
0.000
-0.100
-0.200
-0.300
-0.400
-0.500
348.100 348.000 347.900 347.800 347.700 347.600
Galactic longitude
0.0001 0.0002 0.0004 0.0007

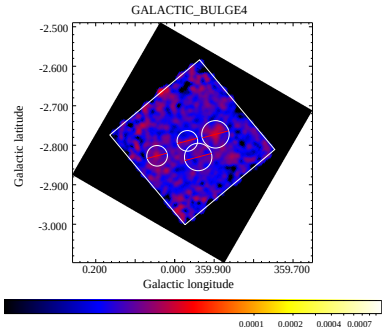
GALACTIC_BULGE4
Galactic latitude
-2.500
-2.600
-2.700
-2.800
-2.900
-3.000
0.200 0.000 359.900 359.700
Galactic longitude
0.0001 0.0002 0.0004 0.0007

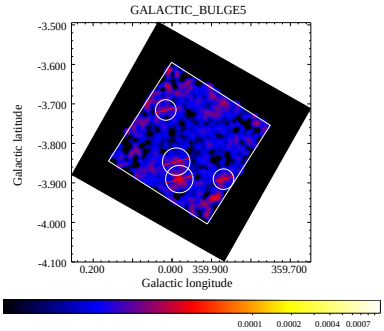
GALACTIC_BULGE5
Galactic latitude
-3.500
-3.600
-3.700
-3.800
-3.900
-4.000
-4.100
0.200 0.000 359.900 359.700
Galactic longitude
0.0001 0.0002 0.0004 0.0007

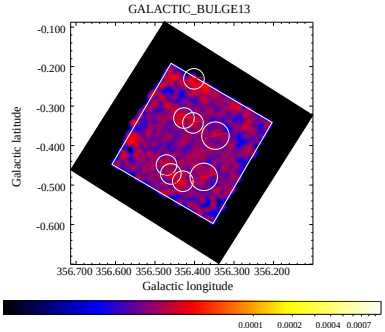
GALACTIC_BULGE13
Galactic latitude
-0.100
-0.200
-0.300
-0.400
-0.500
-0.600
356.700 356.600 356.500 356.400 356.300 356.200
Galactic longitude
0.0001 0.0002 0.0004 0.0007

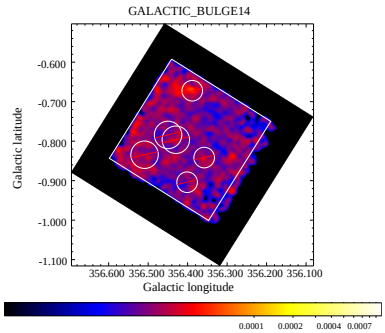
GALACTIC_BULGE14
Galactic latitude
-0.600
-0.700
-0.800
-0.900
-1.000
-1.100
356.600 356.500 356.400 356.300 356.200 356.100
Galactic longitude
0.0001 0.0002 0.0004 0.0007

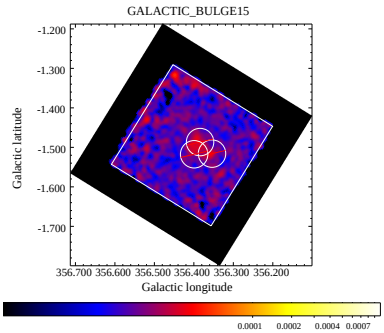
GALACTIC_BULGE15
Galactic latitude
-1.200
-1.300
-1.400
-1.500
-1.600
-1.700
356.700 356.600 356.500 356.400 356.300 356.200
Galactic longitude
0.0001 0.0002 0.0004 0.0007

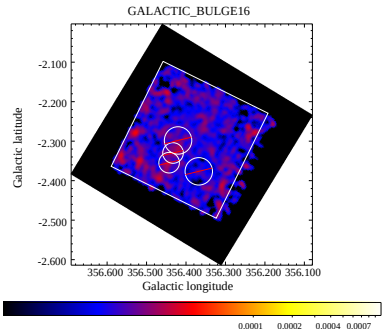
GALACTIC_BULGE16
Galactic latitude
-2.100
-2.200
-2.300
-2.400
-2.500
-2.600
356.600 356.500 356.400 356.300 356.200 356.100
Galactic longitude
0.0001 0.0002 0.0004 0.0007

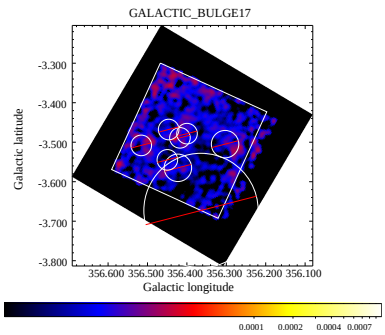
GALACTIC_BULGE17
Galactic latitude
-3.300
-3.400
-3.500
-3.600
-3.700
-3.800
356.600 356.500 356.400 356.300 356.200 356.100
Galactic longitude
0.0001 0.0002 0.0004 0.0007

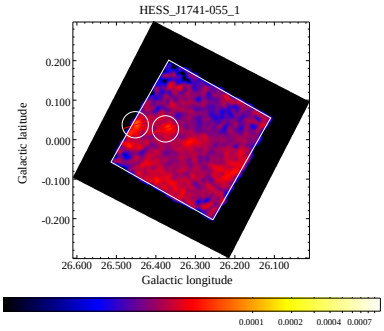
HESS_J1741-055_1
Galactic latitude
0.200
0.100
0.000
-0.100
-0.200
26.600 26.500 26.400 26.300 26.200 26.100
Galactic longitude
0.0001 0.0002 0.0004 0.0007

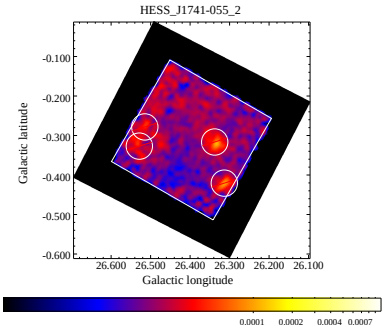
HESS_J1741-055_2
Galactic latitude
-0.100
-0.200
-0.300
-0.400
-0.500
-0.600
26.600 26.500 26.400 26.300 26.200 26.100
Galactic longitude
0.0001 0.0002 0.0004 0.0007

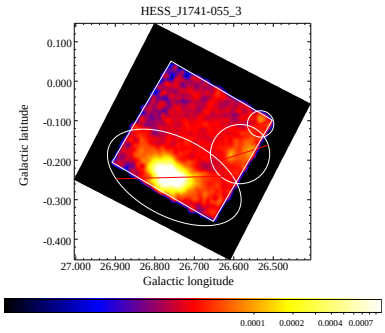
HESS_J1741-055_3
Galactic latitude
0.100
0.000
-0.100
-0.200
-0.300
-0.400
27.000 26.900 26.800 26.700 26.600 26.500
Galactic longitude
0.0001 0.0002 0.0004 0.0007

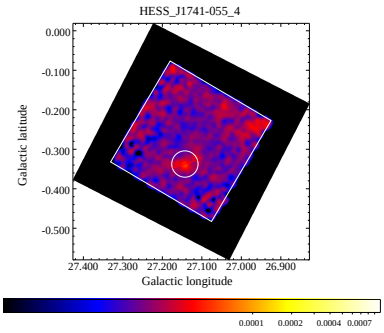
HESS_J1741-055_4
Galactic latitude
0.000
-0.100
-0.200
-0.300
-0.400
-0.500
27.400 27.300 27.200 27.100 27.000 26.900
Galactic longitude
0.0001 0.0002 0.0004 0.0007

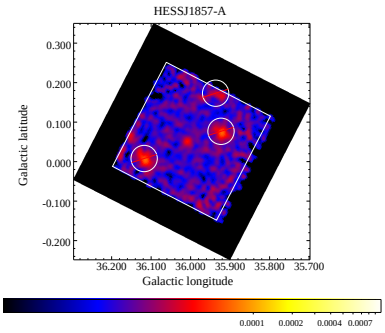
HESSJ1857-A
Galactic latitude
0.300
0.200
0.100
0.000
-0.100
-0.200
36.200 36.100 36.000 35.900 35.800 35.700
Galactic longitude
0.0001 0.0002 0.0004 0.0007

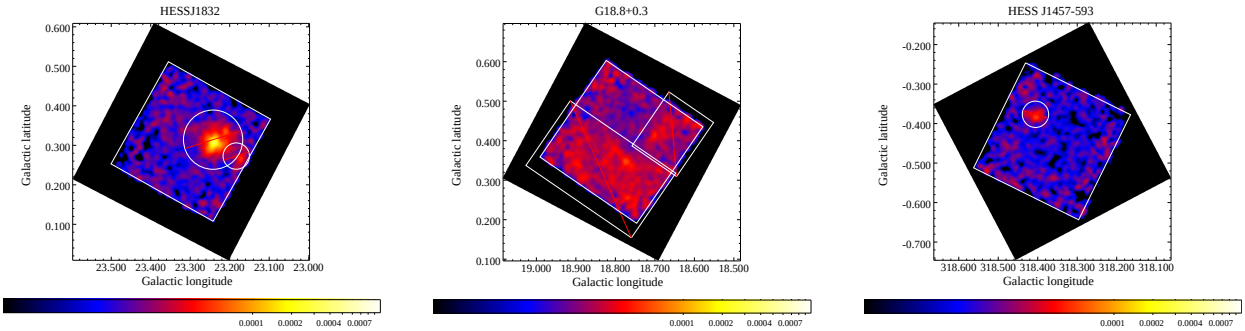
HESSJ1832
G18.8+0.3
HESS J1457-593
Galactic latitude
Galactic longitude
0.0001 0.0002 0.0004 0.0007

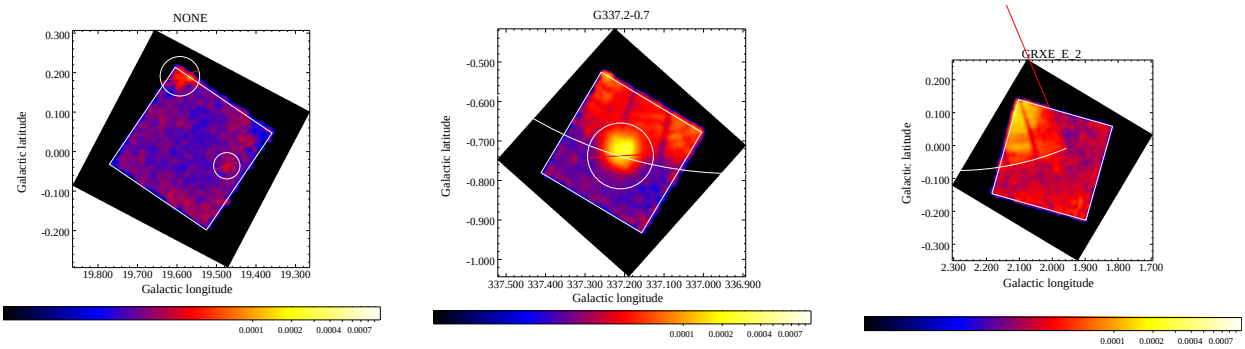
NONE
G337.2-0.7
GRXE_E_2
Galactic latitude
Galactic longitude
0.0001 0.0002 0.0004 0.0007

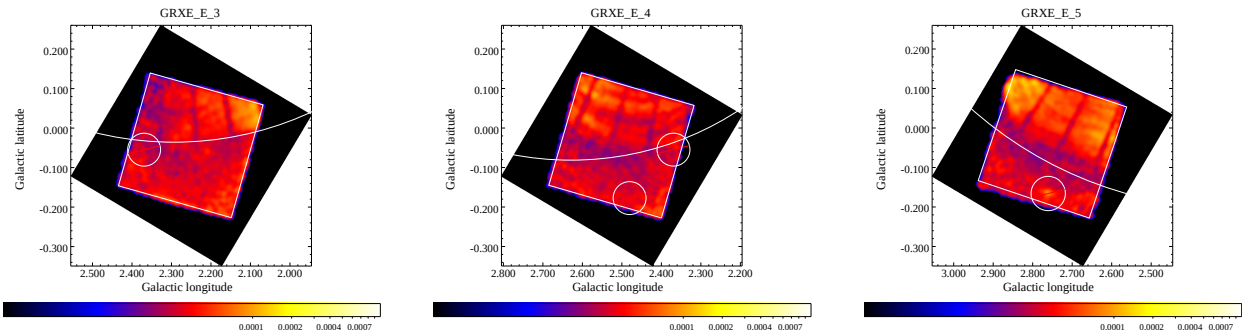
GRXE_E_3
GRXE_E_4
GRXE_E_5
Galactic latitude
Galactic longitude
0.0001 0.0002 0.0004 0.0007

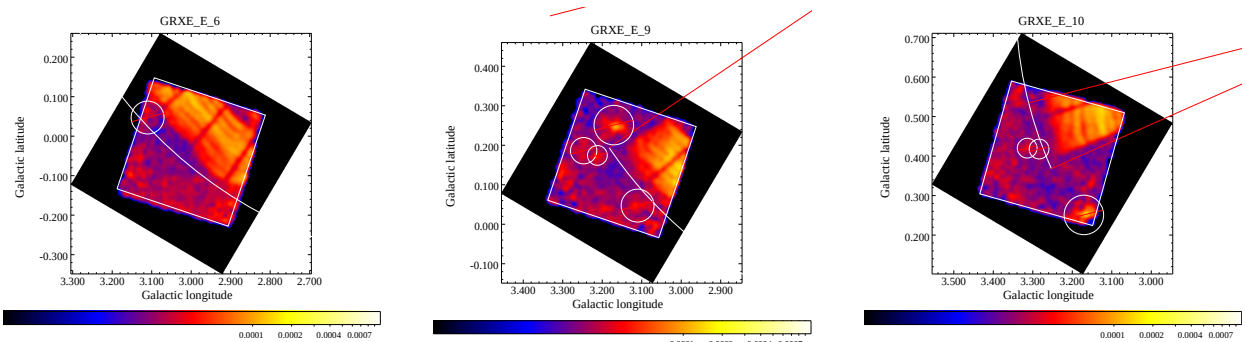
GRXE_E_6
GRXE_E_9
GRXE_E_10
Galactic latitude
Galactic longitude
0.0001 0.0002 0.0004 0.0007

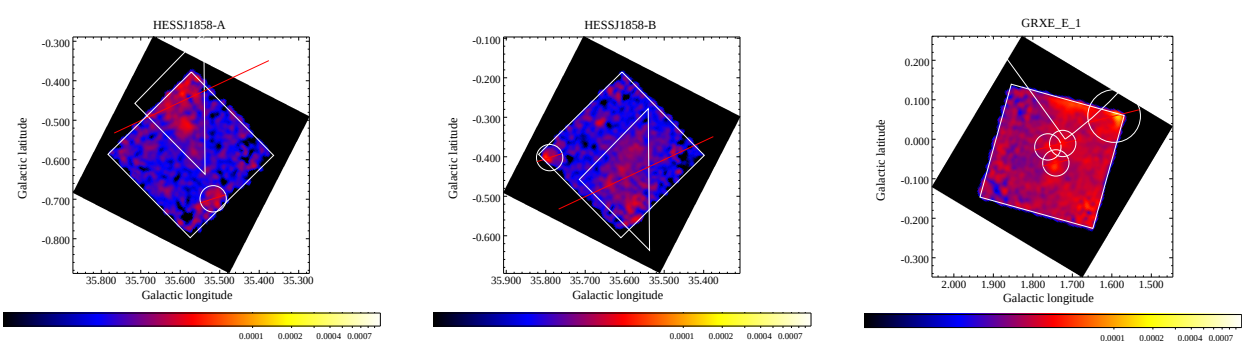
HESSJ1858-A
HESSJ1858-B
GRXE_E_1
Galactic latitude
Galactic longitude
0.0001 0.0002 0.0004 0.0007

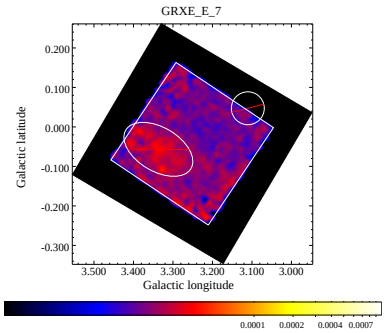
GRXE_E_7
Galactic latitude
0.200
0.100
0.000
-0.100
-0.200
-0.300
3.500 3.400 3.300 3.200 3.100 3.000
Galactic longitude
0.0001 0.0002 0.0004 0.0007

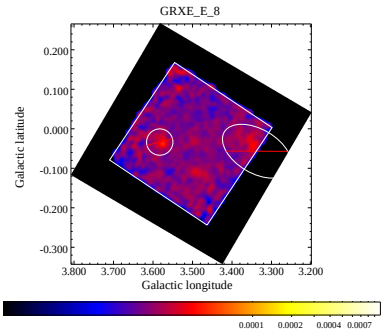
GRXE_E_8
Galactic latitude
0.200
0.100
0.000
-0.100
-0.200
-0.300
3.800 3.700 3.600 3.500 3.400 3.300 3.200
Galactic longitude
0.0001 0.0002 0.0004 0.0007

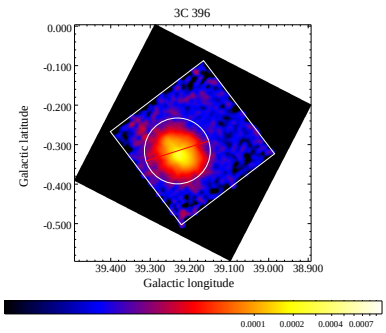
3C 396
Galactic latitude
0.000
-0.100
-0.200
-0.300
-0.400
-0.500
39.400 39.300 39.200 39.100 39.000 38.900
Galactic longitude
0.0001 0.0002 0.0004 0.0007